UNIVERSITY OF CALIFORNIA,
IRVINE

Microfluidics Flow Control for on-Chip 3D Vascularized Micro Tissues

DISSERTATION

submitted in partial satisfaction of the requirements
for the degree of

DOCTOR OF PHILOSOPHY

in Biomedical Engineer

by

Da Zhao

Dissertation Committee:
Professor Abraham P. Lee, Chair
Professor Christopher C. W. Hughes
Associate Professor Michelle A. Digman
Professor Fadi J. Kurdahi

2020

DEDICATION

To

my parents Hufang Zhao and Xiuming Zhao

in recognition of their unconditional love and support

and all my friends

for their encouragement and assistance

TABLE OF CONTENTS

Page

LIST OF FIGURES vi
LIST OF MOVIES vii
ACKNOWLEDGMENTS viii
VITA ix
ABSTRACT OF THE DISSERTATION xi
Chapter 1: INTRODUCTION 1
Chapter 2: HIGH THROUGHPUT MULTIPLE-TYPE TISSUE CO-CULTURE SYSTEM FOR 3D VASCULARIZED MICRO TISSUES 6
Background 6
Materials and Methods 8
High throughput system and microfluidics device design 8
Device fabrication and assembly 10
Cell culture 10
Cell loading and on-chip culture 11
Finite element simulation 12
Perfusion test 12
Data acquisition and analysis 12
Results 13
Different flow patterns in the tissue culture regions to control tissue-tissue interactions 13
Various tissue types formed in the tissue culture regions 15
Perfusable vascular network potential for drug screening and particle delivery study 17
Mimic of NOTCH knockout ECs and co-culture with wild type 18
Discussion 21
Chapter 3: MULTI-LAYERED CONFIGURATION FOR A MODULAR MICROFLUIDIC SYSTEM TO GENERATE LARGE SCALE PERFUSABLE MICROVASCULAR NETWORKS 24
Background 24
Materials and methods 25
Modular microfluidic system based on multi-layered configurations 25
PDMS device design and fabrication 26
Rhombic medium channel design and fabrication 28
Cell culture 29
Cell loading procedures and on-chip culture 29
Dextran-FITC perfusion 30
Data acquisition and analysis 30
Results 31
Modular microfluidic system provides various flow conditions in tissue chambers 31

Semi-closed rhombic medium channels prevent gel bursting during cell loading 34
Vertical anastomosis at the communication pores connects the microvascular networks and the medium channels 36
Large-scale microvascular networks generated in the modular microfluidic system 38
Fluorescent dextran perfusion demonstrates the microvascular networks and the medium channels are tightly connected 41
Discussion 42
Chapter 4: A HYDROSTATIC PRESSURE-DRIVEN PASSIVE MICROPUMP ENHANCED WITH SIPHON-BASED AUTOFILL FUNCTION 45
Background 45
Materials & Methods 47
Platform setup 47
Principle of siphon-based autofill function 48
Sensitivity analysis of autofill function 53
Liquid barrier connector fabrication and operation optimization 55
Finite element simulation of interstitial flow for vasculogenesis 56
Cell culture 57
Results 57
Effectiveness of enhanced micropump with autofill function 57
Characterization of the enhanced micropump 60
Parallel and multiplexed micropump with high flexibility 62
Vasculogenesis by interstitial flow with the enhanced micropump 63
Discussion 65
Chapter 5: NON-UNIFORM VASCULAR NETWORKS GENERATED BY NON-UNIFORM FLOW VELOCITY DISTRIBUTION FOR AN ON-CHIP HEREDITARY HEMORRHAGIC TELANGIECTASIA MODEL 67
Background 67
Materials & Methods 68
Microfluidics chip design 68
Finite element simulation 69
Cell culture 69
Result and discussion 70
Non-uniform flow velocity distribution in the slanted channel design 70
Vasculature formed in various designs of slanted channel device 71
High shear stress distribution in the capillary network 72
Future perspective 73
Chapter 6: LOW OXYGEN TENSION GENERATED BY MICROFLUIDICS CONTROL FOR ON CHIP 3D VASCULATURE 75
Background 75
Material and method 77
Microfluidic chip design for oxygen tension control 77

Finite element simulation 79
Cell culture 79
Calibration of Stern-Volmer equation 80
Fabrication of thin film oxygen sensor 80
Results and discussion 81
Angiogenesis induced by low oxygen tension during long-term culture 81
Observation of oxygen tension change by luminescent optical sensor and calibration of Stern-Volmer equation 83
Future perspective 85
Chapter 7: CONCLUSION AND FUTURE PERSPECTIVE 87
BIBLIOGRAPHY 92
APPENDIX A: CALCULATION OF HYDROSTATIC PRESSURE BALANCE IN MEDIUM RESERVOIR 97
APPENDIX B: 3D ALIGNING SYSTEM FOR MULTILAYER PDMS DEVICE ASSEMBLY 99
APPENDIX C: DETAILED DESCRIPTION OF THE MOVIES 101

LIST OF FIGURES

Page

Figure 1.1 Schematic of microfluidics system for 3D vascularized micro tissue with various flow control 4
Figure 2.1 The HT-MTCS design 8
Figure 2.2 Finite element simulation of the flow in the microfluidics device 15
Figure 2.3 Various tissue types formed in HT-MTCS 17
Figure 2.4 Perfusion test of vascular network in the HT-MTCS 18
Figure 2.5 Mimic of NOTCH knockout for tumor and chemical induced angiogenesis 20
Figure 2.6 Add-ons and modification of the device design 23
Figure 3.1 The modular microfluidic system, combining by two PDMS layers 26
Figure 3.2 Schematic drawing of an example device and the simulated flow conditions inside 28
Figure 3.3 Numerical simulations of the flow inside tissue chambers 33
Figure 3.4 Semi-closed rhombic medium channels was fabricated using plastic molds 35
Figure 3.5 ECs grow vertically at communication pores to form a leakage-free sealing between microvascular networks and medium channels 37
Figure 3.6 Various microvascular networks are generated in the modular microfluidic system 40
Figure 3.7 70kDa FITC-dextran perfusion demonstrated tight interconnections between the microvascular networks and medium channels 42
Figure 4.1 Schematic diagram showing the platform setup of the hydrostatic pressure-driven passive micropump enhanced with siphon-based autofill function 49
Figure 4.2 Schematic diagram showing the working principle of siphon-based autofill function 49
Figure 4.3 Electric-fluidic circuit analogy of siphon-based autofill function 54
Figure 4.4 Schematic diagram showing the sensitivity analysis of autofill function 54
Figure 4.5 Schematic diagram showing the LBC design and operation optimization 56
Figure 4.6 Comparison experiment to test the effectiveness of the enhanced micropump with siphon-based autofill function 58
Figure 4.7 Quantitative analysis of the characteristics of enhanced micropump with autofill function 60
Figure 4.8 Multiplexed micropump with the integration of four-way stopcock for selective liquid perfusion into the IMR at the predefined liquid level 63
Figure 4.9 Application of the enhanced micropump system for sustaining an in vitro vasculogenesis model 65
Figure 5.1 Microfluidics chip prototype for HHT model 69
Figure 5.2 Non-uniform velocity profile in the slanted channel design 71
Figure 5.3 Vasculature formed in chips with different angle α 72
Figure 5.4 Vessel densities in different regions of the tissue chamber 72
Figure 5.5 High shear stress distribution in the capillary network 72
Figure 5.6 High throughput design for HHT model 74
Figure 6.1 Microfluidic chip design for oxygen tension control 79
Figure 6.2 Vascularized tissue cultured in the oxygen control test device 82
Figure 6.3 Oxygen tension change observed by luminescent optical sensors 84

LIST OF MOVIES

Page

Movie 2.1 Perfusion of whole blood in the HT-MTCS chip 17
Movie 2.2 Perfusion of FITC-labeled polystyrene beads in the HT-MTCS chip 18
Movie 2.3 Perfusion of FITC-labeled polystyrene beads in the HT-MTCS chip (2) 18
Movie 3.1 Liquid loading to the rhombic shape medium channel 34
Movie 3.2 Confocal image showing the vertical anastomosis between the tissue and medium channel 38

ACKNOWLEDGMENTS

I would like to express the deepest appreciation to my committee chair, Professor Abraham P. Lee. I was always grateful to his guidance and encouragement during my whole study period. He has provided me with inspiring and valuable suggestions when I had difficulties in research. He also gave me tremendous support for presenting my research and interacting with talented researchers in the field through many conferences. Without Dr. Lee's instruction and support, this dissertation will not be possible.

I would also like to thank my committee member Professor Christopher C. W. Hughes, Professor Michelle A. Digman, and Professor Fadi J. Kurdahi. Dr. Hughes' profound knowledge in blood vessel development and tissue engineering has been a great resource for my experiment design. And the cells and other materials are also provided from Dr. Hughes' lab. Dr. Digman has provided inspiring ideas with my multiple type tissue co-culture system and important resource for the confocal imaging. And special thanks to Professor Fadi J. Kurdahi for overseeing the conflict-of-interest situation.

Great thanks to Professor Xiaolin Wang, former post-doctoral researcher in our lab, and now Assistant Professor at Shanghai Jiaotong University. We worked together in lab for two years and are still in collaboration for some research projects. And great thanks Professor Tao Yue, also former post-doctoral researcher in our lab, and now Assistant Professor at Shanghai University. They not only instructed me on the basic fabrication techniques and simulation skills, but also broaden my way of thinking. I would also like to thank my close collaborators Dr. Duc Phan, Dr. Stephanie Hachey, Dr. Jennifer Fang, and Dr. Jillian Andrejecsk, whose knowledge in their field enables the achievement in our projects. Finally, a thank you to all BioMiNT lab members, including all previous and present lab mates, especially Dr. Wei-Feng Fang, Steven Dell, Apurva Patel, Dr. Xuan Li, Yu-Hsi Chen, Mohammad Aghaamoo and Krystopher Lawrence. It was a great experience working with them, and they all provide kind help during my PhD study.

This research is funded by National Institute of Health and National Heart, Lung, and Blood Institute (NIH NHLBI UH3HL141799). I also receive funding support from National Institute of Health (UG3HL141799, UG3 TR002137-01, UH3 TR00048) during my study.

I thank the following publishers for their permission to use copyrighted materials in my published manuscripts: Chemical and Biological Microsystems Society (Chapter 2, 3, 5 and 6), and Royal Society of Chemistry (Chapter 4). I would also like to thank all the co-authors of the manuscripts for their permission to include the above-published materials in this dissertation.

Last but not least, sincerely thanks to my dear parents. They both worked in health care field. Their prudence and dedication to patients' health built model examples, which always encourage me. Their unconditional love is the strength deep in my heart supporting all these years during my study.

VITA

Da Zhao

2010	Research Assistant, Institute of Bast Fiber Corps, Chinese Academy of Agricultural Sciences, China
2011-12	Research Assistant, Central South University of Forestry and Technology, China
2012	B.S. in Biological Technology, Central South University of Forestry and Technology, China
2014-20	Graduate Student Researcher, BioMiNT Lab University of California, Irvine
2016	M.S. in Biomedical Engineering, University of California, Irvine
2019	Teaching Assistant, Henry Samueli School of Engineering, University of California, Irvine
2020	Ph.D. in Biomedical Engineering, University of California, Irvine

FIELD OF STUDY

Microfluidics application in tissue engineering

JOURNAL PUBLICATION

[1] X. Wang‡, D. Zhao‡, D. T. T. Phan, J. Liu, X. Chen, B. Yang, C. C. W. Hughes, W. Zhang and A. P. Lee, "A hydrostatic pressure-driven passive micropump enhanced with siphon-based autofill function", Lab on a Chip, 2018, 18, 2167-2177.

[2] D. T. T. Phan, X. Wang, B. M. Craver, A. Sobrino, D. Zhao, J. C. Chen, L. Y. N. Lee, S. C. George, A. P. Lee and C. C. W. Hughes, "A vascularized and perfused organ-on-a-chip platform for large-scale drug screening applications", Lab on a Chip, 2017,17, 511-520.

[3] X. Wang, D. T. T. Phan, D. Zhao, S. C. George, C. C. W. Hughes and A. P. Lee, "An on-chip microfluidic pressure regulator that facilitates reproducible loading of cells and hydrogels into microphysiological system platforms", Lab on a Chip, 2016, 16, 868-876.

PATENT

[1] A. P. Lee, T. Yue, D. Zhao and X. Wang. 2019. Multi-layered microfluidic systems for in vitro large-scale perfused capillary networks. U.S. Patent Application 16/166,989.

SELECTED CONFERENCE PUBLICATION

[1] Da Zhao, Tao Yue, et al. “Non-Uniform Vascular Networks Generated by Non-Uniform Flow Velocity Distribution for an on-Chip Hereditary Hemorrhagic Telangiectasia Model”. The 22nd International Conference on Miniaturized Systems for Chemistry and Life Sciences (MicroTAS), Kaohsiung, Taiwan, China, 11-15 Nov. 2018

[2] Da Zhao, Tao Yue, et al. “Angiogenesis Induced by Low Oxygen Tension in a Vascularized Tissue-on-Chip Device”. The 22nd MicroTAS, pp.1566-1568, Kaohsiung, Taiwan, China, 11-15 Nov. 2018

[3] Da Zhao, Duc Phan, et al. “A microfluidic device to culture multi-type 3D in vitro tissues with perfused human capillary network”. The 21st MicroTAS, pp.1035-1036, Savannah, Georgia, USA, 22-26 Oct. 2017

[4] Tao Yue, Da Zhao, et al. “Vertical anastomosis for large scale perfused capillary networks and organs-on-chip applications”. The 21st MicroTAS, pp.1133-1134, Savannah, Georgia, USA, 22-26 Oct. 2017

[5] Xiaolin Wang, Da Zhao, and Abraham P. Lee. “Enhanced hydrostatic pressure-driven passive micropump with siphon-based autofill function”. The 21st MicroTAS, pp.643-644, Savannah, Georgia, USA, 22-26 Oct. 2017

ABSTRACT OF THE DISSERTATION

Microfluidics Flow Control for on-Chip 3D Vascularized Micro Tissues

by

Da Zhao

Doctor of Philosophy in Biomedical Engineering

University of California, Irvine, 2020

Professor Abraham P. Lee, Irvine, Chair

The bottleneck for drug discovery and drug screening has prompted the recent surge for organ-on-a-chip 3D in vitro models that recapitulate physiological and disease mechanisms. Among those models, it is critical to incorporate the vascular capillary networks into micro tissue to better recapitulate the in vivo microenvironment. Microfluidics technology has become an important tool to provide better control of mass transport in the microenvironment for nutrient supply and waste removal. However, the current models only mimic certain aspects of in vivo situations. As in vitro models continue to be developed, more complex on-chip vascularized tissues are necessary to provide more precise physiological systems towards the ultimate goal of 'human-on-a-chip'.

In this dissertation, a series of microfluidic platforms are developed to enable the culturing of large scale vascularized micro tissues. The system is built on a high throughput format integrated with 96-well plate that contains multiple units for parallelization of experiments. The microfluidics channel design of each unit in this system allows co-culture of multiple types of tissue. Here, complex tissues are formed by retaining certain types of tissue in designated regions, and the

interaction of different tissue types can be studied by controlling the tissue formation and mass transport of each region. In this dissertation, a novel 3D hydrogel/medium interface and a siphon-based passive pump are developed to overcome these difficulties. Furthermore, oxygen, one of the important factors affecting tissue growth, is controlled to be at a more physiological level. Various physiological or disease models can be built by selecting and combining these microfluidics components, such as compartmentalized micro tumors co-cultured with vasculature, hereditary hemorrhagic telangiectasia induced by high shear stress, vascularized liver model with in vivo liver structure and oxygen gradient, etc.

CHAPTER 1: INTRODUCTION

A microfluidic organ-on-a-chip cell culture device is created with microchip fabrication processes that contain continuously perfused chambers inhabited by living cells arranged to simulate tissue- and organ-level physiology[1]. Organ-on-a-chip technology has been used to build human related in vitro models for physiological and disease mechanism studies. The current state of organ-on-a-chip has witnessed several tissue/organ specific models, such as adipose[2], heart[3-5], lung [6, 7]， muscle [8, 9], liver[10-12], gut[13, 14], skin[15, 16], brain[17, 18]/blood-brain barrier[19-21], blood vessel/vascularized tissue[22-27] etc. Compared with 2D tissue culture, 3D organ-on-a-chip cultures tissue provides more physiological interactions between cells and the extracellular matrices (ECM)[28, 29] to mimic the mechanical and chemical in vivo microenvironment more realistically, thus promoting cell proliferation and differentiation[30]. Organ-on-a-chip also enables reconstitution of important features of the in vivo microenvironment, such as mechanical microenvironments, spatiotemporal gradients of chemicals, tissue-tissue interfaces, etc.[31] It provides better precision to test drug efficiency and toxicity, as well as pharmacokinetics and pharmacodynamics, which potentially can validate lead candidates in the drug discovery process. It also has the possibility to replace animal tests and to develop personalized medicine and therapy due to the direct usage of human or patient cells.

Microfluidics, as an important element and tool of organ-on-a-chip, is the science and technology of systems that process or manipulate small (10^{-9} to 10^{-18} L) amounts of fluids, using channels with dimensions of tens to hundreds of micrometers[32]. By this definition, there will be minimum consumption of cells and reagents in an organ-on-a-chip reducing the cost, labor and valuable patient samples for personalized model building. When combined with other technologies, such as the microelectromechanical systems, microfluidics can build a truly synthetic system with

better control of the type and position of cells, mass transport, stimuli delivery, signal detection, visualization of the living tissue, etc.

A fully integrated system of multiple organ-on-a-chip elements is leading to a human-on-a-chip paradigm. Although the idea of a single platform is promising, it is difficult to actually integrate all the tissues or organs into one single chip. Therefore, the integration of small numbers of tissues (organs) is the building block towards a more integrated system. Such co-culture platforms have also been reported like liver and skin[33], skin and hair[34], intestine and liver[35], liver and kidney[36], and even four organ co-culture platforms[37, 38]. Multi throughput layout[39] and multi-sensors[40] are also developed to improve the performance of organs-on-chips system.

Among these models, vasculature-on-a-chip recapitulate part of the features of the circulatory system (cardiovascular system). The circulatory system, consisting of heart and hierarchical blood vessels, is an organ system that circulates blood and transports nutrients (such as amino acids and electrolytes), gases (such as oxygen, carbon dioxide), and hormones to and from the cells in the body. Capillary vessel network, where most of these material exchanges happen, has the closest physical interactions with tissue cells. Thus, an in vitro model with capillary network provides significant biological relevance to the in vivo microenvironment, which can model the barrier function of endothelial cells (ECs) and overcome the oxygen diffusion barrier[41, 42]. Therefore, the construction of tissue with large scale or thickness can be possible. One application of vasculature-on-a-chip is to generate a model to study the physiological and pathological mechanism of endothelial cell or blood vessel, such as thrombosis[43], endothelial immune response[44], atherosclerosis[45], angiogenesis[46, 47], cancer metastasis[48, 49]. Another application is to form complex tissue structures to study other tissues or organs[50-53] and drug

screening[54-57]. Vasculature-on-a-chip is also available to connect different tissues or organs-on-chips to form vascularized micro tissues.

Several methods have been reported to develop vascularized tissues, and these methods generally fall into two categories[58, 59]: (1) endothelial cell lining in engineered scaffold strategy (2) naturally formed, cell-based strategy. The former uses naturally derived[60, 61] or synthetically generated[62, 63] tubular structures as the scaffold, and then lines ECs on the inner surface of the scaffold. This method can generate channels in controlled geometry and is readily available for perfusion, but cannot generate capillary bed with diameters under a few micrometers. On the other hand, the latter generates the vasculature with vasculogenesis or angiogenesis methods by controlling mechanical[64, 65], chemical[66, 67] and biological[68] factors. This method can generate blood vessels with small diameters and more complex geometry, but it requires longer culture time and allows limited control.

Our lab and collaborators have developed a microfluidic chip to culture vasculature on chip by controlling the interstitial flow[69, 70] and studied the mass transport on the chip[71]. We have further developed vascularized tumor tissue[54] based on this chip design and achieved good anastomosis between capillary network and microfluidic channels using endothelial cell lining method[72]. A pressure regulator design[73] is developed to improve the success rate of the cell loading process. Thus, a high throughput platform has been developed for anti-angiogenic and anti-tumor drug screening[55]. Our next generation microfluidics system is to generate more integrated vascularized tissue by applying better control of different parameters, and to develop tissue specific or disease models with vasculature.

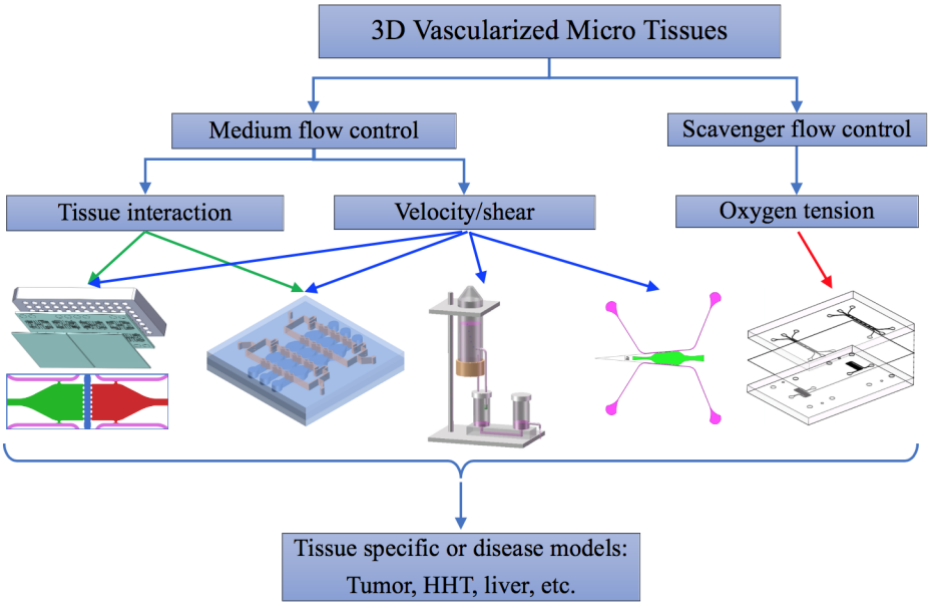

Figure 1.1 Schematic of microfluidics system for 3D vascularized micro tissue with various flow control
Medium flow and scavenger flow are controlled in the presented system. The specific device or module can be applied individually or together to form tissue specific or disease model. (HHT: hereditary hemorrhagic telangiectasia)

In this dissertation, a microfluidic system that can control the medium flow and scavenger flow is built to form integrated vascularized tissues on chip. First, a high throughput microfluidic chip is designed to enable the co-culture of multiple tissue types, in which vascularized tissue can be generated and the mass transport to the tissue is controlled by the medium flow from hydrostatic pumps. Different patterns of vasculature can be generated in compartmentalized microfluidic chip design, and the mass transport can be visualized by simulation software. As a demonstration, compartmentalized vascularized tumor tissues are generated, which provide researchers with a platform to study the whole process of metastasis. Another demonstration is a mimic of genetic wild type/knockout co-culture model for chemical and tumor induced angiogenesis study, which is hard to build in vivo. Second, a two-layer microfluidic chip is designed to provide novel liquid/gel interfaces for medium delivery to the vascularized tissues. This design overcomes the spatial limitation of previous designs and allows versatile, modular combinations to generate large

scale vascularized tissues. In this design, more tissue types and large area of tissues can be cultured and observed in a compact region, which will improve the throughput for experiments. Third, a siphon-based autofill micropump is developed to maintain a steady hydrostatic pressure of medium input into the on-chip vascularized tissues for a prolonged time period. The pump can be integrated with all the current culture systems with hydrostatic pressure-driven pump and perform the autofill function in a highly sensitive manner with a special design called liquid barrier connector. It also has the capability of selective delivery of medium or drug solution to the vascularized tissue on chip. The pump is small in size and doesn't require any power input, which makes it suitable for point-of-care applications. Fourth, an oxygen tension control module for vascularized tissue on a chip is designed. Oxygen tension can be controlled locally with scavenger solution to physiological level to replicate the in vivo microenvironment, and oxygen gradient can be generated across the vascularized tissue for a liver-on-a-chip model. The oxygen distribution can be visualized and quantified by on chip oxygen sensors. Last, on chip disease model for hereditary hemorrhagic telangiectasia (HHT) is developed. HHT is a hereditary disorder correlated with high blood flow and shear stress. A series of microfluidics chips is designed to generate different flow profiles for non-uniform vascular network to mimic HHT-like symptom.

The presented microfluidic systems enable high-throughput large-scale multiple vascularized tissues co-culture by controlling different aspects of parameters. The ultimate goal is to creat integrated organs-on-chips models for drug efficacy and toxicity studies.

CHAPTER 2: HIGH THROUGHPUT MULTIPLE-TYPE TISSUE CO-CULTURE SYSTEM FOR 3D VASCULARIZED MICRO TISSUES

Background

The current development of organ-on-a-chip technology has witnessed a number of tissue-specific models and recently advancing towards multiple tissue/organ co-culture system for more complex body-on-a-chip models. Microfluidics technologies can establish tissue-tissue interfaces for compartmentalization of certain tissue type in designated regions. The commonly used devices for generating the interfaces include porous membranes (including well plate insert)[19, 21, 27, 38, 50], post arrays[20, 53, 74, 75], phase guide[76, 77], etc. Several co-culture models have been reported[33-39]. In these models, cell metabolism[35], nanoparticle delivery[27], and drug efficacy[39] and toxicity[36] are studied. The types of tissue structures include cell monolayer[36], cell aggregates[37] or combination of both[38], connected by microfluidics channels mimicking blood circulation. These models can assist in studying the interaction between certain organs, but the simplicity of individual tissue type loses the detailed structures of specific tissues. Co-culture models with complex tissue structures exist in tissue or organ specific models, such as blood-brain barrier[19, 20], vascularized tumor[27], etc. Hence, a microfluidics chip design that contains vasculature induced by interstitial flow is used to study the homotypic and heterotypic cellular communications[78]. In these models, the tissue type in each compartment is homogeneous, but the whole chip forms a complex tissue structure. Restricted by the design, each of the compartment performs only as a part of tissue unit and lacks the control of microenvironment.

To fill the gap between single tissue type model and multiple organ co-culture models, as well as apply vasculature to the co-culture system, we present a High Throughput Multiple-type Tissue Co-culture System (denoted as HT-MTCS) for 3D vascularized micro tissues. In the

presented system, post arrays are used to compartmentalize the tissues. Each compartment can be seen as an independent tissue unit and connect to the neighboring tissue through the vasculature autonomously formed by ECs, whereas the whole co-cultured system be can be seen as an organ with compartmentalized tissue structures, or a multiple-organ system connected with vasculature based on tissue formation in each compartment. The medium flow in the system is driven by hydrostatic pump, where the pressure input from the hydrostatic pump can be controlled to change the mass transport through the vasculature. Simulation software COMSOL Multiphysics is used to characterize the flow in ECM and vasculature. As a demonstration, compartmentalized vascularized tumor models are generated, which contain tumor region and healthy tissue region. The HT-MTCS provides the possibility of observing the whole cancer metastasis process in a single microfluidics platform. Another demonstration develops a genetic wild type/knockout co-culture model for growth factor and tumor induced angiogenesis study. We mimic the NOTCH knockout model by treating ECs with gamma-secretase inhibitor N-[N-(3,5-difluorophenacetyl)-l-alanyl]-S-phenylglycine t-butyl ester (DAPT)[79]. Then the normal and DAPT treated ECs are loaded in different compartments of the system to form a wild type/knockout co-culture that is difficult being built in vivo. The junction number and vessel area in each compartment are compared, and the chemical and tumor induced angiogenesis are observed and compared at the same time. In general, the HT-MTCS is a platform for co-culturing multi-type vascularized microtissues that can be used as integrated organs-on-chips models.

Materials and Methods

High throughput system and microfluidics device design

The HT-MTCS is a microfluidics system integrated with 96 well plate (Figure 2.1(A)), similar to the high throughput drug screening platform[55] we published before. The whole system is assembled, from top to bottom, with a bottomless 96 well plate (Greiner Bio-One), a polydimethylsiloxane (PDMS) layer with microfluidics device design (denoted as PDMS device layer) and silicone rubber sealing films (PAX Industries). The device layer contains 8 microfluidics device units (Figure 2.1(B)) that form a 4×2 format (U1 to U8).

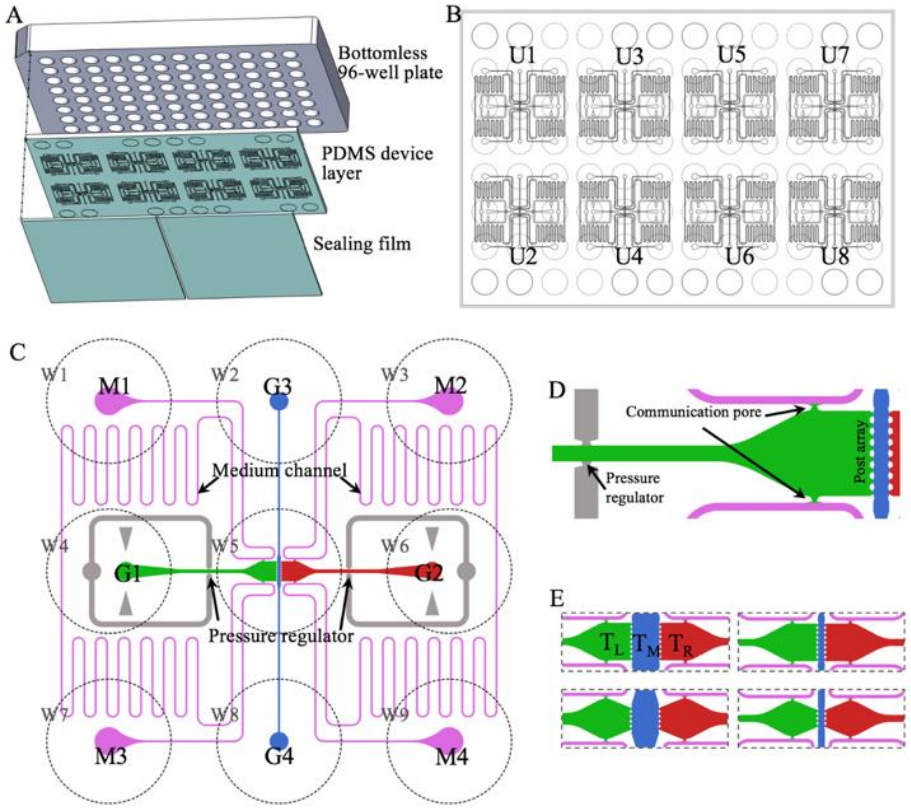

Figure 2.1 The HT-MTCS design
(A) Schematic of the assembly of HT-MTCS. (B) The layout of 8 units (U1 to U8) of microfluidics devices in the PDMS device layer, which takes a 4×2 format aligned with wells. (C) Schematic of a single microfluidics device unit. The unit takes a 3×3 footprint of wells (W1 to W9). (D) The capillary burst valves in different positions in the gel loading region. (E) Different designs of the tissue culture regions, noted by different colors separated by post arrays.

Each unit of microfluidics device (Figure 2.1 (C)) takes a 3×3 footprint in well plate (W1 to W9) and the height for the microfluidics channel is 100μm. The tissue culture regions (located in W5) consist of two tissue chambers that allow vascularized tissues to form (T_L and T_R) and a connecting channel (T_M) that allows the introduction of another type of tissue or ECM, and they are separated by post arrays. The gel loading ports (G1 to G4) are located in different wells, which guide gel loading to different tissue culture regions. The pressure regulator[73] we've developed for ease of gel loading are applied with each of the gel loading channel of the two tissue chambers on side. The medium inlets (M1 to M4) are connected by microfluidics channels with microfluidics resistors that are design for prolonged perfusion (calculation method in Appendix A). The flow profiles in the tissue culture regions can be adjusted by the hydrostatic pressure generated by the medium in the wells where the inlets are located. The medium channels (100μm in width) are connected to the tissue chambers by the capillary burst valve[73] at the communication pore (open width 50μm), where a liquid/gel interface is built. The capillary burst valve design is also used at the post array (open width 40μm) and pressure regulator (open width 85μm). The rationale for the capillary burst valve is using surface tension to stop the gel at the valve; since the width at the opening of capillary burst valve is getting smaller following the sequence where gel flows ($W_{\text{pressure regulator}} > W_{\text{communication pore}} > W_{\text{post array}}$) (Figure 2.1(D)), the capillary burst valve at the pressure regulator will burst first to release the pressure thus protecting the gel interfaces at communication pore and post array[75].There are some variations for the geometry of the tissue culture regions (Figure 2.1(E)) for different applications. The narrow device has a width of 200μm for the connecting channel while the wide device has a width of 800μm. The necking device has a narrow necking at the post array while the flat device doesn't.

Device fabrication and assembly

The general fabrication process follows the protocol we developed for the previous high throughput platform[55]. The SU-8 molds for two halves of the HT-MTCS device layer are fabricated by standard soft lithography method. Then a thick layer of PDMS replicate is generated from each half of the SU-8. These thick PDMS replicates are then trimmed and aligned to the 96 well plate layout in a customized silicone rubber case. A polyurethane liquid resin (Smooth Cast 385, Smooth-On Inc.) is used to cast the master mold. After demolding, the master is used to cast thin layer of PDMS for the full PDMS device layer. After trimming and punching inlets, the PDMS device layer is ready for assembly. The bottom of the 96 well plate is treated in a glass container by a chemical glue solution, namely 2% (v/v) of (3-Mercaptopropyl)trimethoxysilane (Sigma-Aldrich) diluted in methanol, for 1 minute. The treated 96 well plate is rinsed with DI water and then dried naturally in a chemical fume hood. Then all the parts are assembled by oxygen plasma in two steps: first, the bottom surface of the treated plate and the top surface of PDMS device layer are treated with oxygen plasma for 1.5mins, aligned and bonded; and second, the bottom surface of the PDMS device layer and the sealing film is treated by oxygen plasma for 1.5mins as well and bonded together. Then fully assembled device is kept at 65℃ oven overnight as a post bonding process. Before using, the device is sterilized under UV light for 30mins and covered with a lid.

Cell culture

Human endothelial colony-forming cell-derived endothelial cells (ECFC-ECs) and human umbilical vein endothelial cells (HUVECs) are isolated from cord blood[80, 81] and expended in 0.1% gelatin coated flask with EGM-2 medium (Lonza). ECFC-ECs are used from passage 4 to 9, and HUVECs are used from passage 4 to 7. To help tracking the vasculature growth, both cells are

transduced with lentivirus (Addgene) to express mCherry, Venus-GFP, or Azurite blue fluorescent protein. For the ECs to mimic NOTCH knockout, DAPT (Sigma-Aldrich) modified EGM-2 medium (final concentration 2μM) is used in the flask two days before cell loading, and during the on-chip culture. Normal human lung fibroblasts (NHLFs) are purchased from Lonza, cultured in DMEM (Corning) containing 10% Fetal Bovine Serum (FBS, Gibco), and used between passages 5 to 8. SW620 colon cancer cells are also cultured in DMEM medium with 10% FBS and are transduced with lentivirus expressing mCherry fluorescent protein. All the cells are cultured in a fully humidified 37°C/5% CO_2/20% O_2 incubator.

Cell loading and on-chip culture

ECs (ECFC-ECs or HUVECs) and NHLF are harvested and resuspend in 10mg/ml fibrinogen (Sigma-Aldrich) solution at 7×10^6cells/ml for each cell type. The cell-fibrinogen mixture is mixed with 50U/ml thrombin (Sigma-Aldrich) at 5:1 ratio (v/v) and quickly loaded into gel loading port. During experiment, gel loading port G1 and G2 are loaded first for tissue chamber T_L and T_R. After the gel in these two regions are fully polymerized, gel is loaded to the connecting channel T_M though gel loading port G3 or G4. Then 1mg/ml mouse laminin (Gibco) is loaded through medium inlets M1 and M2 to coat the communication pore regions of T_L and T_R, which will assist the ECs anastomosing to the medium channels. At last, EGM-2 medium is perfused to replace laminin, and hydrostatic pressure is set up by different medium volume in medium well (W1, W3, W7, and W9). For the DAPT treated ECs, DAPT modified EGM-2 medium is applied to the corresponding wells during the culture, and the standard EGM-2 medium is applied to the control group.

Finite element simulation

COMSOL Multiphysics® 5.2a (COMSOL Inc.) is used to perform finite element simulations for the interstitial flow through ECM and the laminar flow inside a developed microvascular network. The built-in free and porous media flow model is used to simulate the interstitial flow through the fibrin gel (permeability $1.5\times10^{-13}m^2$). For the laminar flow model, an image of fully developed vascular network is first processed with ImageJ (National Institute of Health) software by adjusting the contrast and brightness, and then finding edges. The resulting outline is converted to a .dxf file using software Img2CAD (Img2CAD.com) and fixed for broken and crossover fragments using software AutoCAD (Autodesk, Inc.). The refined outline is then scaled and integrated with the microfluidics channel geometry as the final geometry. The final geometry is imported to COMSOL and simulated by the built-in laminar flow model.

Perfusion test

70kDa FITC-labeled dextran (final concentration of 50μg/ml, Sigma-Aldrich) is perfused to the medium channel through medium inlet M2 to test whether the capillary network is formed, and anastomosis is achieved. FITC labeled polystyrene beads (7.3μm in diameter) and full blood are also used to perfuse the channel to validate the flow in the vascular network. The beads suspension and the blood are also loaded through M2 but are injected with pipette to increase the flow velocity.

Data acquisition and analysis

Bright-field and fluorescent images are obtained by an optical microscope (Olympus IX51 and Canon 5D II camera). Images with different color channels are merged in ImageJ. The number

of junction and vessel area in the tissue chamber T_L and T_R are calculated by AngioTool (National Institute of Health). The angiogenic sprouting number towards center channel T_M is manually counted for the sprouts passing the gel interface between T_L and T_M, as well as T_R and T_M. All data are collected from 4 repeats of experiments (4 device units). Data are shown in the format mean ± standard deviation unless stated. The comparison between different tissue chambers is analyzed by a two-tail t-test using Microsoft Excel. Microsoft Excel is also used to calculate and plot the mean value and standard deviation.

Results

Different flow patterns in the tissue culture regions to control tissue-tissue interactions

The vasculogenesis process is induced by the pressure driven interstitial flow through the porous fibrin gel matrix[71], and visualized by finite element simulation. The velocities of the flow through the tissue culture regions (Figure 2.2 (A)&(B)) are maintained in the range we've published[55] to stimulate the vasculogenesis. Since the device design for the HT-MTCS includes four medium inlets, the flow pattern across the tissue culture regions can be altered based on the volume of medium in the wells where medium inlets reside (W1, W3, W7, W9), or simply the pressure inputs to the medium inlets (M1 to M4). We defined two general flow patterns through the device, namely the vertical flow mode (Figure 2.2 (A)) and horizontal flow mode (Figure 2.2 (B)). In vertical flow model, the medium input settings are V_{W1}= 370µl (P_{M1}= 1.09cmH_2O =106.69Pa), V_{W3}= 370µl (P_{M2}= 1.09cmH_2O =106.69Pa), V_{W7}= 50µl (P_{M3}= 0.15cmH_2O =14.42Pa) and V_{W9}= 50µl (P_{M4}= 0.15cmH_2O =14.42Pa). In this flow mode, the flow direction is mainly from the top to the bottom of the tissue culture regions, and the connecting channel T_M in the middle receive equal affection from T_L and T_R and the crosstalk between T_L and T_R is impaired. In

horizontal flow model, the medium input settings are V_{W1}= 370µl (P_{M1}= 1.09cmH_2O =106.69Pa), V_{W3}= 185µl (P_{M2}= 0.54cmH_2O =53.34Pa), V_{W7}= 185µl (P_{M3}= 0.54cmH_2O =53.34Pa), and V_{W9}= 50µl (P_{M4}= 0.15cmH_2O =14.42Pa). In this flow mode, the flow from the T_L is introduced to T_R, and T_M will receive more mass delivered from T_L. The pressure inputs can be altered between W1 and W3, as well as W7 and W9, to change the flow direction from T_R to T_L. Thus, the mass transport through all tissue culture regions can be selectively modified during experiment to control the crosstalk between different parts.

After the vasculature formed in the device, the flow in the vessel can also be altered by the pressure input to the medium inlets. Due to the randomness of EC alignment during the tissue remodeling of vasculogenesis, each vascular network needs to be modeled and studied individually with finite element simulation. Figure 2.2 (C) & (D) are models from the vasculature in Figure 2.3 (B) under the two flow modes. The different pressure gradient and flow direction in the vascular network indicate different patterns of tissue-tissue interactions. During experiment, a simulation model can be setup near the end of vasculogenesis to predict the mass transport in the device, then used to instruct later experiment such as target cell traveling in the tissue, drug delivering particles movement, etc.

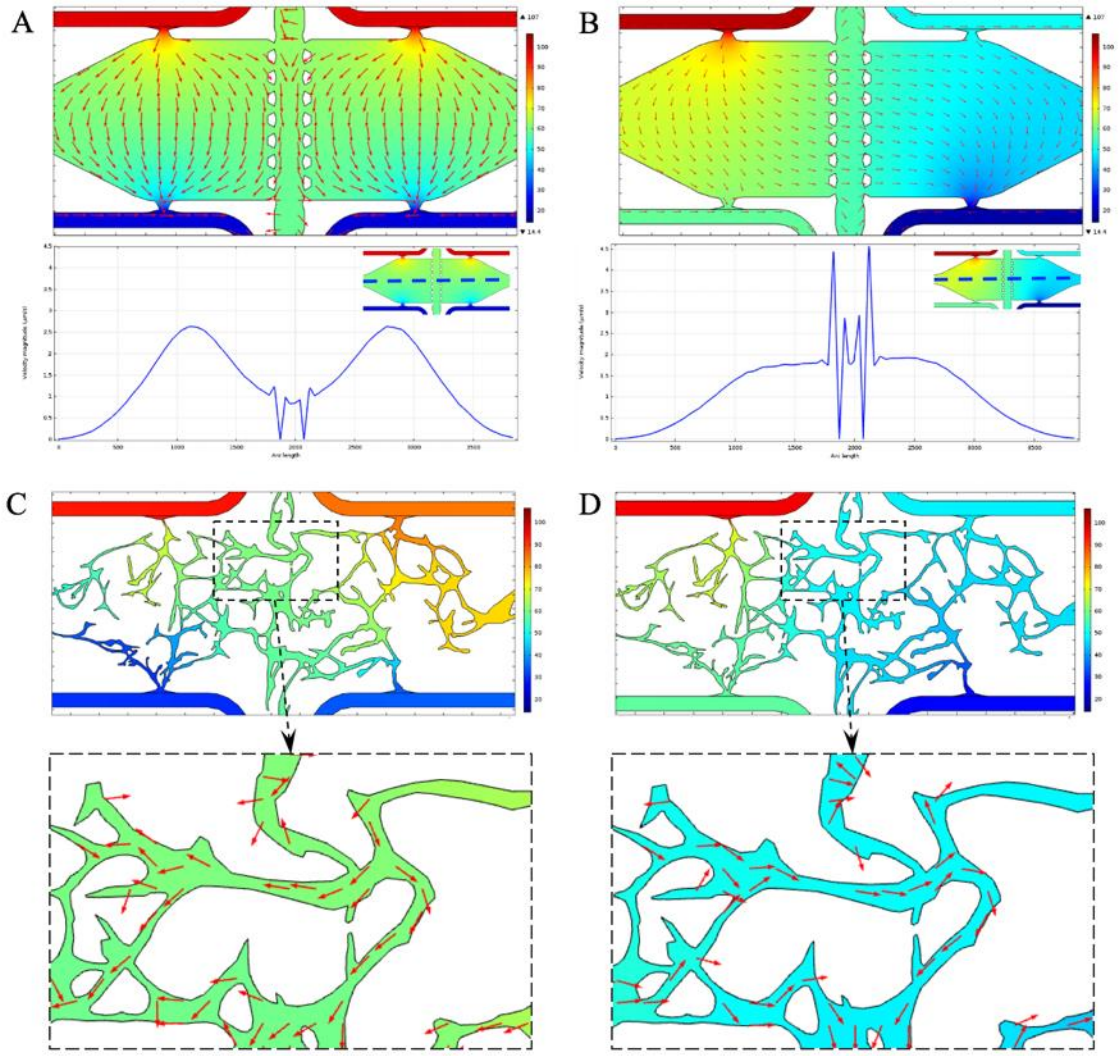

Figure 2.2 Finite element simulation of the flow in the microfluidics device
(A) Flow pattern of the vertical flow mode. The color gradient and the arrow surface represent the pressure gradient and flow speed respectively, same with all other plots. The velocity plot from the cutting line indicates that the velocity of interstitial flow is in the range to stimulate vasculogenesis. In this mode, T_L and T_R are relatively independent and have less interactions, and T_M has less interstitial flow than T_L and T_R. (B) Flow pattern of the horizontal flow mode. T_L and T_R have more interactions with the horizontal flow. T_M has similar interstitial flow with T_L and T_R, and is affected more by one tissue chamber. (C) and (D) The laminar flow in the modeled vascular network under vertical flow mode and horizontal flow mode respectively. The zoom-in boxes indicate different flow directions that affect the tissue-tissue interactions.

Various tissue types formed in the tissue culture regions

The post arrays can separate the boundary between different tissue culture regions, which allow individual control of the composition of each tissue culture region (such as cell type, color and concentration, ECM type and concentration, etc.). As demonstrated, different shapes of

vasculature and vascularized micro tumors are presented (Figure 2.3). In Figure 2.3 (A) to (D), different device designs are showcased with different shapes of vasculature, namely the narrow flat design and the wide flat design (Figure 2.3 (A) & (B) VS. (C) & (D)). In each design, the connecting channel T_M is chosen either to be loaded with vasculature (Figure 2.3 (B) & (D)), which form a complete vascularized tissue, or without vasculature (Figure 2.3 (A) & (C)), which mimics two vascularized tissues bridged by connective tissue. The different width of T_M provides more choices to build different types of tissue models that fit in vivo situation better. Figure 2.3 (B) shows a co-colure model of HUVECs with different fluorescent labels. The HUVECs are restricted in the predefined regions in the beginning of culture, that is Venus-GFP cell in T_L and Azurite blue in T_M and T_R. And we have observed that the two cell types pass the interface between different regions and migrate into the neighboring chamber at the end of culture (Day 7). As a further demonstration of complex tissue structures, we formed vascularized micro tumors in different regions (Figure 2.3 (E) to (G)). Colon cancer line SW620 labeled with mCherry fluorescence is used for the tumor model. HUVECs are still used for the vascular network, but SW620 cell is mixed in T_L, T_M and T_R respectively ($1\times10_6$cells/ml) during the cell loading process to form a vascularized healthy/tumor co-culture model during the vasculogenesis process.

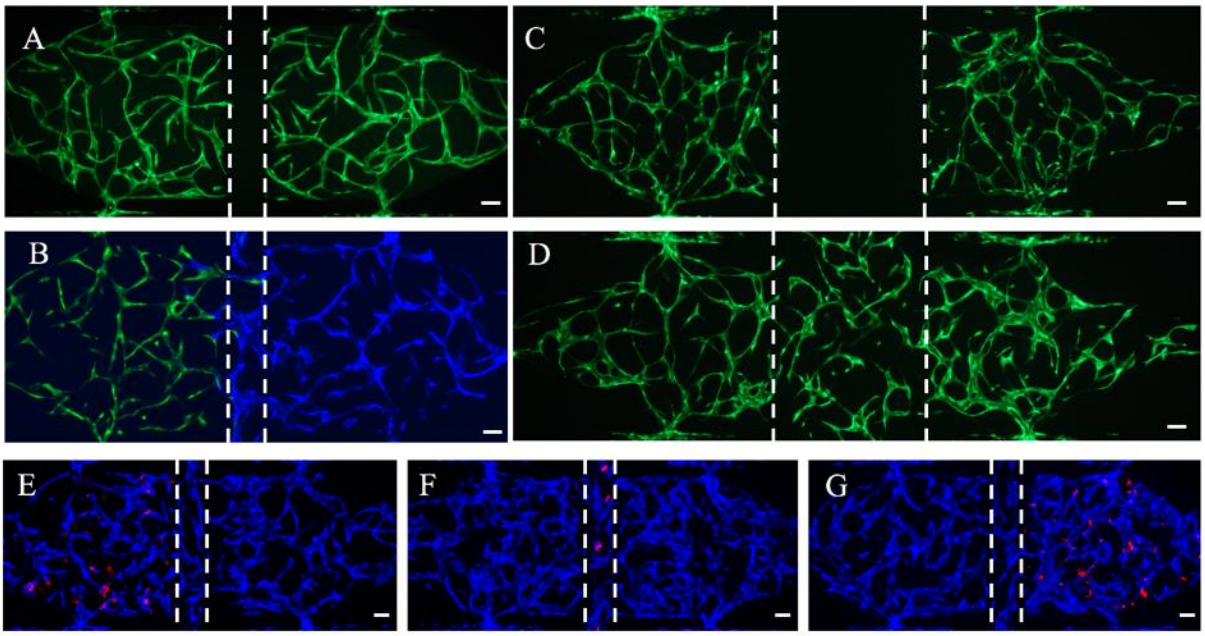

Figure 2.3 Various tissue types formed in HT-MTCS
(A) & (B) vasculature formed in narrow flat design, with T_M loaded with/without cells. HUVECs with different fluorescent labels are used in (B), and cell migration to neighboring chamber observed. (C) & (D) vasculature formed in wide flat design, with T_M loaded with/without cells. (E) to (G) vascularized micro tumors in different tissue culture regions. All scale bars are 100μm, and the dashed lines labels the positions of post arrays. HUVECs are labeled with Venus-GFP and Azurite blue, and SW620 cells are labeled with mCherry fluorescence.

Perfusable vascular network potential for drug screening and particle delivery study

As one of the advantages of in vitro vascularized tissue, the lumen formed by ECs provides the pipeline for mimicking the blood flow and the method for drug or drug-coated particle delivery. In our system, whole blood, 70kD FITC-dextran solution and FITC labeled polystyrene beads are used to validate the function of lumen formed by ECFC-ECs (Figure 2.4). Figure 2.4 (C) shows a group of time lapse images indicating the full blood perfusion through the vascular network. We observe red blood cells are deformed and squeeze through capillary vessel in single column (circle out in Figure 2.4 (C), Movie 2.1), which is same as in vivo tissue. 70kD FITC-dextran solution is chosen as an indicator of serum since it has similar molecular weight as albumin, it also can be seen as the representative of drug solution. The perfusion result (Figure 2.4 (B)) shows that the vascular network is anastomosed with microfluidics channels and only has minor leakage. So, the

cultured vascular network can mimic the barrier function of in vivo ECs to hold drug solution in the endothelial lumen yet allows drug to be delivered to tissue through the gap between ECs. We also perfuse the polystyrene beads (7.2μm in diameter, Movie 2.2 and Movie 2.3) to mimic the drug delivering particles or droplets. Figure 2.4 (A) is a group of time lapse images showing fluorescent beads passing through the vasculature and across the post array to neighboring region. The different diameters of beads in the frame indicate that the beads flow out of the focal plane, which is a proof of the 3D vasculature formed in our device.

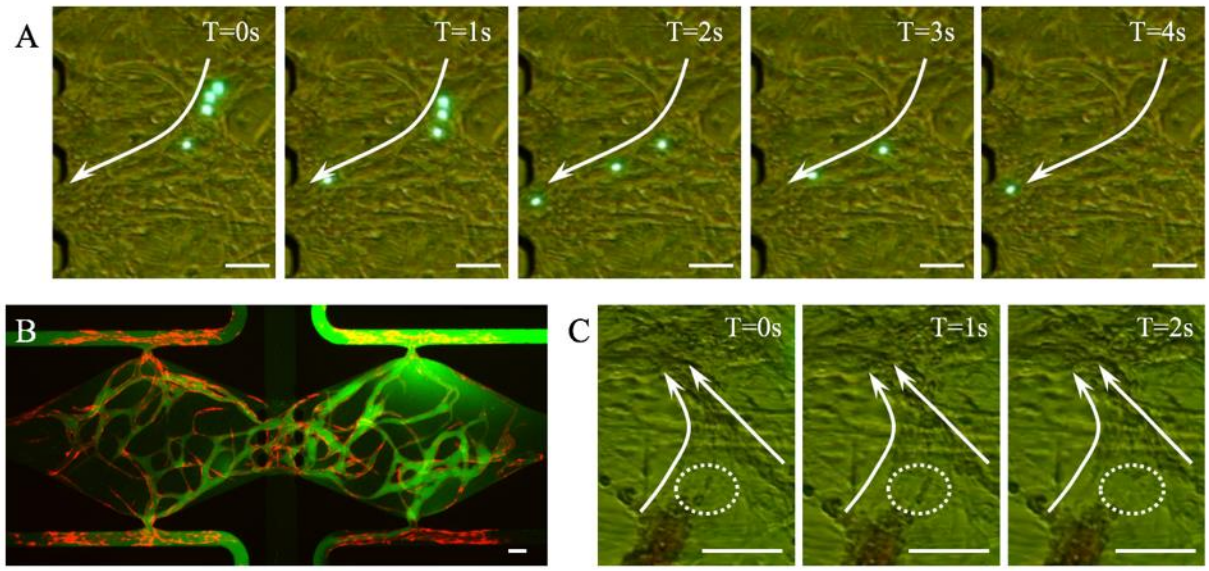

Figure 2.4 Perfusion test of vascular network in the HT-MTCS
(A) Time lapse images of FITC labeled polystyrene beads (7.2μm in diameter) perfused in vascular network. The beads flow from T_R*, passing the post array, to* T_M*. The larger diameter of the beads in the frame indicates that the beads are out of the focal plane. (B) 70kD FITC-dextran perfused in the narrow necking design. The dextran solution is loaded in medium inlet M2 and flows across the whole network. The ECFC-ECs are labeled with mCherry fluorescence. (C) Time lapse images of whole blood perfused in vascular network. The red blood cell deformation and passing through capillary vessel is labeled in the circle. All scale bars are 100μm, and the white arrows are the label of flow direction.*

Mimic of NOTCH knockout ECs and co-culture with wild type

As another model example of the HT-MTCS, we mimic a wild type/knockout co-culture model of NOTCH signaling pathway and observed angiogenesis during the culture. Several

published results proved that the activation of NOTCH signaling pathway can restrict new EC sprouting, and downregulate the vascular lumen diameter by suppressing EC proliferation[82, 83]. DAPT is a γ-secretase inhibitor that can block the γ-secretase complex, thereby inhibiting the NOTCH signaling pathway[79]. The DAPT treated HUVECs are used in our experiment to mimic the NOTCH knockout, loaded in T_R, while the untreated HUVECs are used as a control, loaded in T_L. The connecting channel T_M is set to three experimental conditions to study tumor or chemical induced angiogenesis: (1) SW620 cells (noted as cancer), (2) 50ng/ml growth factors (VEGF & HGF, noted as GF+50) (recombinant human HGF protein, R&D Systems; human VEGF-165, Shenandoah Biotechnology), (3) 100ng/ml growth factors (VEGF & HGF, noted as GF+100). Our hypothesis is that the DAPT treated HUVECs will have more branches and larger diameters (indicated by vessel area) in the tissue chambers and have more sprouts towards the connecting channel than control group. The control group is labeled with Venus-GFP and loaded to T_L, while the DAPT treated experimental group is labeled with Azurite blue and loaded to T_R. For the tumor induced angiogenesis, SW620 cells ($1\times10_6$cells/ml) is mixed with fibrin gel and loaded into T_M during cell loading process. For the chemical induced angiogenesis, both VEGF and HGF are premixed with fibrin and loaded in T_M when cells are loaded to tissue chambers, and 50μl of the growth factors dissolved by EMG-2 medium is add to well W2 during the whole culture period. $VEGF_{165}$ is used to for sustained release during the experiment[84]. The vertical flow condition is used during the whole culture and the flow direction is only flipped vertically every day to reduce the crosstalk between DAPT treated and control network.

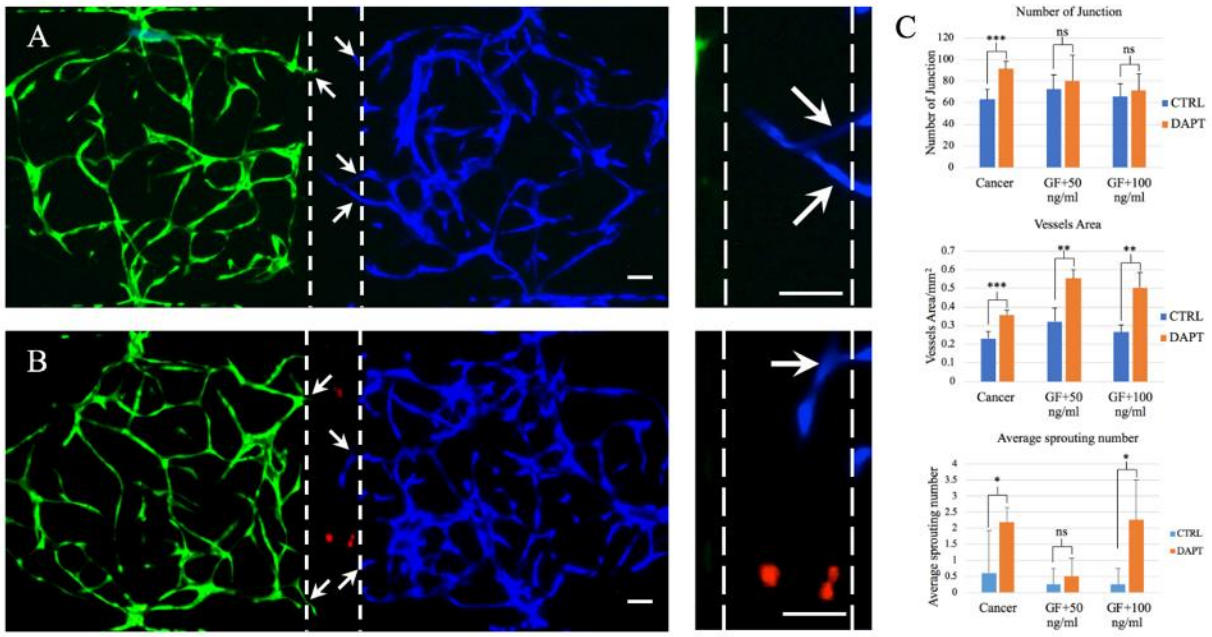

Figure 2.5 Mimic of NOTCH knockout for tumor and chemical induced angiogenesis
(A) & (B) NOTCH knockout mimicked by DAPT treated network and control network. The connecting channel T_M in (A) is loaded as the GF+100 condition, and T_M in (B) is loaded as the cancer condition. The high magnified image is the zoom in view for the sprouts in the connecting channel. The white arrows point to the angiogenetic sprouts. The dashed lines are the position of post arrays. All scale bars are 100μm. DAPT treated HUVECs are labeled with Azurite blue, control HUVECs are labeled with Venus-GFP, and SW620 cells are labeled with mCherry. (C) Quantitative analysis of vascular network in tissue chambers and the angiogenetic sprouts towards the connecting channel.

The results show that the vascular network formed by DAPT treated HUVECs has more junctions and larger vessel areas (Figure 2.5) than control group does. And the vessel length is almost the same (figure not shown), thus the vascular network formed by DAPT treated HUVECs have larger vessel diameters due to the larger vessel area. Specifically, in cancer condition, the number of junctions is 91.40±6.58 in DAPT treated network and 62.80±9.52 in control network. The number of junctions in GF+50 and GF+100 conditions are also higher in the DAPT treated network than the control network, but not statistically significant. The vessel areas in all the conditions show significantly higher values in the DAPT treated networks. In cancer condition, the vessel area is 0.36±0.03mm^2 in DAPT treated network, and 0.23±0.04mm^2 in control network; in GF+50 condition, the vessel area is 0.55±0.05mm^2 in DAPT treated network, and

0.32±0.07mm2 in control network; in GF+100 condition, the vessel area is 0.50±0.08mm2 in DAPT treated network, and 0.26±0.04mm2 in control network. For the tumor induced angiogenesis, we observed ECs sprouts towards the tumor in the connecting channel for both DAPT treated and control network (Figure 2.5 (B)), and the DAPT treated network has more sprouts. Specifically, the average sprouting number is 2.2±0.45 in DAPT treated network and 0.6±1.34 in control network. For the chemical induced angiogenesis, we observed dose response in GF+50 and GF+100 condition for the increased angiogenic sprouting in DAPT treated network towards the connecting channel (Figure 2.5 (A) & (C)). In GF+50 condition, the average sprouting number is 0.50±0.58 in DAPT treated network and 0.25±0.50 in control network; in GF+100 condition, the average sprouting number is 2.25±1.26 in DAPT treated network and 0.25±0.50 in control network.

Discussion

The HT-MTCS is a standardized platform integrated with 96 well plate. The fabrication process is fairly straightforward and can be carried out on a bench top and can easily scale up for mass production. The well plate provides the medium reservoir for the hydrostatic pump needed for the system and the fixed position for operation and data acquisition. Such platform can be easily operated with standard equipment, such as liquid handling robot and imaging system, for large scale in vitro tissue culture. Besides the low consumption of cell and reagent in the platform, our design has advantages typical of microfluidics technology in building integrated micro tissues with well-defined hydrodynamic and biochemical microenvironment. We've demonstrated the capability of forming vascularized tissue with various cell compositions and ECM formations. More complicated tissue structure and flow control can be applied to the HT-MTCS for specific research. For example, the defined position of tumor and healthy tissue, and perfusable vascular

network, combined with controllable flow, allow researchers to study the entire process of metastasis in a single platform with EC formed vasculature. Specifically, we can build a primary tumor in T_L and observe the intravasation into the vasculature by using the horizontal flow to guide the circulating tumor cells (CTCs) to T_R, then observe the CTCs' extravasation into the T_R tissue to form a secondary tumor. The NOTCH knockout mimicking experiment also indicates another kind of application to build a tissue structure that could co-culture wild type and knockout cells in a single platform with controlled environment and study their interaction. In our experiment, we notice that the angiogenetic sprout number is similar between the cancer and GF+100 condition, but the correlation between the two conditions will need further research. This might provide another angle to study the angiogenesis mechanism.

Despite the advantages we have showcased for HT-MTCS, we still notice some limitations of our design. First, the flow in the chip is restricted by the hydrostatic pressure of medium reservoirs, or the height of wells. This limit has been noticed already from our previous high throughput design[55]. Compared with our previous high throughput design, we decouple the medium inlets to allow better control of the flow through each tissue culture region. This modification can provide different composition of medium or drug solution to T_L and T_R, but the pressure gradient is impaired in the horizontal flow mode. To address this, we are working on 3D printed well insert to increase the well height (Figure 2.6 (A)). This could generate higher pressure input to the tissue chamber and apply minimum changes to the whole system. Another method is to apply active pumps to the system. We're building a peristaltic pump that can fit in our required flow rate and provide circulation to our system (Figure 2.6 (B)). This will not only provide higher flow rate, but also reduce the labor during culture process. It will also assist the metastasis study by keeping the CTCs in a close loop of circulation.

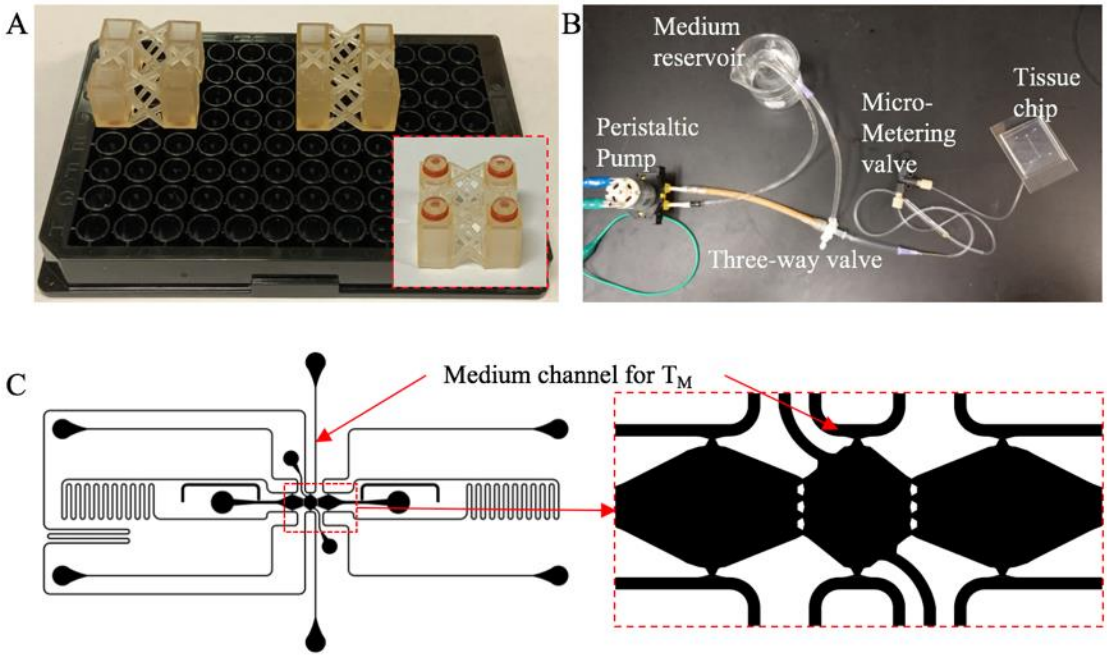

Figure 2.6 Add-ons and modification of the device design
(A) 3D printed well insert to provide higher pressure input to the tissue. (B) peristaltic pump prototype for prolonged circulation of medium. (C) prototype design with individual medium channel to T_M.

Another limitation is the difficulty of further increasing the tissue types. The current design applied individual medium channel to T_L and T_R, but the mass transport to T_M is still relying on the neighboring chambers. We also have a prototype with individual medium channel to T_M (Figure 2.6 (C)). This design has a very long medium channel to bypass all the elements related to T_L. If we keep increasing the tissue culture regions, we cannot solve the space arranging problem to avoid the crossover of gel inlet and medium channel. As a result, a new liquid/gel interface need to be built to separate the medium channel and tissue culture regions into different PDMS layers.

CHAPTER 3: MULTI-LAYERED CONFIGURATION FOR A MODULAR MICROFLUIDIC SYSTEM TO GENERATE LARGE SCALE PERFUSABLE MICROVASCULAR NETWORKS

Background

As previous described, the tissue chambers and culture medium channels HT-MTCS were all in one device layer. This single-layer configuration has limited space for both the tissues and the culture medium channels, which resulted in a crowded layout and limited design options to the position of the microvascular networks. It also limits the flexibility to design multiple interconnected vascularized micro tissues on the same platform.

Potential solutions to overcome these problems stem from the concept of modular microfluidic systems, of which different components are separated and individually designed and fabricated[85-87]. Here, we propose a modular approach with a multi-layered configuration that separates the tissue chambers and culture medium channels into different device layers[88], where both layers can be fabricated and modified individually. This allows the tissue chambers to be densely packed, while culture medium supply can flow vertically into multiple tissues. More importantly, the two device layers can be combined freely, forming various flow conditions inside an array of tissue chambers. As interstitial flow is a key factor to regulate capillary growth[65], this platform can be used to create a wide range of flow conditions to study vasculogenesis and angiogenesis.

In this chapter, we report a two-layer PDMS modular microfluidic system and demonstrated large scale microvascular networks that covers more than 14mm^2, with a vessel density of 12mm/mm^2. To prevent hydrogel bursting into the culture medium channels during gel

loading into the tissue chambers, a novel plastic mold-based fabrication method was developed to make semi-closed rhombic medium channels. Complex microvasculature with varying morphology were grown using this two-layer modular microfluidic system. The vertical vascular anastomosis between two device layers was demonstrated, and 70kDa FITC-dextran perfusion succeeded without leakage at both the anastomotic connections and the microvascular networks, demonstrating a strong barrier property of the vasculature lumens, and a tight interconnection between the culture medium channels and the vascular capillary network underneath. Ultimately, this flexible and scalable modular platform is able to accommodate multiple organs on a chip interconnected via perfused microvasculature, forming the basis of a functioning 'body-on-a-chip'.

Materials and methods

Modular microfluidic system based on multi-layered configurations

Microvascular networks were generated in a diamond shape tissue chamber in our previous works [70, 72]. However, in this configuration, the culture medium channels and tissue chambers were in the same PDMS layer, limiting the space and layout flexibility for the channels and tissues, as well as a range of fluidic conditions to induce vascular formation. Here a modular microfluidic system using two PDMS layers is developed, enabling large-scale, interconnected, multi-chamber microvascular networks with a spatial flow control. In this approach, the channels to delivery culture medium and the tissue chambers are fabricated separately in two PDMS layers. As shown in Figure 3.1(a, b, c), the tissue chambers and culture medium channels are aligned and bonded to form functional devices with various channel configurations. For the medium channels in the Upper layer, they are designed with 4 lines to supply the culture medium to the tissue chambers underneath. For the tissue chambers in the Bottom layer, the previous basic design of diamond

shape was modified and designed with three types of tissue chambers, including diamond, half-rectangle and rectangle shape, to form various configurations. Because different Upper layer and Bottom layer can be combined in various degrees of freedom, and different channel-chamber combinations can form various fluidic flow profiles to induce vascular formation, this system constitutes a modular vascularized micro organ system.

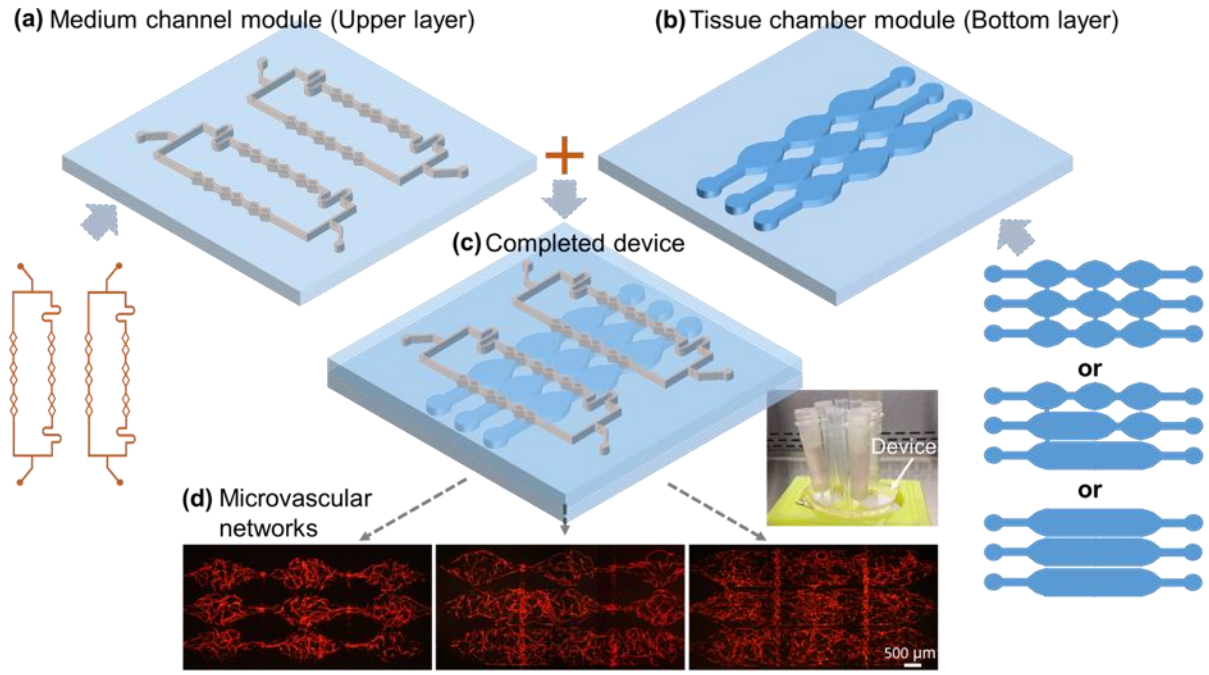

Figure 3.1 The modular microfluidic system, combining by two PDMS layers
(a) Medium channel module (Upper layer) and (b) Tissue chamber module (Bottom layer). There are different channel designs used in these two modules. (c) A completed two-layered device shows the medium channels and tissue chambers in different layers. (d) Large scale perfused microvascular networks generated by using different configurations.

PDMS device design and fabrication

Since various combinations of Upper and Bottom layers can be used in our system, one combination is used here as an example to describe the concept of device design and fabrication, shown in Figure 3.2. In the Upper layer, the straight part of the culture medium channel has a 100-μm width, and its rhombic part has a 150-μm width. The bifurcated channels in the rhombic part

has a 30-μm width. In the Bottom layer, the tissue chamber array consists of three types of tissue chambers, including a diamond, a half-rectangle and a rectangle shape. The diamond shape chambers are similar to the design in our previous works [70, 72].

For each device, the Upper layer and Bottom layer were both made of PDMS (Sylgard-184, Dow) casted from SU-8 patterned silicon wafers using standard soft lithography techniques [89]. The height of the microfluidic channels and the tissue chambers were all 100μm. One Upper layer and one Bottom layer was aligned as shown in Figure 3.2 (a) under the microscope and bonded by plasma bonding. The culture medium channels in Upper layer and the tissue chambers in Bottom layer were crossed after bonding. The crossed areas form an opening space connecting the medium channels and the tissue chambers that are now called communication pores, as shown in Figure 3.2 (b, c). After plasma bonding, bottomless plastic vials served as culture medium reservoirs were glued on top of the inlets and outlets of the medium channels. Fabricated devices were autoclaved at 121°C for 30 minutes before used for subsequent experiments.

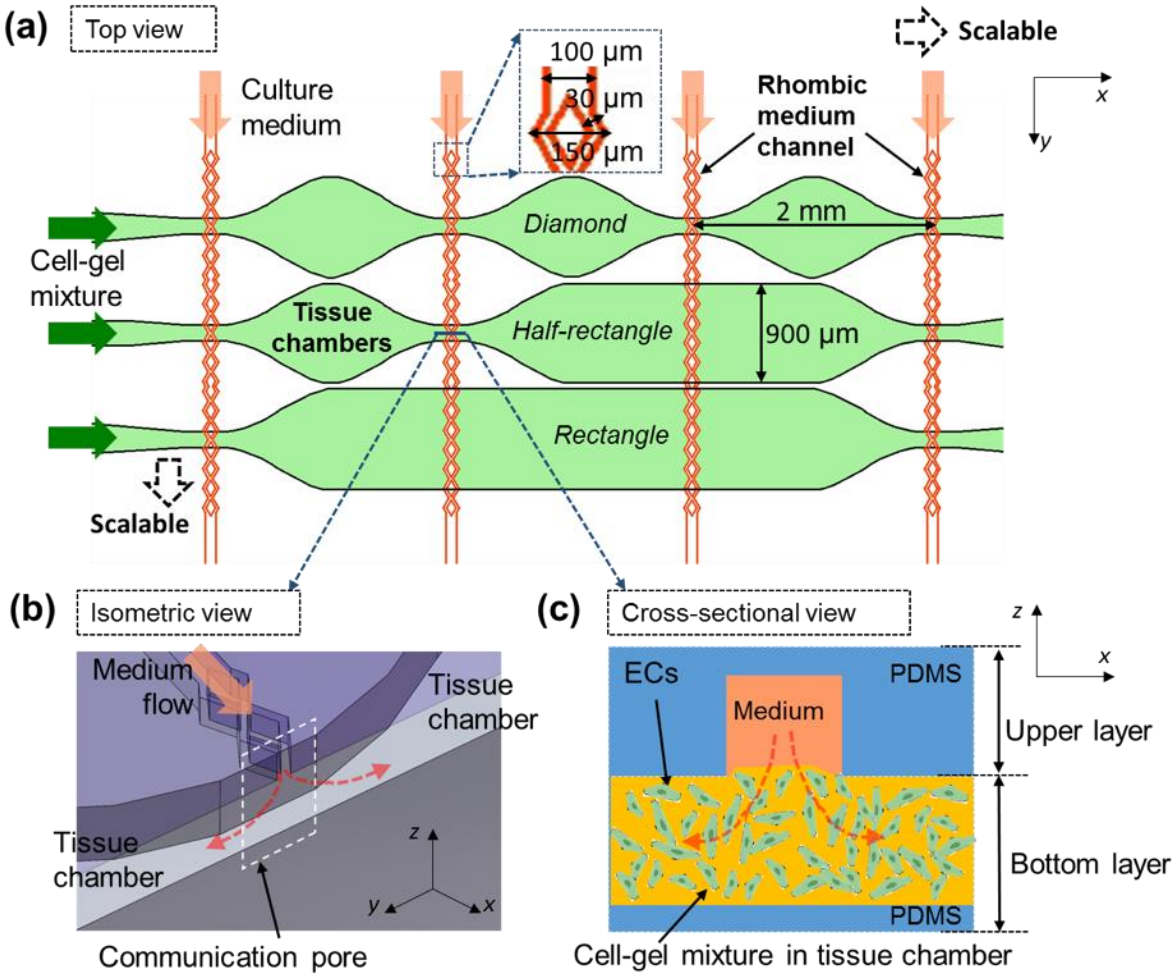

Figure 3.2 Schematic drawing of an example device and the simulated flow conditions inside
(a) Top view of the device layout with a 3x3 tissue matrix. Cell-embedded fibrin gels are loaded into bottom tissue chambers. Then the culture medium is supplied through upper medium channels. (b) The isometric view of a communication pore shows how the medium flows from the medium channel to the tissue chamber. (c) The cross-sectional view of the communication pore shows how the ECs form lumens connecting the medium channel and the tissue chamber.

Rhombic medium channel design and fabrication

To provide sufficient culture medium and prevent gel bursting, a rhombic medium channel was designed and fabricated as shown in Figure 3.3 (a) and Figure 3.4 (c). The opening width of the bifurcated rhombic channels was 30μm. The PDMS layer of these rhombic medium channels were fabricated as shown in Figure 3.4 (a). After the original PDMS layer was replicated from the SU-8 wafers, it was then used as a master mold to cast a liquid plastic replica (a customized

polyurethane, Smooth Cast 310, Smooth-On Inc). After 24 hours, the solidified plastic replica was demolded. The microfluidic feature dimensions were slightly reduced in this plastic mold, since the liquid plastic underwent a volumetric change during the curing process, resulting in a linear dimensional shrinkage (about 4% mentioned in [90]) compared to the original SU-8 mold. The final PDMS layer contains the rhombic medium channels was casted using this replicated plastic mold.

Cell culture

Human endothelial colony forming cell-derived endothelial cells (ECFC-ECs) were isolated from cord blood as previously described [81] and expanded on gelatin-coated (0.5%) flasks in EGM-2 medium (Lonza). ECs were transduced with lentvirus constructs (Addgene) to express mCherry fluorescent protein and used between passages 4 to 7. Normal human lung fibroblasts (NHLFs) were purchased from Lonza, cultured in DMEM (Corning) containing 10% Fetal Bovine Serum (FBS, Gemini Bio Products), and used between passages 5 to 8. All cell types were grown in a 37°C/5% CO_2/20% O_2 incubator in 100% humidified air before used in experiments.

Cell loading procedures and on-chip culture

The cell loading procedures includes cell-gel mixture preparation, cell-gel mixture loading into devices, medium channel coating and culture medium loading. The whole process has to be done within 90 minutes. **First**, the cell-gel mixture was prepared by suspending ECs ($5\times10_6$ cells/mL) and NHLFs ($5\times10_6$ cells/mL) in fibrinogen solution (10mg/mL, Sigma-Aldrich) [69-72]. **Second**, the suspension was mixed with 50U/mL thrombin (Sigma-Aldrich) for a final concentration of 3U/mL and quickly injected (less than 10 seconds) into the tissue chambers through the gel loading port (Green arrows in Figure 3.2 (a)) using a micropipettor. The gel was

allowed to polymerize in the incubator at 37°C for 15 minutes. **Third**, laminin (1mg/mL, Life Technologies) was introduced through the medium loading port (Red arrows in Figure 3.2 (a)) to coat the inner surface of the medium channels. **Finally**, EGM-2 (Lonza) culture medium was supplied through the same culture medium channels (Red arrows in Figure 3.2 (a)) under a relative stable pressure drop from inlets to outlets. After cell loading, cell culture medium in the vials was refilled and the fluidic direction was reversed every 48 hours for 10 days to induce vascular formation.

Dextran-FITC perfusion

To validate anastomosis of the microvascular networks and to evaluate vascular perfusivity, Dextran-FITC perfusion test was conducted. Medium was first replaced by DPBS with a similar hydrostatic pressure profile, and the device was positioned onto a microscope stage. Then 70kDa FITC-dextran (final concentration of 50μg/mL, Sigma-Aldrich) was added to the medium reservoir at the highest hydrostatic pressure side, which allowed 70kDa FITC-dextran to perfuse through the culture medium channels to the microvascular networks. A time-lapse image sequence was recorded for 10 minutes to capture 70kDa FITC-dextran flow in the device.

Data acquisition and analysis

Bright-field and fluorescent images were obtained using an optical microscope (Olympus IX51 and Canon 5D II camera). Confocal images were obtained using a confocal laser scanning microscope (A1Rsi-N, Nikon). Images of the capillaries were processed by ImageJ (Ver. 1.47, NIH) and AngioTool (Ver. 0.6a, NIH) to calculate the Total Vessels Length, Total Number of

Junctions and Average Vessels Length. Data are shown as mean ± standard deviation (SD) unless stated. Estimated means, and standard deviation are calculated using Microsoft Excel.

Results

Modular microfluidic system provides various flow conditions in tissue chambers

The presented modular microfluidic system based on a two-layered configuration can provide design freedom to combine and connect a large number of tissue chambers. As previously demonstrated, ECs are responsive to interstitial flow during vasculogenesis, and interstitial flow can be controlled spatially to grow microvascular networks with different mass transport configurations [71, 91], it is possible to regulate the vessel growth pattern and obtain large-scale microvascular networks in our presented modular microfluidic system by optimizing the interstitial flow profiles. Therefore, we first investigated the interstitial flow conditions, such as pressure gradient and shear stress distribution in different tissue chambers. Numerical fluidic simulations were conducted using COMSOL Multiphysics (Ver. 5.2a). The numerical inputs used in these simulations, including the material properties of fibrinogen hydrogel and the hydrostatic pressure profile used to generate fluidic flow, were based on our previous works [55, 72, 73].

Figure 3.3 (a) shows an example of these simulation results. In this simulation, fluid flow is driven by hydrostatic pressure inside the microfluidic channels and fibrinogen hydrogel are placed inside the tissue chambers. The tissue chamber has three different designs: Diamond, Half-rectangle and Rectangle shape, aimed to investigate how different tissue chamber shapes influence the interstitial flow profile inside. Rainbow color scheme represents the pressure gradient and red lines show the flow stream. By drawing profile lines across these chambers, quantitative analysis of the flow conditions can be performed. Because fibrinogen hydrogel is a porous material,

interstitial flow of culture medium through it was simulated, as shown in Figure 3.3 (b). Culture medium was perfused from the Upper layer medium channels to generate interstitial flow across all lower tissue chambers, which provide stimuli for microvascular growth.

As shown in Figure 3.3 (c), the pressure drop from the left end to the right end of one chamber is approximate 50Pa at different time points during one full culture cycle. Based on our previous data [72], this two-layered configuration provided sufficient pressure gradient to stimulate vessel growth. Different tissue chamber designs were compared to estimate the shear stress distribution, a key factor that regulates vascular development. The hypothesis is that shear stress distribution will determine the growth and connectivity of the microvascular networks inside the chambers, especially in term of vessel length and density [65, 92]. Shear stress distribution inside the diamond, half-rectangle and rectangle-shaped tissue chambers was shown in Figure 3.3 (d, e, f), respectively. Although the lowest shear stress in these three chamber designs are almost the same, the rectangle-shaped chamber has the lowest average shear stress and a more even distribution. Here we chose this configuration with three different shapes in one device as an example to calculate different interstitial flow profiles. In the real experiments, any layout can be used as long as they can be aligned to the culture medium channels. By using different shapes for the tissue chambers, various interstitial flow profiles are provided in this modular microfluidic system, which is an ideal platform to optimize conditions required to generate larger and denser microvascular networks.

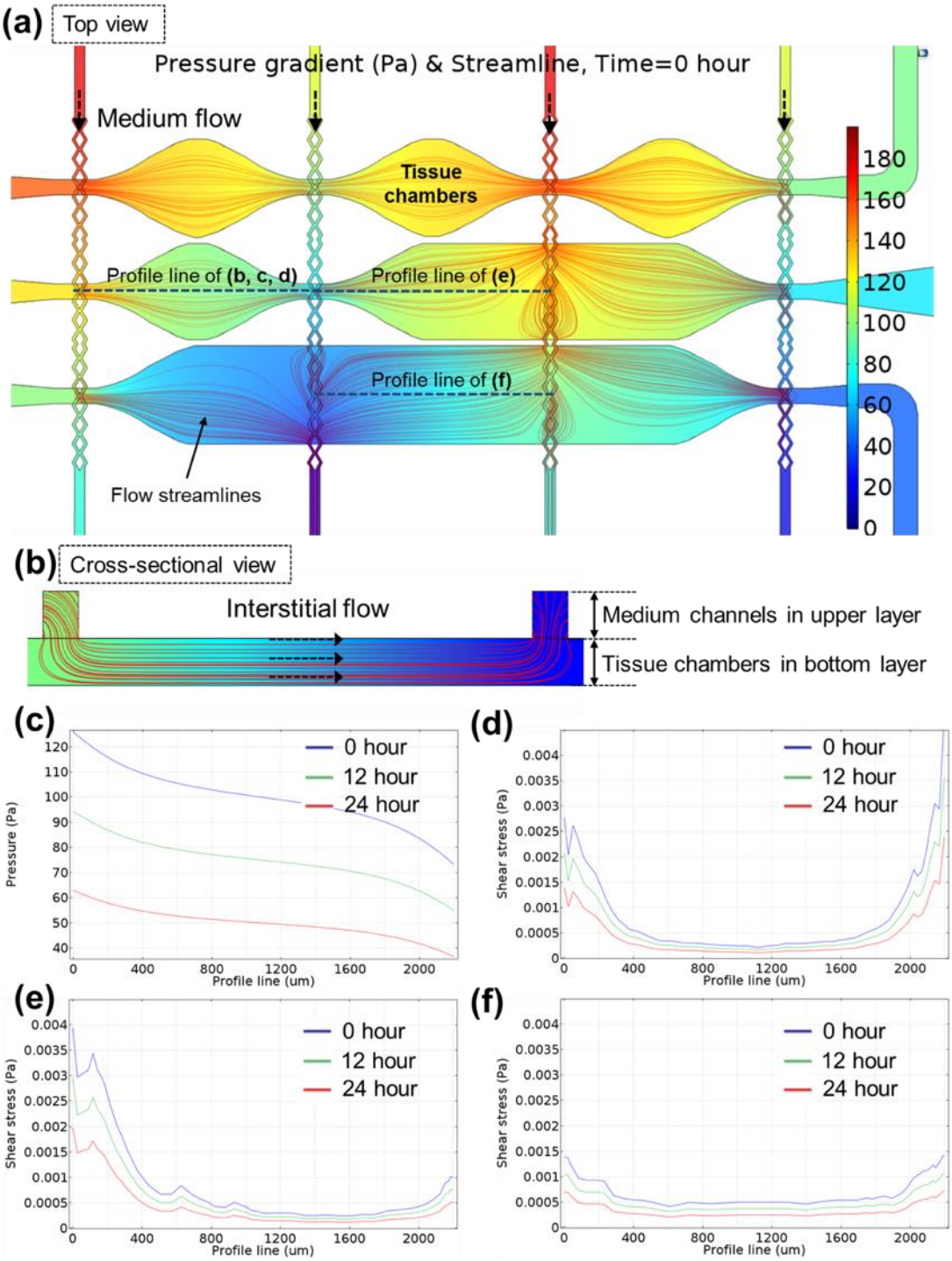

Figure 3.3 Numerical simulations of the flow inside tissue chambers

(a) The pressure gradient and flow stream of 3 types of chambers, including Diamond, Half-rectangle and Rectangle shape. (b) Culture medium was diffused from the upper medium channel into the tissue chamber, generating interstitial flow inside. (c) The pressure drop across one tissue chamber was about 50 Pa, which was sufficient for stimulating the vessel growth. The shear stress distribution inside the (d) Diamond, (e) Half-rectangle and (f) Rectangle shaped tissue chambers were different, which provided various flow conditions to grow larger and denser microvascular networks inside.

Semi-closed rhombic medium channels prevent gel bursting during cell loading

Based on our design concept and numerical simulations, this two-layered configuration provides flexible design to spatially pattern the culture medium channels relative to the tissue chambers. However, two challenges were posed in practice. First, we had to make sure the cell-gel mixture would not burst into the Upper layer medium channels and clog them during the loading process. Second, the culture medium needs to be easily introduced into the medium channels and perfused into the hydrogel underneath.

As shown in Figure 3.2 (c), these is an opening space between the medium channels and the cell-gel mixture in tissue chambers. This opening space has to be large enough to provide sufficient culture medium for cell growth. However, too large of this opening may cause gel bursting into the medium channels during the cell loading process[73]. Therefore, to prevent gel bursting, pillars were first utilized. These was no gel bursting in this case, but when culture medium was introduced into the medium channels, air bubbles were easily trapped by these pillars because of the hydrophobic surface of PDMS. These bubbles block the culture medium from flowing into the hydrogel. Therefore, a novel rhombic shape medium channel was employed. Because the 2 divided channels cross every 100μm in this design, bubbles can be easily flushed out of the channels during the loading of culture medium. Experiments demonstrated that this rhombic medium channel design can prevent air bubbles exceptionally (Movie 3.1).

The crossing sections of the rhombic medium channels act as communication pores as shown in Figure 3.4 (c). As these pores are relatively wider than the divided rhombic channels, gel bursting are more likely to take place at these pores. To prevent gel bursting while keeping the rhombic shape to prevent air bubbles, the dimensions of these pores had to be reduced during

fabrication. An ideal solution is to partially make the bottom opening width smaller to be semi-closed, but not to uniformly reduce the channel width of the diverged rhombic channels.

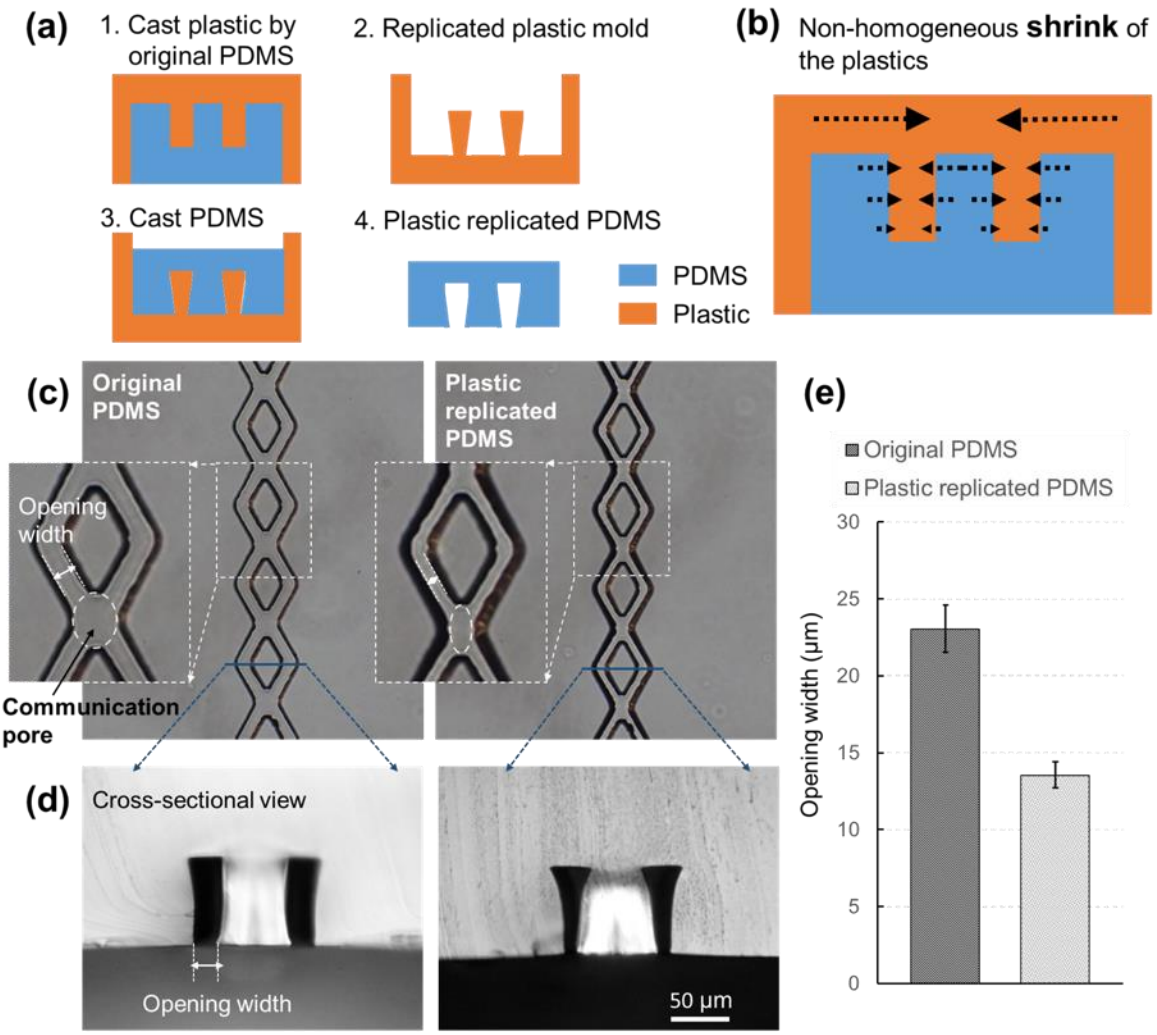

Figure 3.4 Semi-closed rhombic medium channels was fabricated using plastic molds
(a) Fabrication procedures of the plastic replicated PDMS with the semi-closed rhombic medium channels on it. (b) The inhomogeneous shrink mechanism makes the PDMS channel to be semi-closed. (c) The images of original PDMS and plastic replicated PDMS show the size decrease of the opening width and the communication pores. (d) The cross-sectional view clearly shows the semi-closed medium channels. (e) The quantitative data demonstrate that the opening width can be reduced to be about half of the original channels. Mean ± SD, n=8.

In this case, a type of semi-closed rhombic medium channel was obtained based on our novel fabrication approach using the plastic molds. Figure 3.4 (a) shows our plastic replication method used to reduce the opening width. Because the plastic will shrink at a rate of 4% in linear

dimensional size during solidification[90], the feature dimensions on these plastic molds are slightly different compared to the original SU-8 mold. In theory, the shrinkage ratio is isotropic. However, the plastic mold casted from the original PDMS was not isotropic, due to the geometry of the microfluidic channels that resulted in a non-isotropic shrinkage in the horizontal direction, as shown in Figure 3.4 (b). The bulk plastics shrink more in actual distance, shaping the plastic mold as show in Figure 3.4 (a2). Therefore, the opening width in the final PDMS channels replicated from these plastic molds were smaller compared to that casted from original SU-8 mold, as shown in Figure 3.4 (c). As a result, the communication pores became smaller. The cross-sectional images of the channels in Figure 3.4 (d) show a narrow opening of the medium channels. In Figure 3.4 (e), quantitative analysis of the data demonstrated that the opening width could be reduced to approximately half of the original channels. This fabrication method is very simple and can modify the channel shape in a non-isotropic fashion.

Vertical anastomosis at the communication pores connects the microvascular networks and the medium channels

After the cell loading process, the devices were cultured for another 10 to 11 days to allow the ECs proliferate and form a lumenized microvascular networks inside the tissue chambers. Unlike the single-layer device, the ECs near the communication pores in the bottom tissue chambers grew vertically upward into the medium channels in the Upper layer, sealing the inner walls and forming connections between the medium channels and the tissue chambers, as illustrated the schematic drawings in Figure 3.5 (a). This is due to medium flowing from the medium channels into the Bottom tissue chambers and creating a growth factor gradient that stimulates EC migration. This vertical migration eventually connects the microvascular networks

and the medium channels, forming a leakage-free sealing at the communication pores, which we called ‘vertical anastomosis’. Time lapse images in Figure 3.5 (b) clearly show ECs migrating toward the communication pores and resulting in vertical anastomosis.

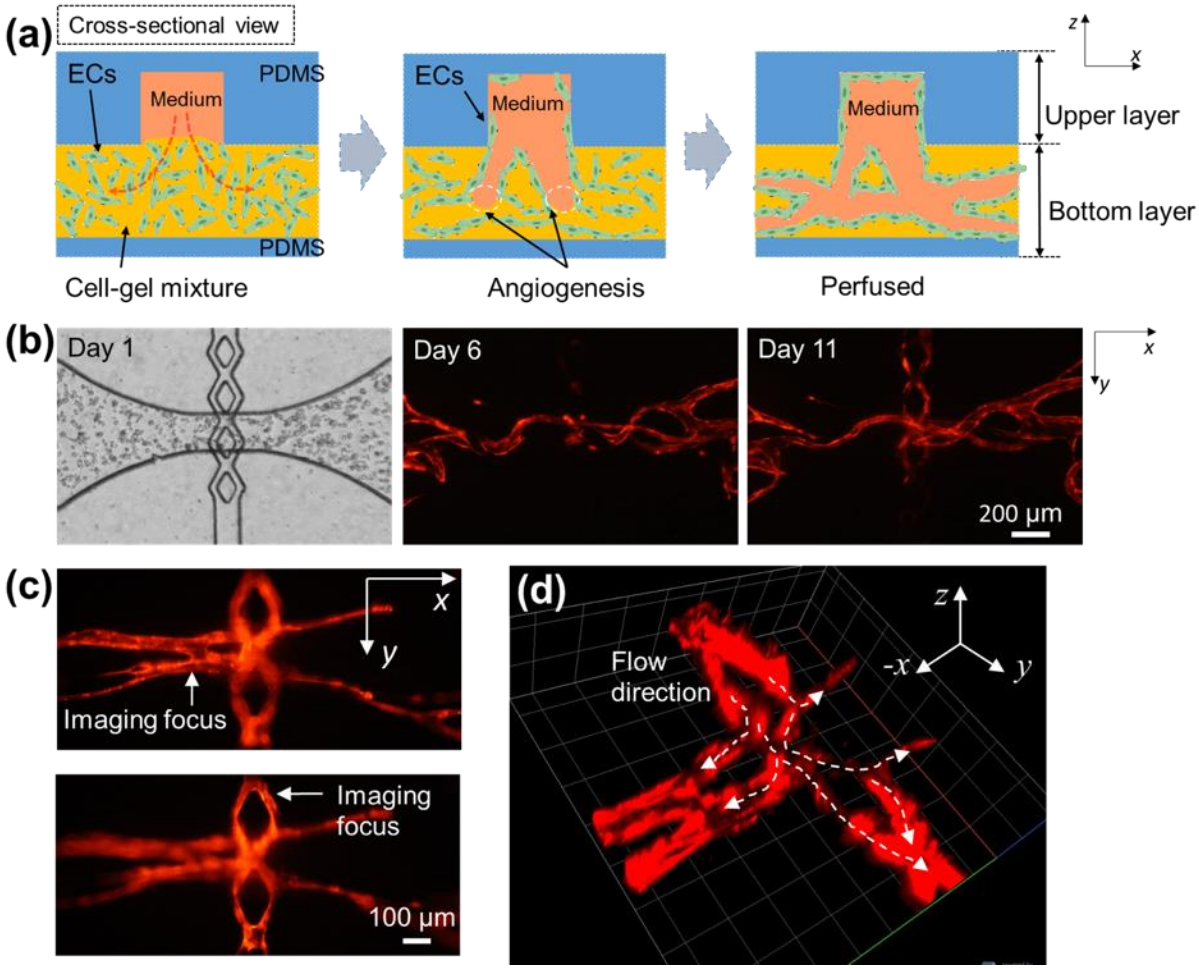

Figure 3.5 ECs grow vertically at communication pores to form a leakage-free sealing between microvascular networks and medium channels

(a) Schematic drawings of the vertical anastomosis at communication pores show that ECs seal the inner walls and form connections. (b) Time-lapse images clearly show the ECs grow at communication pores and form the connections. (c) Different focusing images demonstrate the connections between Upper and Bottom layers. (d) Confocal images show the full connections and how the culture medium flows though these connections into the capillaries.

Because the medium channels and tissue chambers are in two separate PDMS layers, at different positions on the z-axis, they cannot be focused under the same microscope view plane.

However, changing the focal view planes can confirm vertical anastomosis of ECs at the communication pores. As shown in Figure 3.5 (c), the focal view planes of vessel segments in the medium channels and those in the tissue chambers are about 100μm different in the z-direction, which matches the design of 200μm combined thickness of both the medium channel and the tissue chamber. Confocal images were obtained to better visualize complex connections between the microvascular networks and the vessel segments that lined the medium channels (Movie 3.2). These images confirmed anastomosis at the communication pores. As shown in Figure 3.5 (d), the microvascular networks inside the tissue chambers are fully connected to the medium channels in the Upper layer.

Large-scale microvascular networks generated in the modular microfluidic system

As a modular microfluidic system, one advantage is its scalability. We tested two different layouts of tissue chamber with a 3-by-3 and 3-by-5 matrices respectively to demonstrate the scalability of our system. As shown in Figure 3.6 (a), microvascular networks were successfully generated using both 3-by-3 and 3-by-5 chamber matrices. Furthermore, vertical anastomosis was observed in all cases. While scaling up from a 3-by-3 to 3-by-5 configuration may not seem significant, we used this example to demonstrate the feasibility and scalability of our modular microfluidic system to larger tissue chamber matrices of N by N.

Another advantage of this modular system is its flexibility, especially the capacity to generate various fluidic conditions from different designs of the tissue chambers. These fluidic conditions could guide the spatial patterning of larger and denser microvascular networks. A tissue chamber design containing three shapes was utilized to investigate how different fluidic conditions influence vascular formation. As shown in Figure 3.6 (b), diamond, half-rectangle and rectangle

chamber shapes were used to generate tissues in different geometries. 70kDa FITC-dextran was perfused to quantitatively analyze the vessel morphology. Software AngioTool (National Cancer Institute) was used to calculate the total vessel length, total number of junctions and average vessels length, that together represent the morphological properties of the microvasculature. The quantifications (Figure 3.6 (b)) show that rectangle shaped vascularized tissue has the highest value in all three parameters, identifying the rectangle tissue chambers as our selected configuration to generate large-scale microvascular networks. This confirms the fluidic numerical simulation results of the three types of chambers in Figure 3.3, indicating that lower shear stress promotes the formation of longer and denser vessels [64, 65, 92].

Figure 3.6 (c) illustrates a large-scale microvascular network constituting three rows of the rectangle shaped tissue chambers. The microvascular networks robustly developed in the whole tissue chamber array and formed anastomotic connections with the Upper layer rhombic channels at the communication pores. Quantitative morphological analysis was conducted, and the entire microvascular networks covered more than 14 mm^2, with a vessel density of 12 mm/mm^2.

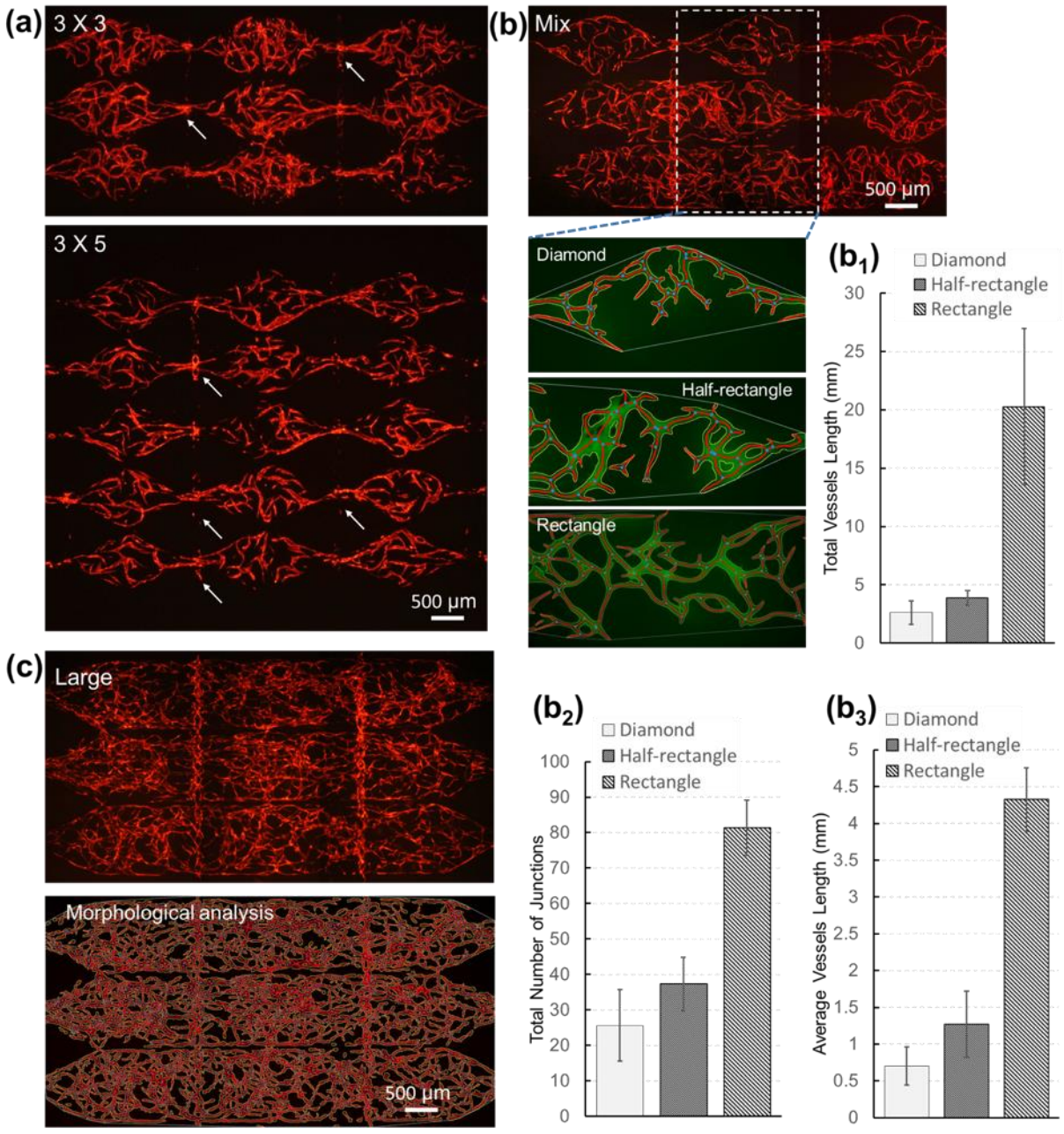

Figure 3.6 Various microvascular networks are generated in the modular microfluidic system
(a) The scalability was demonstrated by expanding the tissue chamber matrixes from 3x3 to 3x5. (b) Different morphological properties of the capillaries generated using Diamond, Half-rectangle and Rectangle shaped chambers were analyzed. Rectangle shaped tissue chambers generated largest scale of capillaries. A large-scale microvascular network covering more than 14 mm^2 with a vessel density of 12 mm/mm^2 was generated by the tissue chamber containing three rows of Rectangle chambers. Mean ± SD, n=6.

Fluorescent dextran perfusion demonstrates the microvascular networks and the medium channels are tightly connected

To validate the integrity of the microvascular networks and the vertical anastomosis at communication pores, 70kDa FITC-dextran was utilized to perfuse through the whole device. 70kDa dextran is chosen since it has a molecular weight close to human serum albumin (MW ~66.5kDa), the main protein of human plasma, making it suitable to test endothelial barrier function. Figure 3.7 (a) shows time-lapse images of FITC-dextran perfusion from the medium channels into the microvascular network. After FITC-dextran was loaded into the medium inlets, a fluorescent microscope was used to continuously monitor dye flow at the communication pores. Time-lapse recording started when the green fluorescence appeared in the medium channels. Within 2 minutes, FITC-dextran began to perfuse into the microvascular network through the communication pores. Over time, the fluorescence intensity in the vessel lumen increased due to accumulating dextran influx. After 6 minutes, FITC-dextran passed through the vessels near the communication pores and filled the entire microvascular networks inside the tissue chambers underneath. This demonstrated the connectivity and perfusability of the microvascular networks. Furthermore, no FITC-dextran was observed outside of the vessels during the whole perfusion test, including the communication areas where ECs formed the vertical anastomosis. As shown in Figure 3.7 (b), after about 15 to 20 minutes, a whole microvascular network was filled with FITC-dextran, and there was no obvious non-physiological leakage of FITC-dextran, especially at the full range of the communication pore area. Therefore, a leak-free sealing at the communication areas resulting from the tight interconnections between the microvascular networks and the medium channels was confirmed. Additionally, a strong endothelial barrier property of the microvascular networks, and the tightness of the anastomosis was demonstrated.

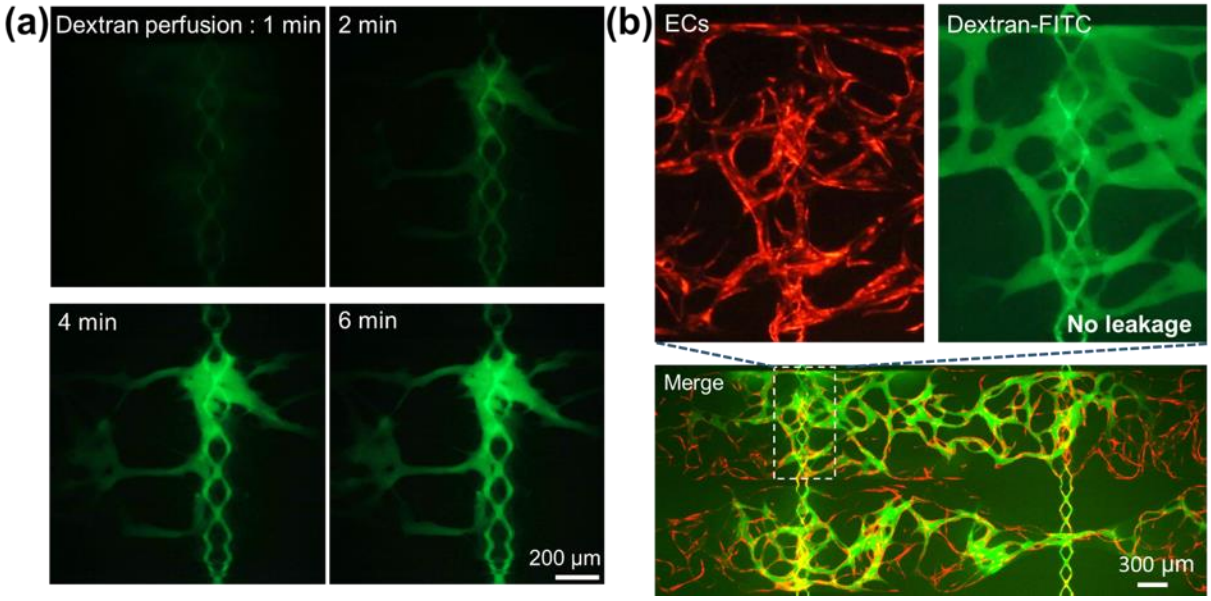

Figure 3.7 70kDa FITC-dextran perfusion demonstrated tight interconnections between the microvascular networks and medium channels

(a) Time-lapse images of the FITC-dextran perfusion from medium channels into capillaries show the connectivity and perfusability. (b) The whole perfused microvascular network demonstrated the strong barrier property of the microvascular networks, and the tightness of the anastomosis.

Discussion

The presented microfluidic system is intrinsically modular, as different patterns of medium channels in the Upper layer and different patterns of tissue chambers in the Bottom layer can be independently configurated. Although the medium channels presented in this paper are coupled (2 medium channels have the same inlet), decoupling channels with separate inlets can provide more flexibility to control the pressure gradients inside the tissue chambers. The tissue chambers on the Bottom layer can also be flexibly designed. In previous designs, it is difficult to introduce cells or chemical compounds into the ECM after the microvascular networks have formed, since there is no secondary channel connected to the ECM. However, with this two-layer configuration, adding more channels on the Bottom layer to provide additional routes to introduce cells afterward or to collect intervascular efflux for quantitative analysis becomes feasible. Another interesting idea is

to connect multiple rows of tissue chambers which are separated in the single layer configurations. Using the vertical anastomosis configuration described here, direct communication between each tissue row is made feasible. If different cell types are loaded into different rows, the communication between these different tissue chambers can be realized through the capillary networks in between or the microfluidic channels above (representing arterial or venule vessels). Not only can multiple different tissues be connected on this platform, one can have same tissues (organs) in an array on the same layer and deliver drugs in one chamber and see how it couples and impacts other tissues connected to it. For example, one can have "healthy" organs in one chamber and deliver therapeutic drugs to "diseased" organs in another chamber to evaluate side effects. Since immune responses usually require cell migration, one could create a scenario to observe immune cells in one chamber respond to infarction or lesion in another chamber. Another example is to create tissue chambers with different endothelial cell densities and see how they respond to various treatments. Since different organs have different vascular densities one can utilize this platform to recapitulate the organ vasculature physiology. Ultimately, this platform will enable a more complex and physiological relevant multi-organ-on-a-chip or 'body-on-a-chip' system to study the interactions between different organs, or to validate the circulatory functions of these microvascular networks. Beyond the two-layered device presented in this work, a multi-layered configuration with more than 2 layers could provide higher throughput, and the possibility of thicker tissues towards studying larger viable vascularized tissues that mimic *in vivo* dimensions.

To create the vertical two-layer platform, a plastic mold fabrication method was developed to provide the microchannels with a sufficiently narrow width towards the tissue chamber, which forms a capillary burst valve to help prevent gel bursting during the loading process. On the other hand, leveraging the non-homogeneous shrinkage due to the channel geometry, this plastic-

replication based fabrication approach can generate features along the z-axis to obtain special microfluidic channels with trapezoid cross-sectional shape.

The rectangle shaped tissue chambers used in this paper generated the densest microvascular network. Such results indicate the correlation of the tissue chamber geometry and the densities of the microvasculature formed inside. In other words, it is the fluid conditions inside the chambers that regulate microvascular development. It has been reported that fluid shear stress attenuates EC sprouting, but lower shear stress of interstitial flow directs endothelial morphogenesis and sprout formation [64, 92]. Here in the rectangle shaped tissue chamber, shear stress is lower than other shapes, which indicates lower shear stress resulted in more vessel sprouts and denser vascular networks. This finding is in correspondence with the findings in literature. In conclusion, the correlation between the chamber shape and the resulting vascular density gives us a potential approach to regulate vascular morphogenesis in our modular microfluidic devices according to the application needs.

CHAPTER 4: A HYDROSTATIC PRESSURE-DRIVEN PASSIVE MICROPUMP ENHANCED WITH SIPHON-BASED AUTOFILL FUNCTION

Background

Delivery of continuous and steady medium flow with accurate flow control is essential for 3D cell/tissue culture inside microfluidic devices, especially for recent organ-on-a-chip applications[1, 93]. As discussed in Chapter 2, the 3D printed well inserts provided a promising method to elongate the perfusion time for large scale in vitro tissues. However, the flow velocity is still descending during the culture period.

In order to generate constant and well-controlled flow in a microfluidic system, external active macropumps such as syringe pumps[94], electrokinetic pumps[95], and compressed air pumps[96] are commonly utilized. However, these types of bulky pumping equipment usually require external electrical power supplies and the corresponding control units, which make them unsuitable for point-of-care testing (POCT) applications that are typically portable diagnostic and monitoring devices[97]. For cell/tissue culture applications, since their culturing microenvironments need to be well maintained at 37°C in 5% CO_2, it is generally prohibitive since the external components of a macropump, such as electric wires or pressure control tubings, would all need to be placed into an incubator. Even though versatile on-chip active micropumps, such as membrane micropump[98], rotary micropump[99], diffuser micropump[100], ultrasonic micropump[101], electroosmotic micropump[102], electro-hydrodynamic micropump[103] and magneto-hydrodynamic micropump[104], have been developed to realize the flow operations with smaller footprints, the flow capacity is insufficient for long-term operation and they still need

control signals from external MEMS actuators or transducers to initiate or stop flow, making them difficult to operate inside incubators.

To overcome these limitations, researchers have developed a number of low-cost, zero electric power consumption, and portable on-chip passive micropumps by different approaches. The pumping mechanism based on pressure difference is the most straightforward and commonly used method in various microfluidics-based applications. Examples of this category of micropumps include the hydrostatic pressure-driven micropump based on either difference in medium height or controlled liquid evaporation rate between inlet and outlet medium reservoirs[72, 105], the surface tension-driven micropump based on the droplets with different sizes at inlet and outlet ports[106], the osmotic pressure-driven micropump based on the solutions with different concentrations[107], as well as the gas pressure difference-based micropump based on pre-vacuumed PDMS as negative pressure or gas generation through chemical reactions as positive pressure[108, 109]. Among these pumping mechanisms, each has its own pros and cons. In particular, the pressure difference-driven micropump could not regulate the flow rate well and is only suitable for short-term use. Therefore, it is unsuited to applications that need long-term stable flows, like 3D cell/tissue culture in microfluidic device. Another promising pumping mechanism takes advantage of capillary force by using either paper or textile wicking as thread pump[110, 111], or by designing a branched microstructure with different dimensions close to the outlet[112], which can generate the adjustable flow rates inside microfluidic channels. Due to the relatively small capillary force, the micropump based on this mechanism is not suitable for maintaining a high flow rate. Recently, another pumping concept by applying finger force on a deformable chamber[113] or pumping lid[114] was reported, which can generate the flexible flow rate control by the design of the pressure chamber or pumping lid with different dimensions or geometries. However, this

pumping mechanism is still difficult to operate inside an incubator with a closed environment for a long time. The siphon effect has been widely utilized as siphon valves in centrifugal microfluidic platforms[115], but is rarely utilized as the microfluidics-based micropump.

Here, we present a flexible hydrostatic pressure-driven passive micropump enhanced with siphon-based autofill function, which can realize autonomous and continuous fluid perfusion inside the microfluidic chip with accurately controlled steady flow for a long period of time. Compared with the previous on-chip passive micropumps, this micropump exhibits multiple beneficial features on a single platform, including: (1) small size (13×5×6 cm^3) and lightweight (60g) of single disassembled system for portability; (2) simple system setup with easily acquired components and ease of operation without peripheral equipment; (3) autofill function enabling long-term perfusion with constant flow rate; (4) flow rate driven by hydrostatic pressure drop can be easily and accurately adjusted; and, (5) multiplexed flow conditions are possible with high controllability and flexibility. As a model application that takes advantage of these capabilities, a microvascular network formation model under the stimulus of interstitial flow was established to demonstrate the effectiveness and power of this enhanced micropump.

Materials & Methods

Platform setup

Figure 4.1 shows the schematic diagram of whole platform setup, and its assembly process is presented in a movie clip (Movie S1 from reference[116]). A microfluidic chip attached with bottomless plastic vials as medium reservoirs at both inlet and outlet ports is mounted on the object stage of a clamping platform. To enable versatile applications, microfluidic chips with different microchannel geometries and dimensions can be integrated into this platform. A tightly sealed

conical tube with large volume (e.g. 50mL) is fixed by the clamping platform positioned above the inlet medium reservoir (IMR), which can function as the medium storage container (MSC). Two plastic tubings with different heights can function as siphons to establish the interconnection between MSC and IMR. Briefly, these tubings can be connected with conical tube at different location by using a needle and sealed by hot glue or epoxy. To ensure there is enough pressure to induce flow inside the low siphon to activate the siphoning effect, the top end of the straight low siphon should be positioned as close to the bottom of the MSC as possible. For the bent high siphon, its top end can be placed at any position above the top end of the low siphon, and its bottom end should be positioned at the desired height to maintain the desired constant liquid level inside the IMR. To control the liquid level at the outlet medium reservoir (OMR), another tube can be inserted into the OMR at the desired height to divert the redundant medium into a waste liquid container. Therefore, a constant hydrostatic pressure drop between IMR and OMR can be generated to supply the steady flow inside the microfluidic chip, which also enables the long-term perfusion with the assistance of siphon-based autofill function.

Principle of siphon-based autofill function

A siphon can be explained as a tube or pipe that allows liquid to flow from the higher level to the lower level without using pumps, which can be mathematically described by Bernoulli's equation. The Bernoulli equation is an approximate relation between pressure, velocity, and elevation, which is only valid for incompressible flow and is expressed as:

$$\frac{V^2}{2} + gh + \frac{P}{\rho} = \text{constant} \quad (1)$$

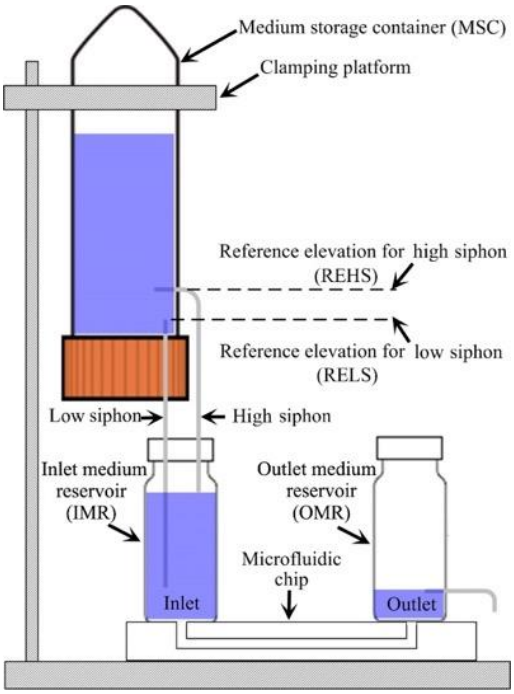

Figure 4.1 Schematic diagram showing the platform setup of the hydrostatic pressure-driven passive micropump enhanced with siphon-based autofill function

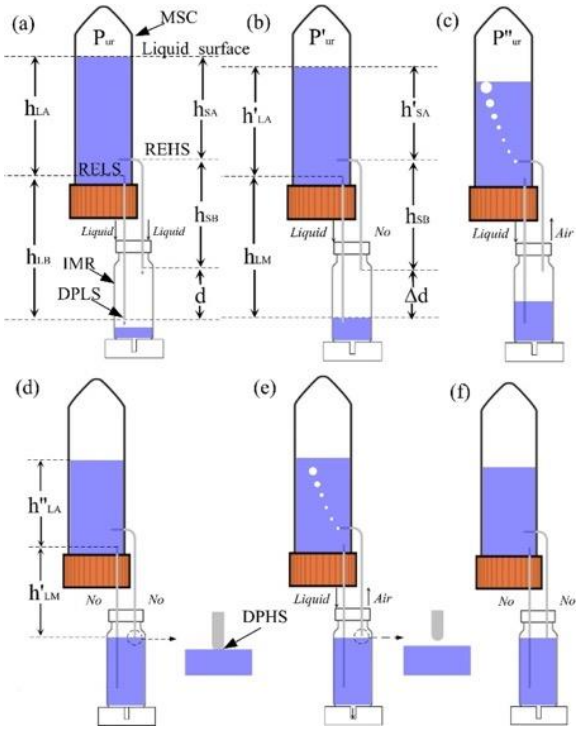

Figure 4.2 Schematic diagram showing the working principle of siphon-based autofill function
(a) Liquid from both siphons during the initial filling process. (b) No liquid inside the high siphon due to the decreased pressure inside the MSC. (c) Cavitation inside the high siphon and air bubbles appearing inside the MSC. (d) No liquid inside both siphons and no air bubble appearing inside the MSC when the liquid level inside the IMR reached to the DPHS. (e) Activation of refilling process when liquid level inside the IMR dropping below the DPHS. (f) Autonomous repetition of refilling process.

where V is the fluid velocity at the chosen point along the streamline, g is the gravitational acceleration constant, h is the elevation of the point above a reference plane, with the positive direction pointing upward, P is the pressure at the chosen point, ρ is the density of the fluid at all points along the streamline, and the value of constant will be the same at any point along a given steady state streamline with non-dissipative flowing fluid in the same fluid systems. For both the low siphon and the high siphon, their top ends are set as the starting points of the siphon and their corresponding horizontal planes are the reference elevations. As shown in Figure 4.2 (a), applying

Bernoulli's equation to the liquid surface inside MSC based on the reference elevation of the low siphon (RELS):

$$\frac{V_C^2}{2} + gh_{LA} + \frac{P_{\text{ur}}}{\rho} = \text{constant} \tag{2}$$

where V_C is the falling speed of liquid surface inside MSC, h_{LA} is the distance between the liquid surface inside MSC and the RELS, and P_{ur} is the air pressure inside MSC.

Compared with the large volume inside MSC, its volume change during each refilling loop is very limited. Therefore, by assuming that MSC is infinite, the falling speed of its liquid surface can be set to zero (V_C= 0). Equation (2) can be further simplified as:

$$gh_{LA} + \frac{P_{\text{ur}}}{\rho} = \text{constant} \tag{3}$$

Applying Bernoulli's equation to the draining point of the low siphon (DPLS) at the height of -h_{LB} relative to RELS before submerging into medium inside IMR (Figure 4.2 (a)):

$$\frac{V_L^2}{2} - gh_{LB} + \frac{P_{atm}}{\rho} = \text{constant} \tag{4}$$

where V_L is the flow velocity at the DPLS, and P_{atm} is the atmospheric pressure. After submerging, applying Bernoulli's equation to the low siphon positioned at the liquid surface inside IMR (Figure 4.2(b)):

$$\frac{V_R^2}{2} - gh_{LM} + \frac{P_{atm}}{\rho} = \text{constant} \tag{5}$$

where V_R is the flow velocity inside the low siphon at the position of liquid surface inside the IMR, and -h_{LM} is the distance of liquid surface inside IMR below the RELS.

Since the siphon is a single system, the constant in all of the above equations is the same. Setting Equation (3) and (4) equal to each other gives:

$$\frac{V_L^2}{2} - gh_{LB} + \frac{P_{atm}}{\rho} = gh_{LA} + \frac{P_{ur}}{\rho} \tag{6}$$

Solving for V_L:

$$V_L^2 = 2\left[g(h_{LA} + h_{LB}) + \frac{P_{ur} - P_{atm}}{\rho} \right] \tag{7}$$

Similarly, the velocity V_S at the draining point of the high siphon (DPHS) based on the reference elevation of the high siphon (REHS) can be represented as:

$$V_S^2 = 2\left[g(h_{SA} + h_{SB}) + \frac{P_{ur} - P_{atm}}{\rho} \right] \tag{8}$$

where h_{SA} is the distance of liquid surface relative to the REHS inside the MSC, and h_{SB} is the distance between the REHS and DPHS. Therefore, the velocity difference between the DPLS and the DPHS before submerging can be expressed as:

$$V_L^2 - V_S^2 = 2gd \tag{9}$$

where d is the distance between the DPHS and DPLS. Similarly, their velocity difference after submerging can be represented as:

$$V_R^2 - V_S^2 = 2g\Delta d \tag{10}$$

where Δd is the distance between the DPHS and the liquid surface inside IMR.

In order to activate the siphoning effect, there must be flow coming from the low siphon first to perfuse IMR (i.e. $V_L > 0$). From Equation (7), the following pressure relationship should be satisfied:

$$P_{ur} + \rho g(h_{LA} + h_{LB}) > P_{atm} \tag{11}$$

It can be easily realized by increasing the length of the low siphon (h_{LB}) through the flexible height adjustment of the clamping platform. With the drop of liquid level inside the MSC, its inside

pressure P'_{ur} will decrease accordingly. According to equation 8, when the liquid level inside the MSC drops to h'_{SA} relative to the REHS, it satisfies the following pressure relationship:

$$P'_{\mathrm{ur}} + \rho g(h'_{SA} + h_{SB}) = P_{atm} \tag{12}$$

At this moment, the velocity V_S at DPHS will become zero, as shown in Figure 4.2 (b). However, there still will be flow coming from the low siphon at the velocity of $V_R = \sqrt{2g\Delta d}$ to raise the liquid level inside the IMR continuously as long as the height difference Δd exists.

As the liquid level inside the MSC drops gradually, the inside pressure P'_{ur} will decrease continuously. Under the effect of atmospheric pressure, air will be pushed into the high siphon from its draining point to induce cavitation. Simultaneously, air bubbles will appear within the MSC, which can increase the inside pressure P''_{ur} accordingly (Figure 4.2(c)). As a result, the liquid level inside the IMR will rise continuously until it is flush with the DPHS to block the air supplementation (Figure 4.2(d)). Thus, the DPHS will determine the height of liquid level inside the IMR, which can be flexibly adjusted by changing its position. With the slow medium perfusion into the microfluidic channel through the inlet port, the liquid level inside the IMR will decrease accordingly. Once it is below the DPHS, air will be pushed into MSC again to re-adjust the liquid level height to the DPHS (Figure 4.2 (e)). The whole process repeats itself autonomously (Figure 4.2(f)), and finally realizes the siphon-based autofill function.

To better understand this principle, the siphon-based autofill function can be simulated into a simplified electric circuit model. For the air supplementation into the MSC during the cavitation process from the high siphon, it can be analogous to the capacitor charging process, as shown in Figure 4.3 (a). Since the air volume inside the MSC is always changing, it can be treated as a variable capacitor $C(P''_{ur})$. The switch represents whether there is air supplementation into the MSC, which is determined by the distance between the liquid level inside the IMR and the DPHS.

Once this distance becomes zero, it corresponds to the switch-off. The negative pressure P'_{ur} inside MSC can be treated as the reference voltage $V(P'_{ur})$ at the time when the first cavitation process initiates, and the atmospheric pressure at the DPHS is considered as the DC voltage source $V(atm)$. After power consumption by the resistance of $R(h_{SB})$ along the high siphon and $R(h'_{SA})$ through the medium inside the IMR, if the applied voltage is still higher than $V(P'_{ur})$, $C(P''_{ur})$ will be charged which corresponds to the generation of air bubbles inside the MSC. For the IMR during the auto-filling process with liquid through the low siphon, since the liquid level inside the MSC and IMR almost has no change during the adjacent refilling processes, it can be treated as the reference voltage $V(h''_{LA}+h'_{LM})$, as shown in Figure 4.3 (b). As the variable capacitor $C(P''_{ur})$ charges, once the total amount of applied voltage is higher than the voltage of $V(atm)$ that represents the atmospheric pressure positioned at the liquid level inside the IMR, the fixed capacitor $C(IMR)$ will be charged continuously until the switch during the cavitation process is off. Due to the fixed electrical potential difference between the input voltage $V(IMR)$ of the fixed capacitor $C(IMR)$ and output voltage $V(OMR)$, the current passing through the resistance of microfluidic channel $R_{channel}$ is constant, which corresponds to the steady flow inside the microfluidic channel.

Sensitivity analysis of autofill function

Theoretically, during each autofill process, once the liquid surface inside the IMR is below the DPHS, the autofill function will be activated immediately. However, in the practical applications, when the liquid surface inside the IMR touches the DPHS, a liquid column with certain height h_w will usually appear inside the high siphon due to either the capillary effect of the high siphon or pressure fluctuation inside MSC (Figure 4.4(a)). In this case, even though the liquid

surface inside the IMR drops to the level below the DPHS, there is still no air bubble appeared inside MSC to supplement the pressure, which means the autofill function will be invalid. Therefore, in order to restart the autofill function, the pressure P_{MSC} inside the MSC must be further reduced to withdraw the liquid column from the high siphon, which could only be realized by the drop of liquid level inside the IMR. Suppose when the liquid surface inside the IMR drops to the distance of h'_{LW} relative to the RELS (Figure 4.4(b)), the liquid column can be removed to restart the autofill function again. The pressure change inside the MSC during the reactivation stage can be represented as:

$$\Delta P_{MSC} = P_{MSC} - P'_{MSC} = \rho g(h'_{LW} - h'_{LM}) \tag{13}$$

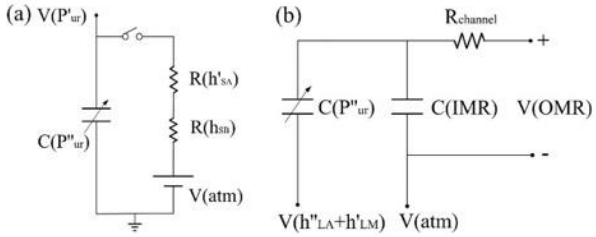

Figure 4.3 Electric-fluidic circuit analogy of siphon-based autofill function
(a) Electric circuit of variable capacitor charging process to simulate the air supplementation inside the MSC during the refilling process. (b) Electric circuit of fixed capacitor charging process to simulate the liquid filling inside the IMR during the auto-filling process.

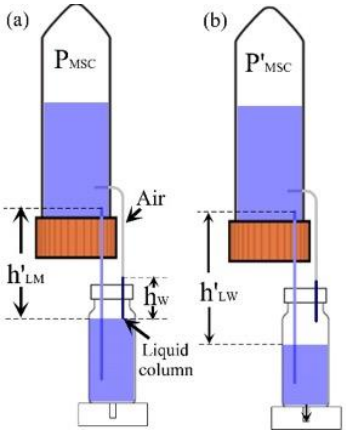

Figure 4.4 Schematic diagram showing the sensitivity analysis of autofill function
(a) Liquid column formation inside the high siphon to block the air supplementation into the MSC. (b) Low sensitivity of liquid level drop inside the IMR through a certain distance to reactivate the autofill function.

This pressure change ΔP_{MSC} should at least offset the extra pressure induced by the liquid column inside the high siphon. Therefore, the following pressure relationship should be satisfied:

$$\rho g(h'_{LW} - h'_{LM}) \geq \rho g h_w \tag{14}$$

This indicates that the liquid surface inside the IMR must drop a distance of at least h_w relative to the DPHS to restart the autofill function. Since medium perfusion into the microfluidic chip through the inlet port is very slow, it will take quite a long time to restart the autofill function with low sensitivity. Therefore, to increase the sensitivity of the autofill function, a liquid column inside the high siphon must be avoided (i.e. $h_w = 0$).

Liquid barrier connector fabrication and operation optimization

In order to completely eliminate the formation of the liquid column inside the high siphon, a homemade liquid barrier connector (LBC) was fabricated and installed at the DPHS, as shown in Figure 4.5 (a). Briefly, a gas permeable/liquid impermeable PTFE film with the pore size of 1μm was hermetically sealed at one side of the connector, and the other side was tightly connected with the high siphon. The fabrication procedure of the LBC was simple, and its assembly process and prototype were shown in a movie clip (Movie S6 from reference[116]). First, two circular disks and the liquid barrier film were separately cut out from a 5mm thick premade PDMS slab and a thin PTFE film by using the puncher with the diameter of 10mm. Then, holes with the diameter of the high siphon and 4mm were separately punched at the center of these two PDMS disks. After their plasma bonding as the housing of LBC, the punched film was glued to this housing by the highly viscous prebaked PDMS without blocking the 4mm opening. Finally, the fully cured connector was inserted into the cap of the IMR, which could be manually moved to adjust the liquid level inside the IMR with high flexibility.

Moreover, to further increase the sensitivity of this enhanced micropump, it is also necessary to prevent liquid column formation inside the high siphon during the initial filling process in which the medium perfusion into the IMR from the low siphon. As shown in Figure 4.5

(b), if the top end of the high siphon is immersed into the liquid inside the MSC, the high siphon should be lifted up to prevent liquid column formation inside it until air bubbles appear inside the MSC. Then, the high siphon can be lowered and interconnected with the movable LBC. Meanwhile, air bubbles inside the MSC would become smaller and faster. Otherwise, the high siphon can be interconnected with LBC directly without inducing the liquid column during both the initial filling and the subsequent refilling process, but no air bubble will appear inside the MSC as the indicator (Figure 4.5(c)).

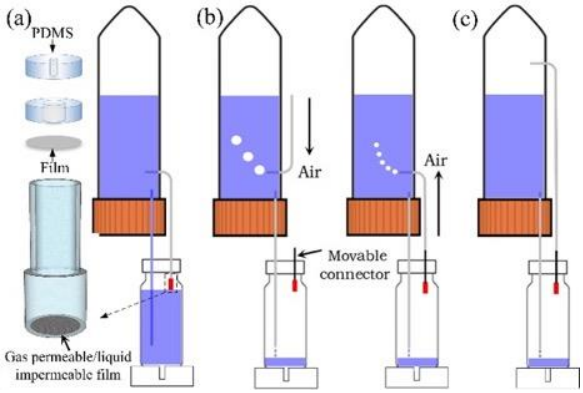

Figure 4.5 Schematic diagram showing the LBC design and operation optimization
(a) Schematic view of the LBC configuration with PDMS and gas permeable/liquid impermeable film, and its integration at the DPHS to prevent liquid column formation during the refilling process. (b) Lift up the high siphon when its top end is immersed into liquid inside MSC to eliminate liquid column formation during the initial filling process. (c) No liquid column formation during initial filling process if the top end of the high siphon is immersed into air inside the MSC.

Finite element simulation of interstitial flow for vasculogenesis

Finite element simulations on interstitial flow for vasculogenesis under the drive of a constant hydrostatic pressure drop were performed by COMSOL Multiphysics 4.3 (Comsol Inc., Burlington, MA, USA). The chip design for the vasculogenesis assay was similar to those described in our previous studies[72, 73]. The interstitial flow across a porous fibrin gel with low permeability of $1.5\times10^{-13}m^2$ inside the tissue chamber was simulated by employing the Brinkman

equation for momentum transportation. Due to the steady hydrostatic pressure drop between the IMR and OMR, the corresponding pressure drop across each tissue chamber was constant to generate the uniform interstitial flow profile, which is the biophysical cue inside the fibrin gel necessary to stimulate vasculogenesis.

Cell culture

Human endothelial colony forming cell-derived ECs (ECFC-ECs) were isolated from cord blood[81], expanded on a flask coated with 10μg/mL fibronectin (Sigma Aldrich) in EGM-2 (Lonza), and used between passages 4- 6. Human normal lung fibroblasts (NHLF) were purchased from Lonza, expanded in DMEM (Corning) containing 10% FBS (Gemini Bio), and used between passages 6- 8. All cell types were grown in a 37°C/5% CO_2/20% O_2 incubator with 100% humidified air environment, and all experimental procedures for embedding cell/tissue into microfluidic device were performed inside a Biosafety Level 2 laminar flow hood with sterile techniques as previously described[71, 72].

Results

Effectiveness of enhanced micropump with autofill function

We first tested the effectiveness of the LBC on the sensitivity of the siphon-based autofill function. As shown in a movie clip (Movie S2 from reference[116]), the sensitivity of autofill function without using the LBC was very low due to the liquid column formation inside the high siphon that postponed the cavitation process. The autofill function could be reactivated only if the liquid column inside the high siphon was removed with the liquid level in the IMR dropping.

However, with the LBC, the autofill function could be activated immediately once the liquid level was below the liquid barrier film sealed on the connector (i.e. predefined liquid level).

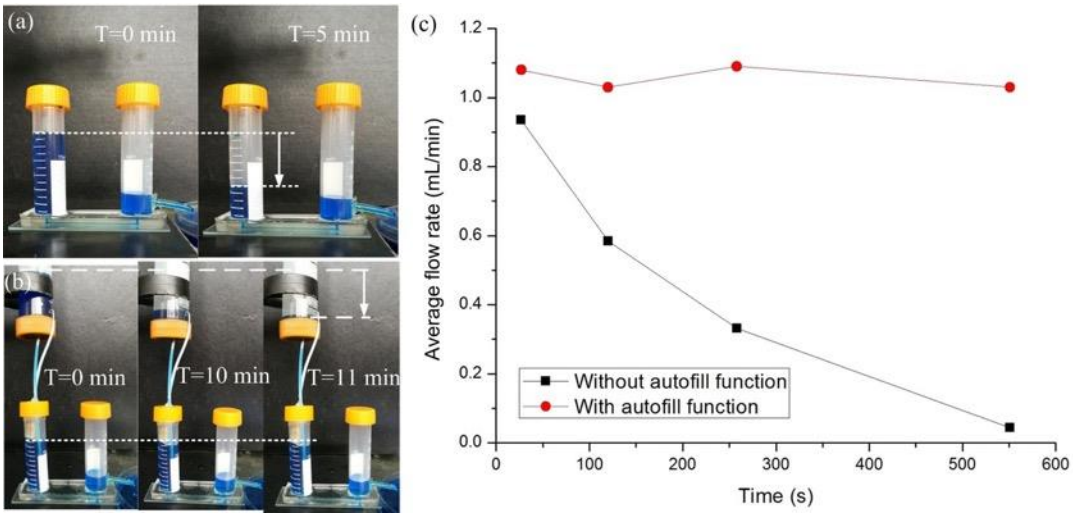

Figure 4.6 Comparison experiment to test the effectiveness of the enhanced micropump with siphon-based autofill function

(a) Decreased hydrostatic pressure drop for conventional micropump without autofill function. (b) Constant hydrostatic pressure drop for enhanced micropump with siphon-based autofill function. (c) Quantitative analysis of flow rate obtained from hydrostatic pressure-driven passive micropump with and without autofill function over time.

In addition, the comparison experiments on the maintenance of hydrostatic pressure drop were conducted based on the micropump with and without autofill function for a microfluidic chip. Here, a long straight microchannel with the length of 45mm and the diameter of 0.7mm was designed in the chip. As shown in Figure 4.6 and a movie clip (Movie S3 from reference[116]), for the conventional hydrostatic pressure-driven passive micropump without autofill function, the liquid level difference between the IMR and OMR dramatically dropped, with a decreased flow rate from 0.935mL/min to 0.0436mL/min over around 9min. However, for the micropump enhanced with autofill function, the liquid level inside the IMR could be steadily maintained at the height of 4cm determined by the LBC (i.e. DPHS). Since the liquid level inside the OMR was set to be 0.5cm, the hydrostatic pressure drop between the IMR and OMR could be steadily maintained

around 3.5cm that resulted in the average flow rate between 1.0mL/min and 1.1mL/min with little fluctuation. It would also persist for a considerable period of time until the liquid level inside the MSC was below the RELS (low siphon level), as shown in Figure 4.6b (T= 11min). In the experiment, the average flow rate was characterized by using the gravimetric method, which was measured with an electric balance (FA1004 from Shanghai Liangping Instrument Co., Ltd. with a resolution of 0.1mg) by weighting the medium accumulated in the outlet medium reservoir driven by the micropump within a defined period of time.

Based on the relative flow rate between the inlet and outlet, there were two different refilling modes, as shown in a movie clip (Movie S4 from reference[116]). If the flow rate in low siphon was higher than the drainage from outlet tubing, the IMR would be refilled intermittently to maintain the constant liquid level determined by the LBC and air bubbles only appeared inside the MSC during the refilling process. Otherwise, the IMR would be refilled continuously and air bubbles appeared all the time. However, in this case, the liquid level inside IMR decreased over time due to the inadequate medium supply and the stable flow rate could not be generated. In both cases, regardless of the different micropump configuration, the autofill function is always effective. However, for microfluidic-based applications, the intermittent refilling mode is normally performed due to the high fluidic resistance of narrow microfluidic channel compared with the diameter of the low siphon. Thus, the constant liquid level can always be well maintained through the autofill function of enhanced micropump to realize the stable flow rate inside microfluidic chip.

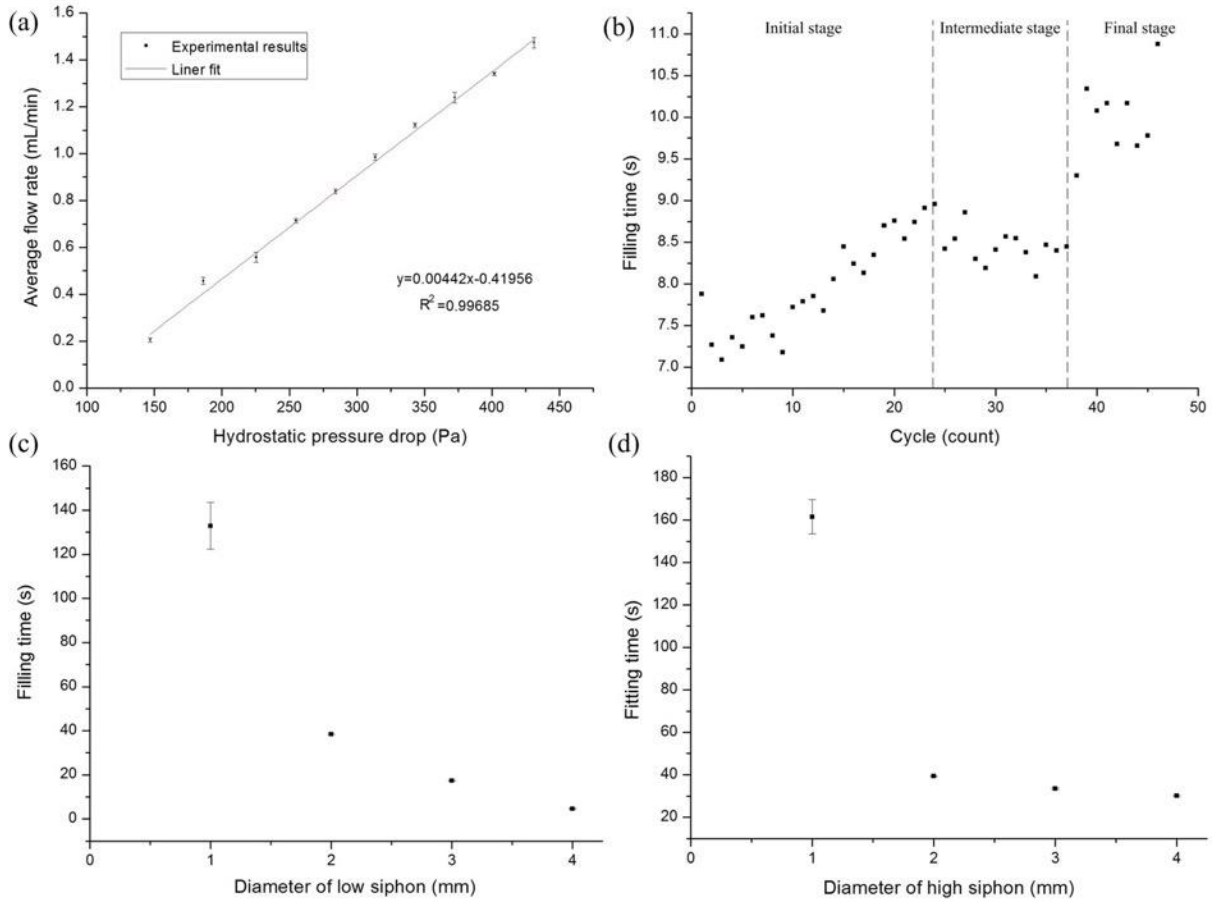

Figure 4.7 Quantitative analysis of the characteristics of enhanced micropump with autofill function
(a) Good linear relationship with small error bar range between hydrostatic pressure drop and flow rate. (b) Refilling time in each cycle slightly increased as the cycle number increased in the same refilling loop. (c) The bigger the diameter of the low siphon, the shorter the refilling time (liquid volume:1 mL). (d) The bigger the diameter of the high siphon, the shorter the refilling time (liquid volume:1 mL).

Characterization of the enhanced micropump

For the hydrostatic pressure-driven passive micropump, the flow rate inside the microfluidic device was dependent on the medium height difference between the IMR and OMR, as well as the dimensions of the microfluidic channels. As shown in Figure 4.7 (a), for the same microfluidic device integrated with the enhanced micropump, the flow rate was linearly proportional to the predefined hydrostatic pressure drop between IMR and OMR, which was determined by the DPHS and the height of drainage tubing at OMR, respectively. The small error

bar range also indicated that the flow rate under certain hydrostatic pressure drop was stable as the result of the siphon-based autofill function.

For one device in the same refilling loop, the refilling time in each circle would slightly increase as the cycle number increased, especially at the initial refilling stage, as shown in Figure 4.7 (b). It is known that when supplementing a certain amount of air, the larger the confined space, the lower the pressure inside it. Similarly, the air volume inside MSC would increase gradually as its liquid level dropped, which resulted in the decreased flow rate at the DPLS to extend the refilling time. Specifically, the air space inside MSC was limited at the initial refilling stage (e.g. 0- 24 cycles). When supplementing the air from high siphon during this stage, the pressure inside MSC would recover rapidly. As a result, the refilling time would increase as the cycle number increased with high sensitivity. When the liquid level inside MSC dropped to a certain height after several cycles (e.g. 25- 37 cycles), the pressure recovery induced by the air supplement was less sensitive than that at the initial refilling stage. Then we observe that there is a plateau during the intermediate refilling stage. When the liquid level almost reached the bottom of MSC after more cycles at the final refilling stage (e.g. >38 cycles), the sensitivity was pretty low that resulted in the great variance in the refilling time.

Besides the air volume inside the MSC, the diameters of both the low siphon and the high siphon would greatly affect the refilling time. As shown in Figure 4.7 (c), the bigger the diameter of the low siphon, the shorter the refilling time. For example, to refill the liquid volume of 1mL, it would take an average of 132s, 38s, 17s and 4.6s for the high siphon with the same diameter of 1mm and the low siphon with different diameter of 1mm, 2mm, 3mm and 4mm, respectively. It was because the bigger the diameter of the low siphon, the higher the liquid flow rate inside it. In addition, the faster the drop of liquid level inside the MSC, the higher the speed of bubbles coming

from the high siphon. Similarly, for the low siphon with the same diameter, it would take a shorter refilling time for the high siphon with a larger diameter. As shown in Figure 4.7 (d), to refill the liquid volume of 1mL, it would take an average of 161s, 39s, 33s and 30s for the low siphon with the same diameter of 1mm and the high siphon with different diameter of 1mm, 2mm, 3mm and 4mm, respectively. In contrast to the influence of the low siphon on bubble speed, the bigger the diameter of the high siphon, the slower the speed of bubbles coming from the high siphon. However, the bubble size would be much bigger for the high siphon with a larger diameter. Although different diameter of both high siphon and low siphon had large effect on the refilling time, the influence sensitivity of low siphon would be much larger than that of high siphon.

Parallel and multiplexed micropump with high flexibility

By interconnecting multiple IMRs with tubing or other components (e.g. luer connectors, etc.), two or more parallel experiments for statistical analysis with the same flow conditions can be simultaneously conducted by using only one MSC (Figure S2 in reference[116]). Through the connected vessels effect, the liquid volume inside multiple IMRs will be maintained at the same height level that is determined by the DPHS inside only one IMR.

Furthermore, the respective high siphon from two different MSCs could be interconnected into one common high siphon through a four-way stopcock with four different operation modes, which could be flexibly switched during either the same or different refilling loop under the same hydrostatic pressure drop (Figure 4.8 and Movie S5 from reference[116]). For the MSCs with the same liquid, after the liquid volume inside one MSC was almost empty, the other MSC could be switched on to prolong the perfusion time, which would be suitable for long-term experiments without the need to frequently refill medium in the MSC. In addition, different solutions could be

selectively loaded into the IMR to the predefined liquid level, which would be beneficial for versatile applications like the response of cultured cell/tissue to different chemical reagents or drug compounds. For example, after the formation of vascularized microtumors under the continuous cell culture medium perfusion coming from one MSC, drugs inside the other MSC could be switched on and added into the cultured tissue for anti-cancer drug screening applications[55].

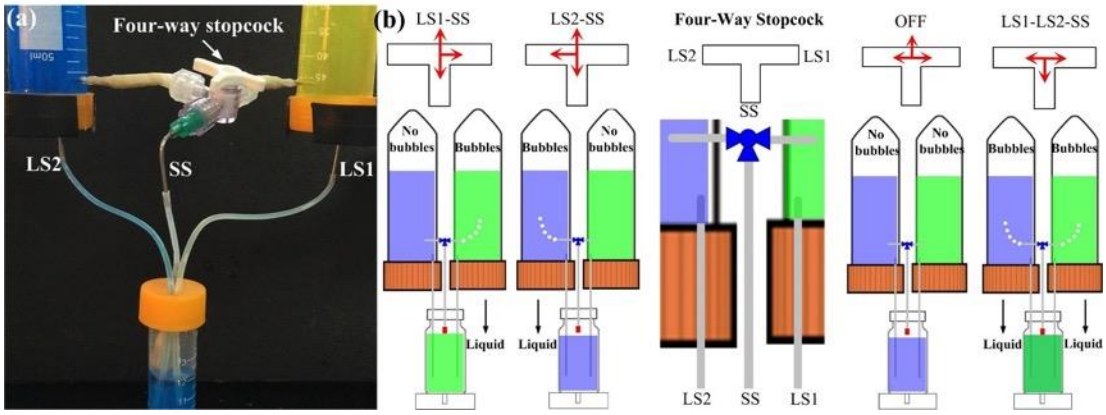

Figure 4.8 Multiplexed micropump with the integration of four-way stopcock for selective liquid perfusion into the IMR at the predefined liquid level

(a) Prototype of the multiplexed micropump. (b) Four operation modes controlled by the switch of four-way stopcock with high flexibility

Vasculogenesis by interstitial flow with the enhanced micropump

For ease of transport and use, both the size (13×5×6 cm_3) and the weight (60g) of the single disassembled system is small, and its assembly procedure is very simple, as shown in a movie clip (Movie S6 from reference[116]). All of the components can be easily acquired. Figure 4.9 (a) shows a prototype of the enhanced micropump with two parallel single assembled systems for in vitro vasculogenesis studies. Notably, the configuration of enhanced micropump may vary based on different microfluidic chips for specific biological applications. Here, two MSCs are placed on the ring stand above the IMRs that are fixed at the inlet ports of the microfluidic chip. Briefly, the bottom of the IMRs are immersed into the uncured PDMS and then placed on the inlet ports, which

will form the solid connection after cured. The thread-to-barb fittings are utilized to establish the interconnection between the MSC and siphon, which can also be sealed with uncured PDMS. The bent stainless-steel needles of predetermined height are inserted into the outlet ports, and the culture medium flowing from the outlets of the microfluidic chip is guided into an empty cell culture flask, which acts as a waste container. For microfluidic chip, three central millimeter-sized diamond tissue chambers (1×2mm) with one gel loading inlet and outlet are connected with two side square cross-sectional microfluidic channels (100×100μm). The microfluidic channels are further coupled in an asymmetrical design with one medium inlet and outlet, which can generate the interstitial flow across the confined gel inside tissue chamber[55].

In the experiment, the hydrostatic pressure drop was steadily maintained at 10mmH_2O, and interstitial flow inside the tissue chamber was generated at a velocity of 0.31- 2.55μm/s in the horizontal direction and 2.44- 19.4μm/s in the vertical direction based on the simulation results, as shown in Figure 4.9 (b). Under the stimulus of interstitial flow generated by the constant hydrostatic pressure drop, vascular fragments could be formed as early as day 3 and continued to develop into a capillary network through day 5 as previously described[55, 71, 72]. By day 7, the capillary network was lumenized and interconnected, and this could last for more than 14 days (Figure 4.9 (c) and Movie S7 from reference[116]). Most importantly, besides the advantage of steady flow, the enhanced micropump also enabled long-term perfusion inside the incubator for up to 5 days without the need to supplement medium to the MSC or relevel the hydrostatic pressure drop between the IMR and OMR. This is 2 to 3-fold longer than our previous culture method, which needs medium change every other day[71].

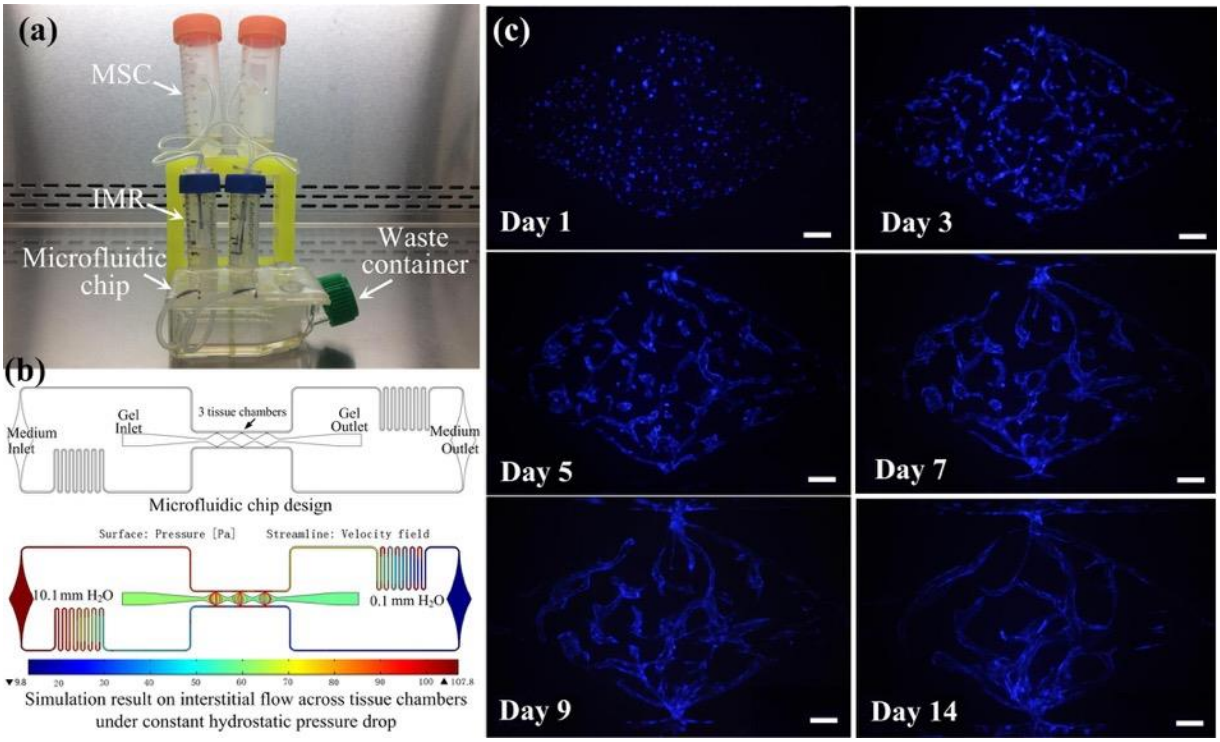

Figure 4.9 Application of the enhanced micropump system for sustaining an in vitro vasculogenesis model (*a) Prototype of system setup for tissue culture inside incubator. (b) Microfluidic chip design and simulation on the interstitial flow profile across tissue chamber for vasculogenesis. (c) Microvascular network formation inside tissue chambers throughout 14 days. Scale bar: 100µm.*

Discussion

Compared with the traditional hydrostatic pressure-driven passive micropump, our enhanced micropump can provide a steady flow rate inside microfluidic devices for long periods without the need of additional complicated peripheral equipment. All the components can be easily acquired from most laboratories and replaced with high flexibility. For example, the supporting/clamping platform can be customized to hold multiple MSCs and fabricated by 3D printing technology. It also can be designed into adjustable platforms, whose height can be flexibly moved up and down to adapt multiple settings. There is no doubt that the LBC is the core component of the whole system, which will directly determine the success of autofill function and its sensitivity. To make it more reliable, the standardization of the LBC should be further improved by using standard fittings like hollow screw and nut. Furthermore, the enhanced micropump can

be applied to the liquid with different hydrophilic/hydrophobic properties. If the liquid inside the IMR is hydrophilic, the PTFE films on LBC with the hydrophobic property should be utilized. Otherwise, the hydrophilic PTFE films need to be selected.

Here we have focused on a single medium reservoir module with siphon-based autofill function to maintain the high hydrostatic pressure. A further increase in the number of modules is possible for some applications that require different hydrostatic pressure drops with either the same or different liquid simultaneously. For example, for multi-organ-chip or body-on-chip applications, each organ has its own culture condition, which would communicate with each other by secreting and sensing a variety of biomolecules or metabolite. Therefore, multiple modules with either different medium types or different hydrostatic pressure drops can be placed on a single microfluidic chip to maintain the optimal condition for each organ as well as to study the organ-to-organ communications (as shown in Figure S3 from reference[116]).

While this enhanced micropump has many advantages, there are still some limitations. For example, although it can maintain the constant hydrostatic pressure drop to supply the steady flow rate, pulsatile flow conditions cannot be implemented directly. To solve this problem, the combination of microfluidic oscillator arrays with the enhanced micropump as the common gravity head can generate the pulsatile flow autonomously with a wide range of oscillation periods[117]. Another drawback of this micropump is that it can only provide low-pressure input to the microfluidic chips, which is only the limited hydrostatic pressure drop between the IMR and OMR. Although it's very suitable for tissue culture and other biomedical researches, it cannot be used for applications needing high pressure or flow rate, such as droplet generation.

CHAPTER 5: NON-UNIFORM VASCULAR NETWORKS GENERATED BY NON-UNIFORM FLOW VELOCITY DISTRIBUTION FOR AN ON-CHIP HEREDITARY HEMORRHAGIC TELANGIECTASIA MODEL

Background

Hereditary Hemorrhagic Telangiectasia (HHT) is a dominant genetic disorder characterized by the presence of vascular malformations in multiple organs. The rupture of these vascular malformations will lead to acute hemorrhage and chronic bleeding, as well as stroke and heart failure[118-120]. Although the HHT is considered as a rare disease with worldwide prevalence in the order of 1 in 10,000[121], it still affects significant number of people. 85% of HHT cases are associated with heterozygous mutations in two genes: activin receptor-like kinase1 (ACVRL1 or Alk1; type 2 HHT) or its coreceptor, Endoglin (ENG; type I HHT)[122]. High shear stress also affects ECs and can mediate HHT[123-125]. The current research methods for HHT are mainly mouse or zebrafish model[126, 127], and computational simulation tools are used to study the effect of flow on the vasculature[128]. Recent research shows that a loss of Alk1 expression in the mouse retina produces arteriovenous malformations in regions that correlate with high blood flow and shear stress[123]. However, the usage of animal model faces various issues such as high cost and ethical dilemma. Microfluidics technology provides methods to overcome these drawbacks. In other words, microfluidics technology generates HHT models with human cells, which, as a result, could provide a more biologically relevant model. The microenvironment can be better controlled to study the effect of the shear stress on vasculature. In this chapter, we present a microfluidic chip to assess the effect of a range of shear stresses on vascular network formation by altering the angle

of medium channels. Vasculatures are cultured in this device and modeled to computational simulation for the shear stress calculation.

Materials & Methods

Microfluidics chip design

The microfluidic chip prototype is comprised of a tissue chamber and medium channels (Figure 5.1 (A)). The tissue chamber contains a 3D matrix embedded with endothelial cells that will organize under interstitial flow into a lumenized vascular network. The adjacent medium channels supply medium through communication pores to generate interstitial flow for the vasculature development. Compared to a control device with parallel medium channels, the slanted medium channels in the current design form an angle α and make a sector shape for the tissue chamber (Figure 5.1 (A) & (B)). By adjusting this angle α, as well as the pressure input at the medium inlets, we can generate a non-uniform flow velocity profile, and thus manipulate shear stress during and after the vasculogenesis. To keep the tissue chamber areas equal, the width at the middle of the chamber is kept as the same width with that of the control device (~2mm). Bottomless screw cap vials, as reservoirs to adjust hydrostatic pressure, are glued to the medium inlets by PDMS (Figure 5.1 (C)). The 4-inlet setting of pressure input make it flexible to adjust the flow profile in the tissue chamber.

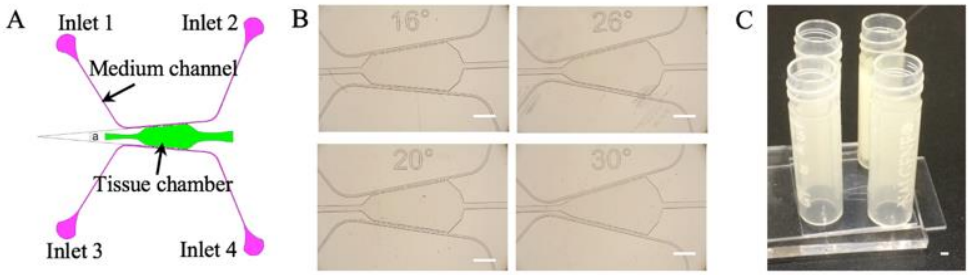

Figure 5.1 Microfluidics chip prototype for HHT model
(A) Schematic of slanted channel microfluidics chip design. (B) Various designs of different angel α. (C) Assembled device with screw cap vials. All the scale bars are 1mm.

Finite element simulation

COMSOL Multiphysics® 5.2a (COMSOL Inc.) is used to simulate the interstitial flow through ECM and the laminar flow inside a developed microvascular network. The details of the methods have been described in CHAPTER 2.

Cell culture

HUVECs and NHLFs are used for the experiments. The cell expanding method is also as the same in CHAPTER 2. HUVECs and NHLFs are embedded at a 1:1 ratio ($7\times10_6$cells/ml of each cell type) in fibrin gel in the tissue chamber of the slanted channel device. A device with parallel medium channels ($\alpha=0$) is used as a control. Both devices are cultured at 37°C and 5% CO_2. The initial pressure setting is shown in Figure 5.2 (A). The pressure settings between inlets 1&3, as well as 2&4, are flipped every other day to assist the vasculogenesis process. Vessel length per unit area is measured by AngioTool (National Institute of Health) as an indicator of the density of the vascular network.

Result and discussion

Non-uniform flow velocity distribution in the slanted channel design

The finite element simulation result of the interstitial flow in the control device shows a bell-shape curve in the center of the tissue chamber, but the flow velocity in the slanted channel device ($\alpha = 30^{o}$ shown as an example) shows that the peak velocity is shifted to the narrow part of the tissue chamber (Figure 5.2 (B)). This is due to the angle α generates different widths for the tissue chamber, and the narrow part experiences smaller hydraulic resistance, thus with higher flow velocity. By analyzing the velocities at different positions of both the control and slanted channel devices, we observe a clear velocity difference at the left and the center part from the right part in slanted channel device, while the velocity in the control device shows a more uniform distribution (Figure 5.2 (C)). This indicates a non-uniform flow velocity profile can be generated in our chip design to provide the desired shear stress to induce HHT symptoms.

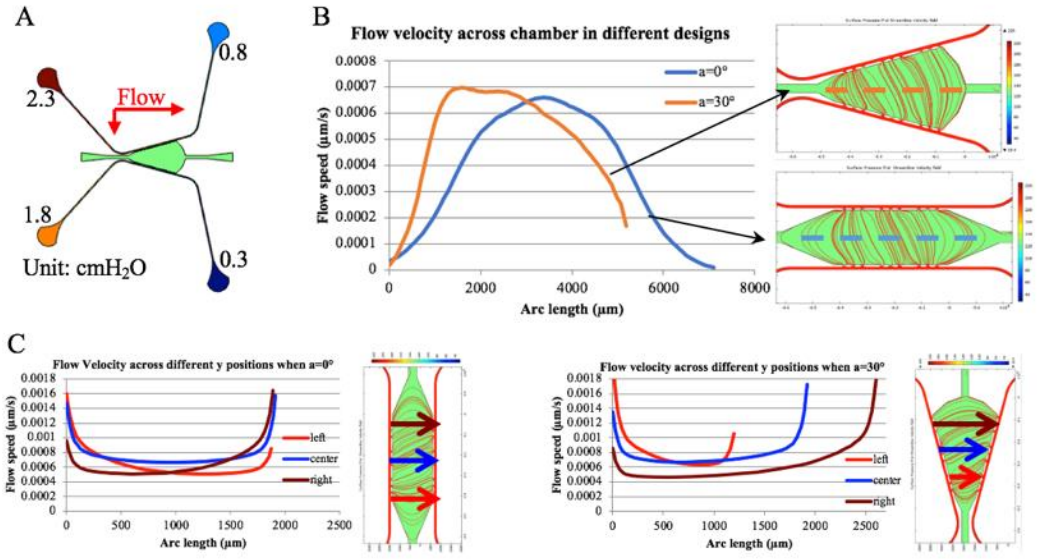

Figure 5.2 Non-uniform velocity profile in the slanted channel design
(A) Hydrostatic pressure input settings to the design and the pressure gradient. (B) Flow velocities at the horizontal cutting lines across the middle of tissue chambers. The peak of the velocity in the α= 30° device is shifted to left compared with control device (α= 0). (C) Velocity profiles at different vertical cutting lines. The α= 30° device has higher velocity in the left and middle regions than that of the right region.

Vasculature formed in various designs of slanted channel device

Based on the reported result[123] and our device design, the hypothesis is that the narrow part of the tissue chamber will have capillaries with relatively larger diameters and the wide part of the tissue chamber will have capillaries with relatively higher density. We observe vasculature formed around day 6 of the culture in chips with different angle α (16º, 20º, 26º and 30º) (Figure 5.3). The HUVECs also migrate out to the medium channels to form good anastomosis. The vessel length per unit area is analyzed as an indicator for the vessel density. For ease of analysis, the tissue chamber is divided into three regions: left (the narrow part), middle, and right (the wide part). The vessel length per unit area shows an increasing trend from the left to the right of the tissue chamber in the 20º and 30º design, but the control device shows a uniform density of the capillary network (Figure 5.4).

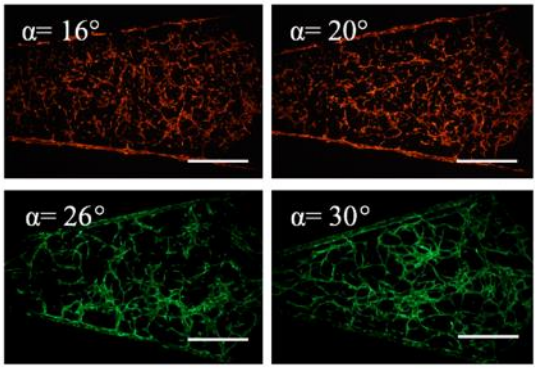

Figure 5.3 Vasculature formed in chips with different angle α

All scale bars are 1mm. HUVECs are labeled with mCherry or Venus-GFP.

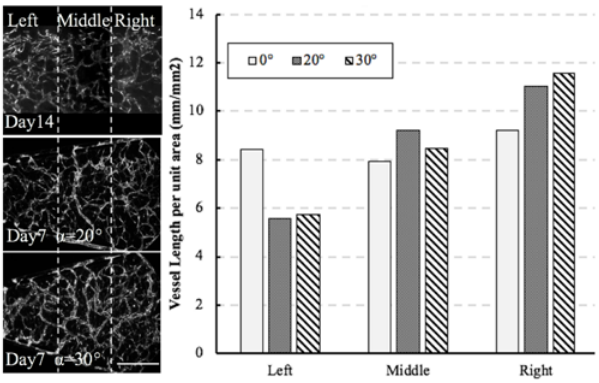

Figure 5.4 Vessel densities in different regions of the tissue chamber

The vessel length per unit area is used to indicate the vessel density. In the control device, it doesn't show significant difference in different regions. However, in the 20° and 30° device, this number shows an increasing trend from the left to the right region. The scale bar is 1mm.

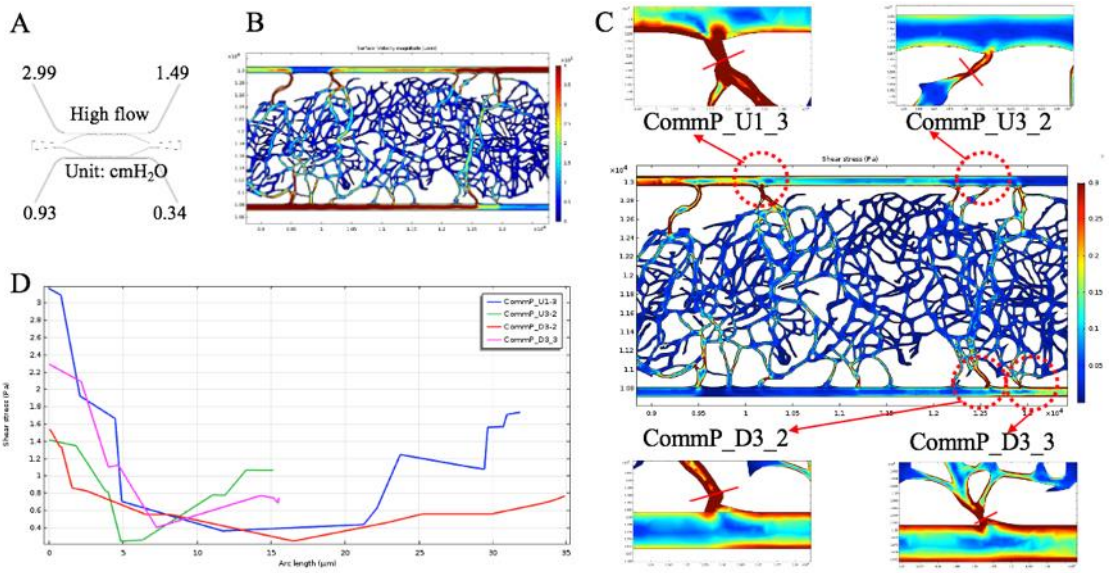

Figure 5.5 High shear stress distribution in the capillary network

(*A) The high flow setting for the medium inlets. (B) Velocity gradient in vasculature. (C) Shear stress gradient in vasculature. Communication pore (labeled as CommP) regions are showed in high magnitude view for the high shear stress. (D) Plot of the shear stress from the cutting lines of communication pores in (C).*

High shear stress distribution in the capillary network

In order to generate the highest flow rate in the device, a high flow mode (Figure 5.5 (A)) is applied to the medium inlets. The velocity and shear stress are plotted by COMSOL. We observe that the high flow velocity regions are similar to the high shear stress regions, or the

communication pore regions (Figure 5.5 (C)). We further plot the shear stress at the cross session of the high shear region, and the highest shear stress is located at the vessel wall, where, according to the finite element simulation results, the shear stress can be about 1.4- 3.2Pa (Figure 5.5 (D)). Although the simulation model has a lot of approximations during the modeling process, it still shows the trend of the shear stress distribution, given the fact that we cannot directly measure the flow in the vasculature.

Future perspective

The designing purpose of the HHT model is for large scale drug screening studies. However, the current prototyping takes extra manpower in fabrication and operation; for example, the gluing process of medium reservoirs and removing and adding caps for the reservoirs take a long time, and a prototype chip takes very large space in the incubator. The solution for these problems is to build a high throughput platform integrated with well plate, so that the fabrication and cell culture process is simplified, and more miniaturized devices can be applied. It is also easy to apply commonly used imaging system for data acquisition. However, the 4-inlet design of prototype increases the difficulty of integrating to 96 well plate by increased inlet numbers. Therefore, we redesign a high throughput system that includes 12 units of the HHT chip design (Figure 5.6 (A)). The pressure regulator design is also integrated to the chip to assist the cell/ECM loading process to guarantee success rate of large-scale screening experiment. Customized 3D printed well inserts (Figure 5.6 (B)) are also developed to increase the flexibility of adjusting the hydrostatic pressure input to the tissue. After the concept is proven, the high throughput form for other angles (16º, 20º, 26º and 30º) can also be built. Another aspect to improve is the ECs used for the model. Although the HHT is a hereditary disorder as previously described, the ECs we

currently use for the model are wild type ones; thus, by integrating Alk1 knock-out ECs, the model can be fully functional to study the effect of high shear stress on HHT. Tissue specific HHT will be built with special properties. For example, vascularized liver/HHT model, is discussed in the next chapter with the add-on of oxygen tension control module.

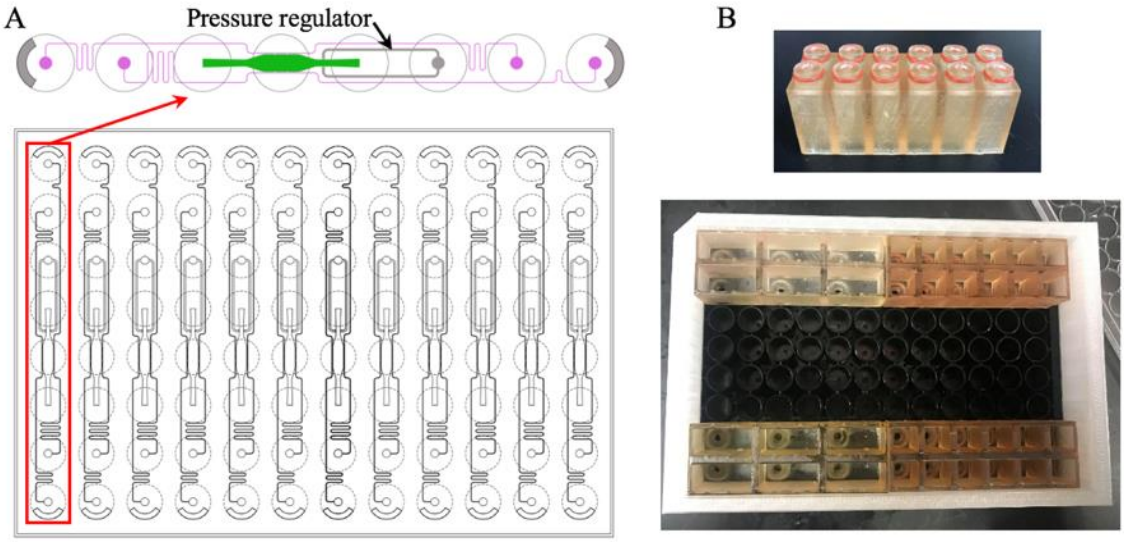

Figure 5.6 High throughput design for HHT model
(A) unit chip design and 12-unit layout fitted for 96 well plate. (B) 3D printed well inserts and assembly to well plate.

CHAPTER 6: LOW OXYGEN TENSION GENERATED BY MICROFLUIDICS CONTROL FOR ON CHIP 3D VASCULATURE

Background

Oxygen tension, or partial pressure of oxygen, affects cellular function and behavior in living tissue. Oxygen plays a very important role in energy metabolism and regulatory activity in cells; 95% of the oxygen in our body, functioning as primary electron acceptor, is used in a process called mitochondrial oxidative phosphorylation, and this process can provide 95% of the adenosine triphosphate (ATP) in our body[129]. Oxygen tension is also an important factor in signaling pathway affecting the differentiation of stem cell[130]. Hypoxia can maintain the undifferentiated state of stem cells[130] and the high expression of hypoxia-inducible factor (HIF1-α)[131], which plays a role in angiogenesis[132] that affects the formation of capillary network. The oxygen tension in healthy tissues varies from different tissue types[133-135], but the typical oxygen tension is between 2-9%[130], which is lower than the ambient atmospheric oxygen tension (21%). Since the normal incubator for cell culture is set at 37°C in 5% CO_2 and connected to the ambient atmosphere, how to regulate the oxygen tension in vitro is a critical matter to mimic the physiological microenvironment where cells live in vivo.

Current methods for oxygen tension control can be classified into two categories: global macroscale control and local microenvironment control[136]. The global oxygen control of macroenvironment includes hypoxic chambers, hypoxic workstations, and perfusion chambers. These methods only provide a single oxygen tension level at a time, so they cannot replicate the in vivo oxygen gradient inside the tissues. Bulky and expensive equipment, slow equilibration, and difficulty in coupling to microscopy also limit their usage. On the other hand, the local control of the oxygen in the microenvironment using microfluidic system may overcome these drawbacks.

Different strategies have been utilized to control the oxygen tension in these microfluidic systems. The first is using equilibrated liquid[137] or gas[138-146] as a source to control the system's oxygen tension. Liquid equilibrated by gas, or gas itself, are perfused to the tissue to balance the oxygen tension delivered to the tissue. The second is the depletion of oxygen by cellular consumption[147, 148]. This method takes the advantage of oxygen consumed by large number of cells, especially cancer cells, to generate an oxygen gradient as cell culture medium pass the cell culture region. The third is using chemical reaction to generate or scavenge oxygen on-chip[149-153]. These chemical reactions are usually happened in a separated microfluidic channel to avoid toxic chemicals affecting cells or tissues. Oxygen gradient can be generated by adjust the concentration and flow rate of chemicals, as well as the distance between the microfluidic channels and the tissue culture region.

The methods of oxygen tension measurement are generally in two categories: Clark-style electrodes and luminescent optical sensors. Clark-style electrodes are based on the reduction of oxygen at the working electrode[154]. Oomen, et al.[155] summarize the structure and working mechanism of Clark-style electrodes in detail. Due to the relatively large size of the electrodes and the depletion of oxygen, luminescent optical sensors are developed for monitoring oxygen levels inside microfluidic systems. These optical sensors can reversibly be quenched by oxygen and change their fluorescence intensity and excited lifetime. The relation between fluorescence intensity and oxygen tension is described by the Stern-Volmer equation[150]:

$$\frac{I_0}{I} = 1 + K_q[O_2] \tag{15}$$

where I_0 is the intensity in the absence of oxygen, I is the intensity in the presence of oxygen, K_q is quenching constant, and $[O_2]$ is the oxygen tension. The quenching constant, K_q, needs to be calibrated for each sensor by measuring the intensity of at least two known oxygen tensions, and

a larger K_q value means a higher sensitivity for the system. With oxygen indicating fluorophores, a normal fluorescent microscope is sufficient to measure the oxygen tension. The commonly used oxygen indicating fluorophores are ruthenium tris(2,2-dipyridyl) dichloride hexahydrate (RTDP) and platinum (II) octaethylporphyrin ketone (PtOEPK). RTDP suspension can be simply flowed through the microfluidic device channels to measure the oxygen tension of the entire microfluidic network, but RTDP is lightly toxic to cells[156]. PtOEPK, on the other hand, can be incorporated into the channel walls to implement long-term monitoring of the oxygen tension and avoid toxicity[147, 157].

Therefore, the oxygen tension is an essential element to generate a more biologically relevant vasculature-on-chip model. In this chapter, a test microfluidics device to integrate oxygen tension control module to our current vasculature-on-a-chip platform is presented. Then, a vascularized liver model with oxygen gradient is proposed and tested. Luminescent optical sensor RTDP and PtOEP are fabricated for the vasculature-on-a-chip design.

Material and method

Microfluidic chip design for oxygen tension control

A test chip is first designed to validate the concept of oxygen tension control and cell viability during long term culture with scavenger. This chip design has three basic elements: a tissue culture module, scavenger solution channel, and a thin layer of PDMS to separate them (Figure 6.1(A)). The tissue culture module in the top layer contains a series of tissue chambers for single tissue type and the supporting medium channels. The serpentine channel in the bottom layer is for oxygen scavenger solution to flow and consume the oxygen in the device; sodium sulfite (Na_2SO_3) is used as the scavenger, and its concentration and flow rate can be adjusted to alter the

oxygen tension. A 100μm thick PDMS layer is used between them to separate the scavenger solution and the vascularized tissue. This thin layer of PDMS is fabricated by spin coating uncured PDMS on a silicon wafer and bake in a 120℃ oven for 30mins. The high permeability and the small thickness of PDMS layer will allow oxygen to permeate through quickly from top to bottom layer for the scavenging reaction. The multilayer PDMS alignment and bonding is assisted by the 3D aligner we built (Appendix B). Isolating the oxygen from atmosphere is important in this design, so the bottom layer will be bonded to a glass slide to make it gas impermeable. And there is a layer of polyvinylidene chloride (PVDC) above the top layer tissue culture module as a barrier[158]; the PVDC membrane is assembled to the PDMS by plasma bonding. Then, the screw cap vials are glued to the top the chip as the medium reservoirs (Figure 6.1 (B)). The whole device is safe to be autoclaved to sterilize before usage.

Another chip design is a new design for vascularized liver model and liver specific HHT model (Figure 6.3 (A)). In this design, scavenger channel is integrated in the same layer with tissue culture module. The medium channels are designed to mimic the blood vessels distribution of liver tissue. Three groups of communication pores are connected to the medium channels mimicking hepatic artery, portal vein, and central vein. The scavenger channels are designed next to the tissue chamber to generate oxygen gradient mimicking the in vivo microenvironment.

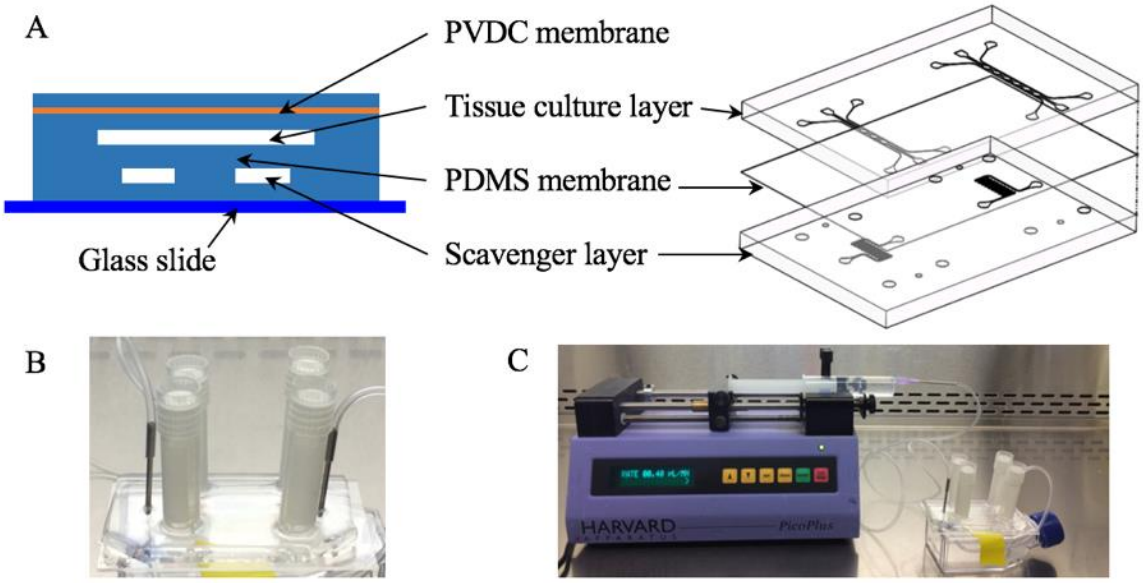

Figure 6.1 Microfluidic chip design for oxygen tension control
(A) Test chip design with multilayer setting for oxygen tension control. The PDMS membrane thickness is 100μm, allowing fast oxygen permeation. PVDC membrane and glass slide will isolate atmospheric oxygen. (B) Fully assembled chip with oxygen tension control module. The screw cap vials are for the hydrostatic pressure input from medium, and the plastic tubings are for scavenger perfusion. (C) Syringe pump used for scavenger perfusion. A T-25 cell culture flask is modified as the sink for scavenger.

Finite element simulation

COMSOL Multiphysics® 5.2a (COMSOL Inc.) is used to simulate the oxygen transportation across the PDMS and tissue chamber. Transport of diluted species model is applied to the liver chip design. The diffusion coefficient of oxygen in water is set as $2.1\times10^{-9}m^2/s$ and that in PDMS is set as $3.55\times10^{-9}m^2/s$[153].

Cell culture

The ECFC-EC and NHLF are used to test the cell viability in the test chips during the long-term culture. The cell expanding process and loading process has been described in the previous chapters. A group of chips without the PVDC membrane is set as control group with normal oxygen tension. Before day 9, the scavenger channels in experimental groups are filled with PBS to keep the humidity and osmotic pressure in the tissue chambers. At the end of day 9, three

conditions are applied to the tissue: (1) normal oxygen condition (control chips), (2) lower oxygen condition (chips with PVDC membrane, scavenger channel filled with PBS), (3) minimum oxygen condition (chips with PVDC membrane, scavenger channel perfused with sodium sulfite solution, 2mg/ml at 0.4µl/min delivered by syringe pump) (Figure 6.1 (C)). The hydrostatic pressure in the medium reservoirs are reset and media are refreshed every other day. The waste scavenger is collected by a customized sink to avoid contaminating the incubator (Figure 6.1 (C)).

Calibration of Stern-Volmer equation

RTDP is used as the oxygen indicating fluorophores for the calibration of Stern-Volmer equation (Equation (15)). A 2mg/ml RTDP is made within the 10mg/ml fibrin gel. This mixture is loaded to the tissue chamber for measurement. The fluorescence intensity I is calculated by ImageJ (National Institute of Health). Since $\frac{1}{I}$ is linearly related to $[O_2]$, a calibration needs to be performed to calculate the quenching constant K_q; at least two known points are required to do the calibration. Then the equation can be used to calculate oxygen tension when the fluorescent intensity is measured at certain point. Sodium sulfite solution (0% oxygen, 10mg/ml) and PBS (20% oxygen) are used as the known points. Then linear regression is performed to calculate the quenching constant K_q.

Fabrication of thin film oxygen sensor

PtOEP (platinum octaethylporphyrin) is used as the luminescent optical sensor. PtOEP has similar property as PtOEPK and can be immobilized in polystyrene (PS) film. The powder of PtOEP is first dissolved in toluene at 1.5mg/ml and filtered to remove the undissolved debris. PS beads is also dissolved in toluene to make a 35% (w/w) solution. Then these two solutions are

mixed with a 1:2 (v/v) ratio. The fully mixed solution is then spin coated (1000rpm for 1min) on a 75×50mm glass slide, then air dried in dark overnight to allow complete evaporation of toluene. To assist the sensor layer protection and the cell adhesion during the experiment, a very thin layer of PDMS is then spin coated (3000rpm for 1min) on the top surface, which also allows plasma bonding to assemble to other parts of the chip.

Results and discussion

Angiogenesis induced by low oxygen tension during long-term culture

The primary vascular networks are formed in all the tested chips by day 9 (Figure 6.2 (A)). At this point, the control chip had more mature vascular networks and the PVDC embedded device only had fragments of vessels. After the scavenger was perfused into the scavenger channel of the chip at day 9, the vascular network in the minimum oxygen tension continued to develop by angiogenesis, whereas the vasculature in normal and lower oxygen control didn't show obvious change from day 9 to day 14 (Figure 6.2(A)). Thus, a low oxygen level slows the growth of vasculature; however, once the hypoxic levels are reached in the presence of Na_2SO_3, angiogenesis is stimulated in the device.

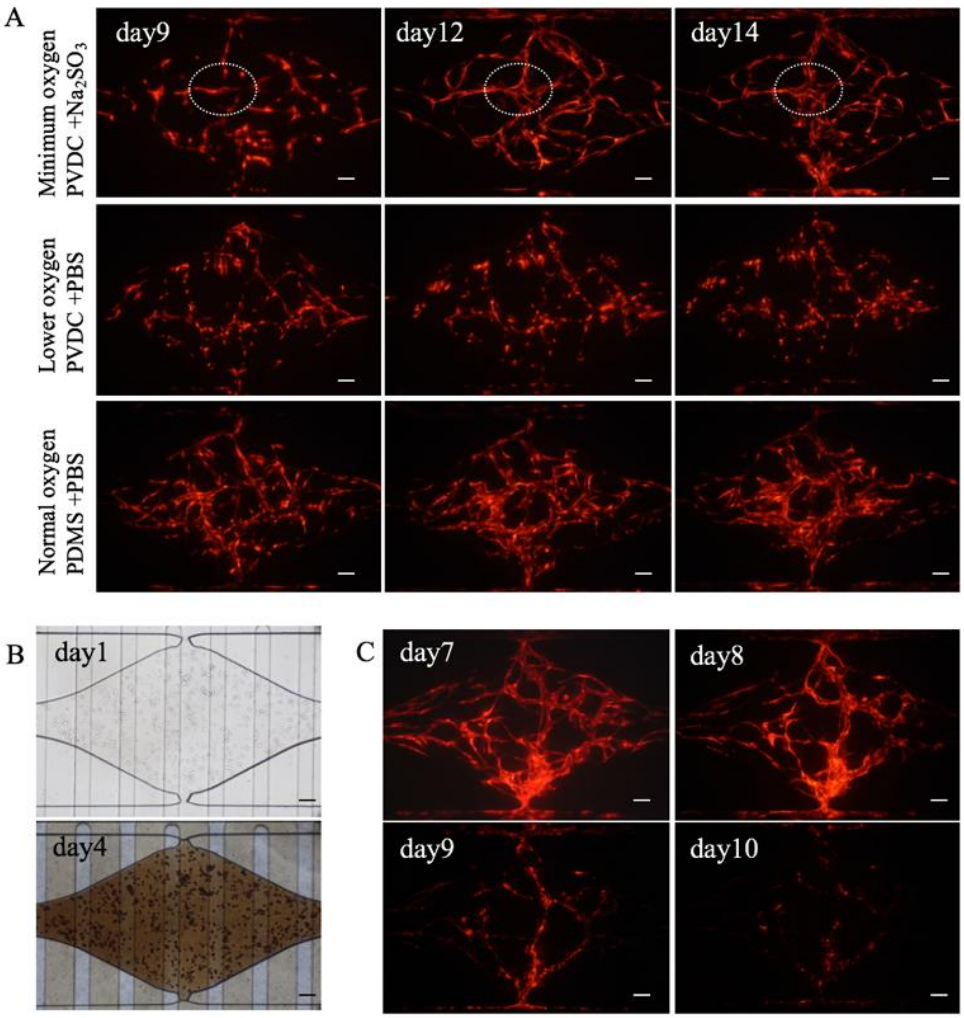

Figure 6.2 Vascularized tissue cultured in the oxygen control test device
(A) Angiogenesis induced by hypoxia condition. The capillary vessel fragment continues to grow after scavenger solution is applied (after day9, labeled in white circles). The vasculature in normal and lower oxygen condition don't show obvious change during the same period. All these chips are cultured for more than 14 days. (B) The color change of pyrogallol's reaction with oxygen. The colored product will also permeate through the PDMS membrane and stay in the tissue chamber during the culture. (C) Toxicity of pyrogallol to the ECs. The primary vasculature is killed by pyrogallol and its product within 3 days. All scale bars are 100μm.

All of the chips can be cultured for more than 14 days, which shows that sodium sulfite is safe as the scavenger for long term 3D tissue culture. We also test the commonly used scavenger pyrogallol (mixed with sodium hydroxide solution at 1:1 concentration). However, all the cells cannot survive for more than 3 days (Figure 6.2 (C)). Besides, the color generated by the chemical reaction will remain inside the tissue chamber to block the bright field channel for image (Figure 6.2 (B)).

Observation of oxygen tension change by luminescent optical sensor and calibration of Stern-Volmer equation

We use RTDP as the luminescent optical sensor to observe the oxygen gradient in liver chip design. First, we need to calibrate the Stern-Volmer equation. PBS and sodium sulfite solution are loaded to the tissue chamber of different chips. Fluorescence images are taken, and the fluorescence intensity are calculated in a rectangular region in the center of the tissue chamber. We observe the fluorescence intensity of RTDP in PBS I_{20}= 65.11, and the fluorescence intensity of RTDP in sodium sulfite I_0= 77.31. Then the calculated K_q= 0.94, and the calibrated Stern-Volmer equation is

$$\frac{77.31}{I} = 1 + 0.94[O_2] \tag{16}$$

Second, we generated the oxygen gradient (Figure 6.2 (C)) by perfusing sodium sulfite solution through the scavenger channel near the channel mimicking portal vein (1μl/min by syringe pump). The tissue chamber is loaded with RTDP with fibrin gel and the fluorescence intensity along the cutting line is calculated (Figure 6.2 (C)). The oxygen tension is calculated by the calibrated Stern-Volmer equation (Equation (16)). This trend is similar to that of the finite element simulation result (Figure 6.2 (B)).

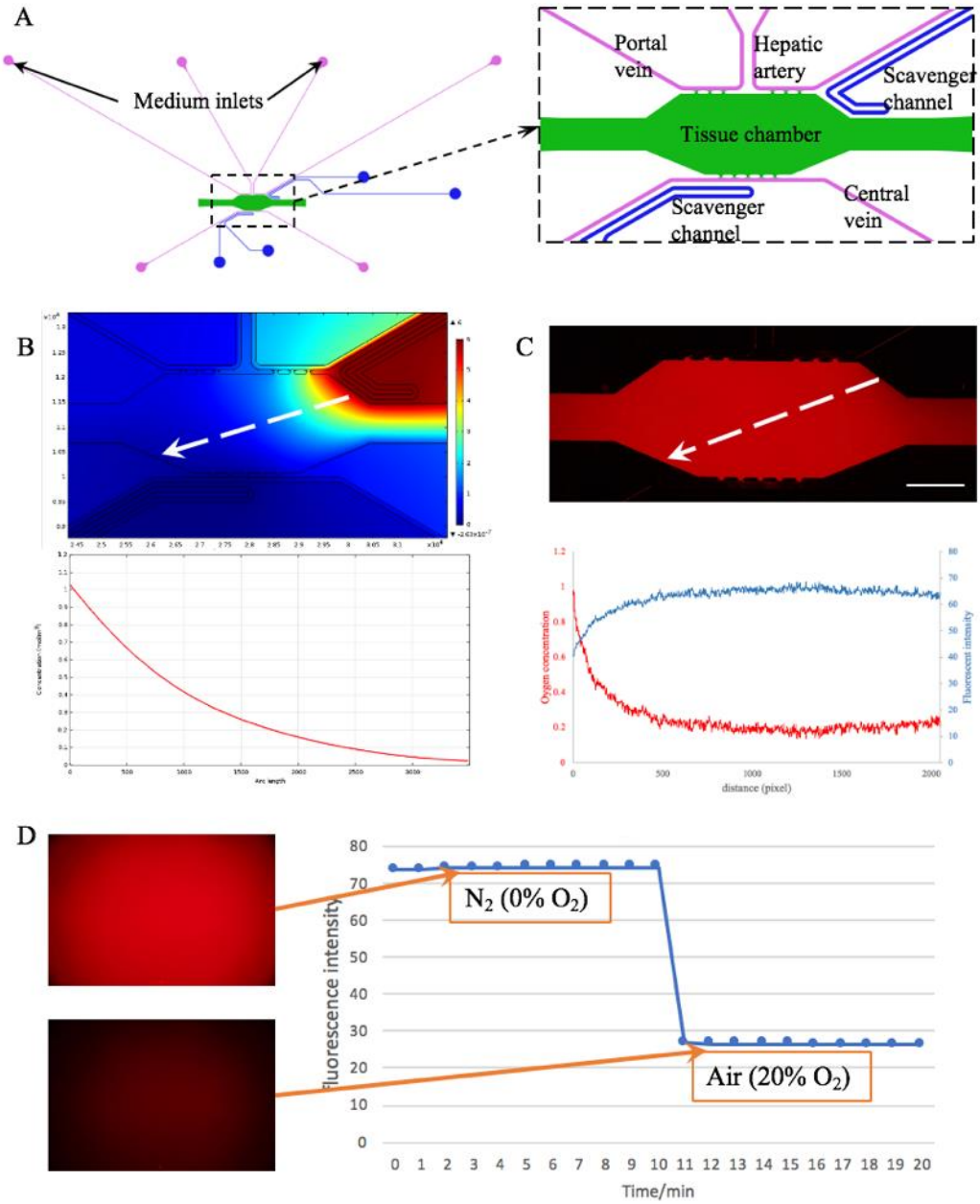

Figure 6.3 Oxygen tension change observed by luminescent optical sensors
(A) The liver chip design. The medium channels provide 3 groups of communication pores for interstitial flow control, mimicking the blood vessel structures in liver (hepatic artery, portal vein and central vein). (B) Finite element simulation of the oxygen distribution in the liver chip design. The 0% oxygen tension is set to the scavenger channel near the central vein channel. Upper: the oxygen gradient. Down: the oxygen tension along the cutting line. (C) Oxygen distribution in the liver chip indicating by RTDP sensor. Upper: oxygen gradient in the liver chip. The scale bar is 1mm. Down: fluorescence intensity along the cutting line and the oxygen tension calculated by Equation (16). (D) Fluorescence change indicated by PtOEP sensor.

The PtOEP sensor substrate is also plasma bonded to a liver chip. The plasma treatment for PDMS causes a reduction of oxygen permeability[159] and the recovery process takes more than

three days[160]. So, the chip is tested 7 days after the plasma bonding to guarantee full recovery oxygen permeability. Compressed air and nitrogen are perfused into the tissue chamber sequentially to test the response of the PtOEP sensor. We observe different fluorescence intensities when perfused with different gases (Figure 6.3 (D)). The Stern-Volmer equation can be calibrated based on these data when the PtOEP sensor is applied during experiment.

Future perspective

The hypoxia induced angiogenesis is not quantified with the oxygen sensor. So, the next step will be integrating the oxygen sensor to the cell culture system for long-term observation of the oxygen tension change in the vascularized micro tissues. The choice of oxygen sensor is a tricky problem. The RTDP sensor is easy to apply by adding to cell culture medium and perfuse through the whole tissue culture region. It can be washed away by clear medium. However, RTDP is slightly toxic to cells and the repetitive loading and washing process could be tedious during long-term culture process. PtOEP sensor overcomes these drawbacks by separating the sensor film from the tissue with PDMS, but the sensor film can only detect the oxygen tension right above the PDMS thin film, which will lose fidelity of the oxygen distribution of 3D tissue. Nevertheless, we've developed both sensors that can be applied to on-chip 3D vascularized tissue, we could choose which type of sensor to use based on the experiment design.

The liver chip design is a novel design we never applied to the vasculature-on-a-chip platform. The 3-group communication pores and medium channels raise the problem how to design the interstitial flow in the tissue chamber. We've tested the vasculogenesis in the liver chip design with hydrostatic pressure dropping from hepatic artery to portal vein and then to central vein, but we find that the capillary vessels form only between hepatic artery and central vein, or

only between portal vein and central vein. Our hypothesis is that the formed capillary vessels will take most of the medium and impair the interstitial flow to the rest of the communication pores. We propose a solution to combine the communication pores at the hepatic artery and portal vein as a group and apply equal hydrostatic pressure between them, but they provide the hydrostatic pressure drop between this group and the central vein. This method is still under examination. After solving the vasculogenesis problem, hepatocyte will be co-cultured with the vasculature and oxygen gradient mimicking in vivo liver microenvironment will be applied by the scavenger. The position of the scavenger channel needs to be optimized to get the oxygen gradient in the tissue chamber to the physiological level. The gene expression or protein correlated with liver zonation will be measured to validate the effectiveness of the vascularized liver model. Eventually, Alk1 knockout ECs will be used to build a more realistic liver HHT model and drug screening study will be performed.

CHAPTER 7: CONCLUSION AND FUTURE PERSPECTIVE

In summary, we have developed an integrated microfluidics system capable of co-culturing multiple tissue types in high throughput manner with multiple aspects of parameters controlled. The system could co-culture 3 types of different tissues, vascularized or non-vascularized, to study the tissue-tissue interactions, in which the flow profile is controlled by the hydrostatic pressure input generated by the medium. The multilayered design provides another method of generating vascularized tissue with large area, and the modular design provides researchers more flexibility for experimental design. The siphon-based autofill pump could provide control of constant hydrostatic pressure inputs to the microfluidics devices for long term steady flow, thus reduce the variance of each experiment and researchers' labor input. It also provides a possible solution of powerless input for microfluidics applications for resource limited situations such as POCT. The HHT chip design is a specialized application of our microfluidics system for desired shear stress control. The oxygen tension control module has different formats to provide local oxygen control for the presented microfluidics system by controlling the scavenger flow. The oxygen sensing system is also developed to track the oxygen tension change in our microfluidics chips. Live/HHT model is under trial for more integrated and biological related tissue/disease model.

By co-culturing different types of tissue in the HT-MTCS, we generated various types of tissue models. First of all, multiple types vascularized tissue were built in different chip designs such as vasculature/ECM/vasculature, vasculature with the same kind of ECs, and vasculatures with different kinds of ECs in different regions. We also built vascularized micro tumor models with tumor localized at different regions of our microfluidics chips. The perfusable vasculature was validated by various materials, such as FITC-dextran solution, fluorescence beads suspension and whole blood. Combined with localized micro tumor and the peristaltic circulation pump, the

perfusable vasculature provided the possibility of generating a platform for observing the whole process of metastasis. This could also be considered as a full replica of human circulation system, which can be applied to other tissue or disease model. We also showcased the capability of generating a genetic wild type/knockout co-culture model with controlled cell configurations. DAPT treated HUVECs were used to mimic the NOTCH signaling pathway knockout cells and were co-cultured with wild type HUVECs in different regions of the HT-MTCS. These two tissue types showed different morphologies in the tissue chambers and angiogenic reactions to the target in the connection channels (cancer cells and chemical cues). Specifically, the DAPT treated HUVECs showed more branched and dilated vessels, and more sprouts towards the cell and chemical cues in the connecting channels.

The multilayered modular design enlightened a new method to generate large scale vasculature in a compact region with flexibility. We solve the space arranging problem of integrating more tissue culture units by separating the medium channels into a different PDMS layer. Different geometries of tissue chambers formed modular devices for various interstitial profiles for different density of vasculatures. A semi closed rhombic medium channel was developed to avoid the air bubbles appearing during cell loading process, and the anastomosis between 3D tissue and medium channel was also achieved by this design. 70kDa FITC-dextran perfusion was demonstrated without non-physiological leakage. Large vascularized tissue arrays have been demonstrated (such as 3×5, 5×5 tissue arrays), and microvascular networks covering more than 14 mm^2, with a vessel density of 12 mm/mm^2 were generated.

The enhanced hydrostatic pressure-driven passive micropump were developed for versatile microfluidics-based applications, especially for cell/tissue culture. The configuration of the entire system is simple and portable, and the related components can be easily acquired. With the siphon-

based autofill function, the steady flow rate with precise control can be supplied automatically and continuously for long terms. The hydrostatic pressure drop can be flexibly adjusted by simply changing the position of the LBC inside the IMR, and the characterization results show that the refilling time will be directly influenced by the air volume inside MSC as well as the siphon diameter. With the integration of various fluidic regulators, the enhanced micropump can be further optimized to realize parallel or multiplexed medium delivery. Experimental results from a vasculogenesis assay demonstrate the effectiveness of this enhanced micropump for cell/tissue culture inside an incubator for 14 days, allowing for the development of superior organ-on-a-chip applications.

The slanted channel microfluidics chip design was created for the HHT model by regulating the shear stress affecting the vasculature. The slanted medium channels form a sector shape of the tissue chamber, which possess different hydraulic resistance, thus generating a non-uniform flow velocity and shear stress gradient in the tissue chamber. By adjusting the angle of the sector shape and the hydrostatic pressure provided by the medium, various shear stress gradient could be applied to the vascularized tissue. The vasculature geometry was modeled to a 2D projection and calculated by finite element simulation software. The high shear stress region could be visualized, and the wall shear stress could be estimated by the simulation model. Combined with gene edited ECs, the slanted channel chip design provides researchers an in vitro platform to study the mechanism of HHT, especially for the shear stress related hypothesis. This chip design has also been fitted to a high throughput format for drug screening study.

The oxygen tension control module of our system could locally control the oxygen tension of the tissue by scavenger flow, either for the whole tissue part or with a spatial oxygen gradient. The scavenger strategy was applied for the oxygen tension control and different oxygen scavenger

has been tested for the vascularized tissue. We found that sodium sulfite is suitable for the long-term culture of vascularized tissue by showing less toxicity to cells. Hypoxia induced angiogenesis were observed in the testing device controlled by sodium sulfite. Oxygen gradient in a new liver chip design was calculated by finite element simulation model and validated by luminescent optical sensor. Two kinds of oxygen sensor were developed for the observation of oxygen distribution in the vascularized tissue in different situations.

One innovative aspect of this dissertation is designing the high throughput tissue culture platforms integrated with 96 well plate. This commonly used platform provides the biologist with a user-friendly interface. It also keeps the adaptability to currently available automation equipment such as liquid handling robot and imaging system. Another aspect is that all the concepts and parts are designed a in modular format for more generalized or universal purposes, not restricted only to the demonstrated examples. This allows quick integration of different parts to a highly integrated tissue culture system with desired parameters controlled, even though few examples were provided such as the HHT model and the liver model. It also has potential for the development of new in vitro tissue culture models, not restricted to vascularized tissue. Besides, several concepts of the accessories supporting the tissue culture models are discussed in this dissertation such as the 3D aligner for multiple layer PDMS device fabrication, the 3D printed well inserts to increase the hydrostatic pressure generated to the tissue, and the peristaltic pump for medium circulation.

As stated in the introduction chapter, the 3D in vitro vascularized tissue models provide a useful platform for mechanism study and have the potential of replacing, or partially replacing, animal models during the drug discovery process. As personalized medicine and other innovative concepts are emerging in the healthcare industry, microfluidics technology, including 3D in vitro vascularized tissue models, will be involved in a myriad of applications. While the author here

looks forward to having the presented vascularized tissue models applied for more scientific researches and the preclinical studies, it is also the author's expectation to inspire researchers in the field as well as to introduce microfluidics technology and applications to the general public.

BIBLIOGRAPHY

[1] S. N. Bhatia and D. E. Ingber, *Nat Biotechnol*, 2014, **32**, 760-772.

[2] P. Loskill, T. Sezhian, K. M. Tharp, F. T. Lee-Montiel, S. Jeeawoody, W. M. Reese, P. H. Zushin, A. Stahl and K. E. Healy, *Lab Chip*, 2017, **17**, 1645-1654.

[3] A. Agarwal, J. A. Goss, A. Cho, M. L. McCain and K. K. Parker, *Lab Chip*, 2013, **13**, 3599-3608.

[4] Y. S. Zhang, A. Arneri, S. Bersini, S. R. Shin, K. Zhu, Z. Goli-Malekabadi, J. Aleman, C. Colosi, F. Busignani, V. Dell'Erba, C. Bishop, T. Shupe, D. Demarchi, M. Moretti, M. Rasponi, M. R. Dokmeci, A. Atala and A. Khademhosseini, *Biomaterials*, 2016, **110**, 45-59.

[5] A. Marsano, C. Conficconi, M. Lemme, P. Occhetta, E. Gaudiello, E. Votta, G. Cerino, A. Redaelli and M. Rasponi, *Lab Chip*, 2016, **16**, 599-610.

[6] D. Huh, B. D. Matthews, A. Mammoto, M. Montoya-Zavala, H. Y. Hsin and D. E. Ingber, *Science (New York, N.Y.)*, 2010, **328**, 1662.

[7] P. Zamprogno, S. Wüthrich, S. Achenbach, J. D. Stucki, N. Hobi, N. Schneider-Daum, C.-M. Lehr, H. Huwer, T. Geiser, R. A. Schmid and O. T. Guenat, *bioRxiv*, 2019, DOI: 10.1101/608919, 608919.

[8] A. Grosberg, A. P. Nesmith, J. A. Goss, M. D. Brigham, M. L. McCain and K. K. Parker, *J Pharmacol Toxicol Methods*, 2012, **65**, 126-135.

[9] M. A. Ortega, X. Fernandez-Garibay, A. G. Castano, F. De Chiara, A. Hernandez-Albors, J. Balaguer-Trias and J. Ramon-Azcon, *Lab Chip*, 2019, **19**, 2568-2580.

[10] P. J. Lee, P. J. Hung and L. P. Lee, *Biotechnol Bioeng*, 2007, **97**, 1340-1346.

[11] N. S. Bhise, V. Manoharan, S. Massa, A. Tamayol, M. Ghaderi, M. Miscuglio, Q. Lang, Y. Shrike Zhang, S. R. Shin, G. Calzone, N. Annabi, T. D. Shupe, C. E. Bishop, A. Atala, M. R. Dokmeci and A. Khademhosseini, *Biofabrication*, 2016, **8**, 014101.

[12] D. Yoon No, K. H. Lee, J. Lee and S. H. Lee, *Lab Chip*, 2015, **15**, 3822-3837.

[13] K. Y. Shim, D. Lee, J. Han, N. T. Nguyen, S. Park and J. H. Sung, *Biomed Microdevices*, 2017, **19**, 37.

[14] S. Jalili-Firoozinezhad, R. Prantil-Baun, A. Jiang, R. Potla, T. Mammoto, J. C. Weaver, T. C. Ferrante, H. J. Kim, J. M. S. Cabral, O. Levy and D. E. Ingber, *Cell Death Dis*, 2018, **9**, 223.

[15] M. Wufuer, G. Lee, W. Hur, B. Jeon, B. J. Kim, T. H. Choi and S. Lee, *Sci Rep*, 2016, **6**, 37471.

[16] F. A. Alexander, S. Eggert and J. Wiest, *Genes (Basel)*, 2018, **9**.

[17] O. Kilic, D. Pamies, E. Lavell, P. Schiapparelli, Y. Feng, T. Hartung, A. Bal-Price, H. T. Hogberg, A. Quinones-Hinojosa, H. Guerrero-Cazares and A. Levchenko, *Lab Chip*, 2016, **16**, 4152-4162.

[18] J. Park, B. K. Lee, G. S. Jeong, J. K. Hyun, C. J. Lee and S. H. Lee, *Lab Chip*, 2015, **15**, 141-150.

[19] Y. I. Wang, H. E. Abaci and M. L. Shuler, *Biotechnol Bioeng*, 2017, **114**, 184-194.

[20] G. Adriani, D. Ma, A. Pavesi, R. D. Kamm and E. L. Goh, *Lab Chip*, 2017, **17**, 448-459.

[21] J. D. Wang, S. Khafagy el, K. Khanafer, S. Takayama and M. E. ElSayed, *Mol Pharm*, 2016, **13**, 895-906.

[22] Y. Xiao, D. Kim, B. Dura, K. Zhang, R. Yan, H. Li, E. Han, J. Ip, P. Zou, J. Liu, A. T. Chen, A. O. Vortmeyer, J. Zhou and R. Fan, *Adv Sci (Weinh)*, 2019, **6**, 1801531.

[23] S. Oh, H. Ryu, D. Tahk, J. Ko, Y. Chung, H. K. Lee, T. R. Lee and N. L. Jeon, *Lab Chip*, 2017, **17**, 3405-3414.

[24] B. Zhang, M. Montgomery, M. D. Chamberlain, S. Ogawa, A. Korolj, A. Pahnke, L. A. Wells, S. Masse, J. Kim, L. Reis, A. Momen, S. S. Nunes, A. R. Wheeler, K. Nanthakumar, G. Keller, M. V. Sefton and M. Radisic, *Nat Mater*, 2016, **15**, 669-678.

[25] C. Kim, J. Kasuya, J. Jeon, S. Chung and R. D. Kamm, *Lab Chip*, 2015, **15**, 301-310.

[26] N. Mori, Y. Morimoto and S. Takeuchi, *Biomaterials*, 2017, **116**, 48-56.

[27] H. F. Wang, R. Ran, Y. Liu, Y. Hui, B. Zeng, D. Chen, D. A. Weitz and C. X. Zhao, *ACS Nano*, 2018, **12**, 11600-11609.

[28] D. E. Discher, P. Janmey and Y. L. Wang, *Science (New York, N.Y.)*, 2005, **310**, 1139-1143.

[29] F. Rosso, A. Giordano, M. Barbarisi and A. Barbarisi, *Journal of cellular physiology*, 2004, **199**, 174-180.

[30] D. Antoni, H. Burckel, E. Josset and G. Noel, *International journal of molecular sciences*, 2015, **16**, 5517-5527.

[31] D. Huh, G. A. Hamilton and D. E. Ingber, *Trends Cell Biol*, 2011, **21**, 745-754.

[32] G. M. Whitesides, *Nature*, 2006, **442**, 368-373.

[33] I. Wagner, E. M. Materne, S. Brincker, U. Sussbier, C. Fradrich, M. Busek, F. Sonntag, D. A. Sakharov, E. V. Trushkin, A. G. Tonevitsky, R. Lauster and U. Marx, *Lab Chip*, 2013, **13**, 3538-3547.

[34] B. Atac, I. Wagner, R. Horland, R. Lauster, U. Marx, A. G. Tonevitsky, R. P. Azar and G. Lindner, *Lab Chip*, 2013, **13**, 3555-3561.
[35] Y. Imura, K. Sato and E. Yoshimura, *Anal Chem*, 2010, **82**, 9983-9988.
[36] J. Theobald, A. Ghanem, P. Wallisch, A. A. Banaeiyan, M. A. Andrade-Navarro, K. Taskova, M. Haltmeier, A. Kurtz, H. Becker, S. Reuter, R. Mrowka, X. L. Cheng and S. Wolfl, *Acs Biomaterials Science & Engineering*, 2018, **4**, 78-89.
[37] C. Zhang, Z. Zhao, N. A. Abdul Rahim, D. van Noort and H. Yu, *Lab Chip*, 2009, **9**, 3185-3192.
[38] I. Maschmeyer, A. K. Lorenz, K. Schimek, T. Hasenberg, A. P. Ramme, J. Hubner, M. Lindner, C. Drewell, S. Bauer, A. Thomas, N. S. Sambo, F. Sonntag, R. Lauster and U. Marx, *Lab Chip*, 2015, **15**, 2688-2699.
[39] T. Satoh, S. Sugiura, K. Shin, R. Onuki-Nagasaki, S. Ishida, K. Kikuchi, M. Kakiki and T. Kanamori, *Lab Chip*, 2017, **18**, 115-125.
[40] Y. S. Zhang, J. Aleman, S. R. Shin, T. Kilic, D. Kim, S. A. Mousavi Shaegh, S. Massa, R. Riahi, S. Chae, N. Hu, H. Avci, W. Zhang, A. Silvestri, A. Sanati Nezhad, A. Manbohi, F. De Ferrari, A. Polini, G. Calzone, N. Shaikh, P. Alerasool, E. Budina, J. Kang, N. Bhise, J. Ribas, A. Pourmand, A. Skardal, T. Shupe, C. E. Bishop, M. R. Dokmeci, A. Atala and A. Khademhosseini, *Proc Natl Acad Sci U S A*, 2017, **114**, E2293-E2302.
[41] E. Ruvinov, Y. Shandalov, S. Levenberg and S. Cohen, in *Tissue Engineering*, eds. C. A. V. Blitterswijk and J. De Boer, Academic Press, Oxford, 2014, DOI: 10.1016/b978-0-12-420145-3.00018-3, pp. 627-683.
[42] M. Radisic, H. Park, F. Chen, J. E. Salazar-Lazzaro, Y. Wang, R. Dennis, R. Langer, L. E. Freed and G. Vunjak-Novakovic, *Tissue Eng*, 2006, **12**, 2077-2091.
[43] M. Tsai, A. Kita, J. Leach, R. Rounsevell, J. N. Huang, J. Moake, R. E. Ware, D. A. Fletcher and W. A. Lam, *The Journal of clinical investigation*, 2012, **122**, 408-418.
[44] W. H. Wu, T. H. Punde, P. C. Shih, C. Y. Fu, T. P. Wang, L. Hsu, H. Y. Chang and C. H. Liu, *Sensors and Actuators B-Chemical*, 2015, **209**, 470-477.
[45] N. Venugopal Menon, H. M. Tay, K. T. Pang, R. Dalan, S. C. Wong, X. Wang, K. H. H. Li and H. W. Hou, *APL Bioeng*, 2018, **2**, 016103.
[46] J. Ko, J. Ahn, S. Kim, Y. Lee, J. Lee, D. Park and N. L. Jeon, *Lab Chip*, 2019, **19**, 2822-2833.
[47] G. S. Jeong, S. Han, Y. Shin, G. H. Kwon, R. D. Kamm, S. H. Lee and S. Chung, *Anal Chem*, 2011, **83**, 8454-8459.
[48] J. S. Jeon, S. Bersini, M. Gilardi, G. Dubini, J. L. Charest, M. Moretti and R. D. Kamm, *Proc Natl Acad Sci U S A*, 2015, **112**, 214-219.
[49] S. Bersini, J. S. Jeon, G. Dubini, C. Arrigoni, S. Chung, J. L. Charest, M. Moretti and R. D. Kamm, *Biomaterials*, 2014, **35**, 2454-2461.
[50] D. Huh, B. D. Matthews, A. Mammoto, M. Montoya-Zavala, H. Y. Hsin and D. E. Ingber, *Science (New York, N.Y.)*, 2010, **328**, 1662-1668.
[51] R. Sudo, S. Chung, I. K. Zervantonakis, V. Vickerman, Y. Toshimitsu, L. G. Griffith and R. D. Kamm, *FASEB J*, 2009, **23**, 2155-2164.
[52] K. J. Jang, A. P. Mehr, G. A. Hamilton, L. A. McPartlin, S. Chung, K. Y. Suh and D. E. Ingber, *Integr Biol (Camb)*, 2013, **5**, 1119-1129.
[53] S. Kim, M. Chung and N. L. Jeon, *Biomaterials*, 2016, **78**, 115-128.
[54] A. Sobrino, D. T. Phan, R. Datta, X. Wang, S. J. Hachey, M. Romero-Lopez, E. Gratton, A. P. Lee, S. C. George and C. C. Hughes, *Sci Rep*, 2016, **6**, 31589.
[55] D. T. T. Phan, X. Wang, B. M. Craver, A. Sobrino, D. Zhao, J. C. Chen, L. Y. N. Lee, S. C. George, A. P. Lee and C. C. W. Hughes, *Lab Chip*, 2017, **17**, 511-520.
[56] C. J. Kastrup, M. Nahrendorf, J. L. Figueiredo, H. Lee, S. Kambhampati, T. Lee, S. W. Cho, R. Gorbatov, Y. Iwamoto, T. T. Dang, P. Dutta, J. H. Yeon, H. Cheng, C. D. Pritchard, A. J. Vegas, C. D. Siegel, S. MacDougall, M. Okonkwo, A. Thai, J. R. Stone, A. J. Coury, R. Weissleder, R. Langer and D. G. Anderson, *Proc Natl Acad Sci U S A*, 2012, **109**, 21444-21449.
[57] D. Huh, D. C. Leslie, B. D. Matthews, J. P. Fraser, S. Jurek, G. A. Hamilton, K. S. Thorneloe, M. A. McAlexander and D. E. Ingber, *Sci Transl Med*, 2012, **4**, 159ra147.
[58] K. Haase and R. D. Kamm, *Regenerative medicine*, 2017, **12**, 285-302.
[59] A. Hasan, A. Paul, N. E. Vrana, X. Zhao, A. Memic, Y. S. Hwang, M. R. Dokmeci and A. Khademhosseini, *Biomaterials*, 2014, **35**, 7308-7325.

[60] J. R. Gershlak, S. Hernandez, G. Fontana, L. R. Perreault, K. J. Hansen, S. A. Larson, B. Y. Binder, D. M. Dolivo, T. Yang, T. Dominko, M. W. Rolle, P. J. Weathers, F. Medina-Bolivar, C. L. Cramer, W. L. Murphy and G. R. Gaudette, *Biomaterials*, 2017, **125**, 13-22.
[61] A. D. Wong and P. C. Searson, *Cancer Res*, 2014, **74**, 4937-4945.
[62] W. Wu, A. DeConinck and J. A. Lewis, *Adv Mater*, 2011, **23**, H178-183.
[63] J. S. Miller, K. R. Stevens, M. T. Yang, B. M. Baker, D. H. Nguyen, D. M. Cohen, E. Toro, A. A. Chen, P. A. Galie, X. Yu, R. Chaturvedi, S. N. Bhatia and C. S. Chen, *Nat Mater*, 2012, **11**, 768-774.
[64] J. W. Song and L. L. Munn, *Proc Natl Acad Sci U S A*, 2011, **108**, 15342-15347.
[65] S. Kim, M. Chung, J. Ahn, S. Lee and N. L. Jeon, *Lab Chip*, 2016, **16**, 4189-4199.
[66] Y. Shin, J. S. Jeon, S. Han, G. S. Jung, S. Shin, S. H. Lee, R. Sudo, R. D. Kamm and S. Chung, *Lab Chip*, 2011, **11**, 2175-2181.
[67] W. A. Farahat, L. B. Wood, I. K. Zervantonakis, A. Schor, S. Ong, D. Neal, R. D. Kamm and H. H. Asada, *PLoS One*, 2012, **7**, e37333.
[68] Y. Zheng, J. Chen, M. Craven, N. W. Choi, S. Totorica, A. Diaz-Santana, P. Kermani, B. Hempstead, C. Fischbach-Teschl, J. A. Lopez and A. D. Stroock, *Proc Natl Acad Sci U S A*, 2012, **109**, 9342-9347.
[69] M. L. Moya, Y. H. Hsu, A. P. Lee, C. C. Hughes and S. C. George, *Tissue Eng Part C Methods*, 2013, **19**, 730-737.
[70] Y. H. Hsu, M. L. Moya, C. C. Hughes, S. C. George and A. P. Lee, *Lab Chip*, 2013, **13**, 2990-2998.
[71] Y. H. Hsu, M. L. Moya, P. Abiri, C. C. Hughes, S. C. George and A. P. Lee, *Lab Chip*, 2013, **13**, 81-89.
[72] X. Wang, D. T. Phan, A. Sobrino, S. C. George, C. C. Hughes and A. P. Lee, *Lab Chip*, 2016, **16**, 282-290.
[73] X. Wang, D. T. T. Phan, D. Zhao, S. C. George, C. C. W. Hughes and A. P. Lee, *Lab Chip*, 2016, **16**, 868-876.
[74] M. Kang, W. Park, S. Na, S. M. Paik, H. Lee, J. W. Park, H. Y. Kim and N. L. Jeon, *Small*, 2015, **11**, 2789-2797.
[75] C. P. Huang, J. Lu, H. Seon, A. P. Lee, L. A. Flanagan, H. Y. Kim, A. J. Putnam and N. L. Jeon, *Lab on a Chip*, 2009, **9**, 1740-1748.
[76] P. Vulto, S. Podszun, P. Meyer, C. Hermann, A. Manz and G. A. Urban, *Lab Chip*, 2011, **11**, 1596-1602.
[77] S. J. Trietsch, G. D. Israels, J. Joore, T. Hankemeier and P. Vulto, *Lab Chip*, 2013, **13**, 3548-3554.
[78] L. F. Alonzo, M. L. Moya, V. S. Shirure and S. C. George, *Lab Chip*, 2015, **15**, 3521-3529.
[79] M. Mori, T. Miyamoto, H. Yakushiji, S. Ohno, Y. Miyake, T. Sakaguchi, M. Hattori, A. Hongo, A. Nakaizumi, M. Ueda and E. Ohno, *Hum Cell*, 2012, **25**, 9-15.
[80] J. M. Melero-Martin, Z. A. Khan, A. Picard, X. Wu, S. Paruchuri and J. Bischoff, *Blood*, 2007, **109**, 4761-4768.
[81] X. Chen, A. S. Aledia, S. A. Popson, L. Him, C. C. Hughes and S. C. George, *Tissue Eng Part A*, 2010, **16**, 585-594.
[82] J. Dufraine, Y. Funahashi and J. Kitajewski, *Oncogene*, 2008, **27**, 5132-5137.
[83] R. C. Sainson, J. Aoto, M. N. Nakatsu, M. Holderfield, E. Conn, E. Koller and C. C. Hughes, *FASEB J*, 2005, **19**, 1027-1029.
[84] A. H. Zisch, M. P. Lutolf, M. Ehrbar, G. P. Raeber, S. C. Rizzi, N. Davies, H. Schmokel, D. Bezuidenhout, V. Djonov, P. Zilla and J. A. Hubbell, *FASEB J*, 2003, **17**, 2260-2262.
[85] P. Loskill, S. G. Marcus, A. Mathur, W. M. Reese and K. E. Healy, *PLoS One*, 2015, **10**, e0139587.
[86] K. C. Bhargava, B. Thompson and N. Malmstadt, *Proc Natl Acad Sci U S A*, 2014, **111**, 15013-15018.
[87] K. A. Shaikh, K. S. Ryu, E. D. Goluch, J. M. Nam, J. Liu, C. S. Thaxton, T. N. Chiesl, A. E. Barron, Y. Lu, C. A. Mirkin and C. Liu, *Proc Natl Acad Sci U S A*, 2005, **102**, 9745-9750.
[88] M. Zhang, J. Wu, L. Wang, K. Xiao and W. Wen, *Lab Chip*, 2010, **10**, 1199-1203.
[89] Y. Xia and G. M. Whitesides, *Angew Chem Int Ed Engl*, 1998, **37**, 550-575.
[90] S. P. Desai, D. M. Freeman and J. Voldman, *Lab Chip*, 2009, **9**, 1631-1637.
[91] E. A. Logsdon, S. D. Finley, A. S. Popel and F. Mac Gabhann, *J Cell Mol Med*, 2014, **18**, 1491-1508.
[92] V. S. Shirure, A. Lezia, A. Tao, L. F. Alonzo and S. C. George, *Angiogenesis*, 2017, **20**, 493-504.
[93] V. van Duinen, S. J. Trietsch, J. Joore, P. Vulto and T. Hankemeier, *Current opinion in biotechnology*, 2015, **35**, 118-126.
[94] P. J. Hung, P. J. Lee, P. Sabounchi, N. Aghdam, R. Lin and L. P. Lee, *Lab on a Chip*, 2005, **5**, 44-48.
[95] V. Studer, A. Pépin, Y. Chen and A. Ajdari, *Analyst*, 2004, **129**, 944-949.
[96] K. W. Bong, S. C. Chapin, D. C. Pregibon, D. Baah, T. M. Floyd-Smith and P. S. Doyle, *Lab on a Chip*, 2011, **11**, 743-747.
[97] S. K. Sia and L. J. Kricka, *Lab on a Chip*, 2008, **8**, 1982-1983.

[98] M. A. Unger, H.-P. Chou, T. Thorsen, A. Scherer and S. R. Quake, *Science (New York, N.Y.)*, 2000, **288**, 113-116.
[99] H.-P. Chou, M. A. Unger and S. R. Quake, *Biomedical Microdevices*, 2001, **3**, 323-330.
[100] H. Andersson, W. Van Der Wijngaart, P. Nilsson, P. Enoksson and G. Stemme, *Sensors and Actuators B: Chemical*, 2001, **72**, 259-265.
[101] J. C. Rife, M. I. Bell, J. S. Horwitz, M. N. Kabler, R. C. Y. Auyeung and W. J. Kim, *Sensors and Actuators A: Physical*, 2000, **86**, 135-140.
[102] S. Debesset, C. J. Hayden, C. Dalton, J. C. T. Eijkel and A. Manz, *Lab on a Chip*, 2004, **4**, 396-400.
[103] J. Zeng and T. Korsmeyer, *Lab on a Chip*, 2004, **4**, 265-277.
[104] A. V. Lemoff and A. P. Lee, *Sensors and Actuators B: Chemical*, 2000, **63**, 178-185.
[105] M. Zimmermann, S. Bentley, H. Schmid, P. Hunziker and E. Delamarche, *Lab on a Chip*, 2005, **5**, 1355-1359.
[106] G. M. Walker and D. J. Beebe, *Lab on a Chip*, 2002, **2**, 131-134.
[107] J. Y. Park, C. M. Hwang, S. H. Lee and S.-H. Lee, *Lab on a Chip*, 2007, **7**, 1673-1680.
[108] D. Y. Liang, A. M. Tentori, I. K. Dimov and L. P. Lee, *Biomicrofluidics*, 2011, **5**, 024108.
[109] L. Qin, O. Vermesh, Q. Shi and J. R. Heath, *Lab on a Chip*, 2009, **9**, 2016-2020.
[110] T. Kokalj, Y. Park, M. Vencelj, M. Jenko and L. P. Lee, *Lab on a Chip*, 2014, **14**, 4329-4333.
[111] G. S. Jeong, J. Oh, S. B. Kim, M. R. Dokmeci, H. Bae, S.-H. Lee and A. Khademhosseini, *Lab on a chip*, 2014, **14**, 4213-4219.
[112] M. Zimmermann, H. Schmid, P. Hunziker and E. Delamarche, *Lab on a Chip*, 2007, **7**, 119-125.
[113] K. Iwai, K. C. Shih, X. Lin, T. A. Brubaker, R. D. Sochol and L. Lin, *Lab on a Chip*, 2014, **14**, 3790-3799.
[114] S. Begolo, D. V. Zhukov, D. A. Selck, L. Li and R. F. Ismagilov, *Lab on a Chip*, 2014, **14**, 4616-4628.
[115] J. Siegrist, R. Gorkin, L. Clime, E. Roy, R. Peytavi, H. Kido, M. Bergeron, T. Veres and M. Madou, *Microfluidics and nanofluidics*, 2010, **9**, 55-63.
[116] X. Wang, D. Zhao, D. T. T. Phan, J. Liu, X. Chen, B. Yang, C. C. W. Hughes, W. Zhang and A. P. Lee, *Lab Chip*, 2018, **18**, 2167-2177.
[117] S.-J. Kim, R. Yokokawa, S. C. Lesher-Perez and S. Takayama, *Nature communications*, 2015, **6**, 1-7.
[118] J. W. Wee, Y. W. Jeon, J. Y. Eun, H. J. Kim, S. B. Bae and K. T. Lee, *Blood research*, 2014, **49**, 192-195.
[119] A. Evans, P. Whelehan, K. Thomson, D. McLean, K. Brauer, C. Purdie, L. Baker, L. Jordan, P. Rauchhaus and A. Thompson, *Radiology*, 2012, **263**, 673-677.
[120] J. McDonald, P. Bayrak-Toydemir and R. E. Pyeritz, *Genetics in Medicine*, 2011, **13**, 607-616.
[121] D. A. Marchuk, A. E. Guttmacher, J. A. Penner and P. Ganguly, *American journal of medical genetics*, 1998, **76**, 269-273.
[122] J. McDonald, W. Wooderchak-Donahue, C. VanSant Webb, K. Whitehead, D. A. Stevenson and P. Bayrak-Toydemir, *Frontiers in Genetics*, 2015, **6**, 1.
[123] N. Baeyens, B. Larrivee, R. Ola, B. Hayward-Piatkowskyi, A. Dubrac, B. Huang, T. D. Ross, B. G. Coon, E. Min, M. Tsarfati, H. Tong, A. Eichmann and M. A. Schwartz, *J Cell Biol*, 2016, **214**, 807-816.
[124] P. Corti, S. Young, C. Y. Chen, M. J. Patrick, E. R. Rochon, K. Pekkan and B. L. Roman, *Development*, 2011, **138**, 1573-1582.
[125] W. W. Sugden, R. Meissner, T. Aegerter-Wilmsen, R. Tsaryk, E. V. Leonard, J. Bussmann, M. J. Hamm, W. Herzog, Y. Jin, L. Jakobsson, C. Denz and A. F. Siekmann, *Nature Cell Biology*, 2017, **19**, 653-665.
[126] S. Tual-Chalot, S. P. Oh and H. M. Arthur, *Front Genet*, 2015, **6**, 25.
[127] R. N. Wilkinson and F. J. M. van Eeden, in *Progress in Molecular Biology and Translational Science*, ed. T. J. A. Chico, Academic Press, 2014, vol. 124, pp. 93-122.
[128] M. O. Bernabeu, M. L. Jones, J. H. Nielsen, T. Kruger, R. W. Nash, D. Groen, S. Schmieschek, J. Hetherington, H. Gerhardt, C. A. Franco and P. V. Coveney, *J R Soc Interface*, 2014, **11**.
[129] D. F. Wilson, D. K. Harrison and S. A. Vinogradov, *J Appl Physiol (1985)*, 2012, **113**, 1838-1845.
[130] A. Mohyeldin, T. Garzon-Muvdi and A. Quinones-Hinojosa, *Cell Stem Cell*, 2010, **7**, 150-161.
[131] C. I. Kobayashi and T. Suda, *Journal of cellular physiology*, 2012, **227**, 421-430.
[132] G. L. Semenza, *N Engl J Med*, 2011, **365**, 537-547.
[133] W. K. R. Barnikol and H. Pötzschke, *GMS German Medical Science*, 2012, **10**.
[134] G. D'Ippolito, S. Diabira, G. A. Howard, B. A. Roos and P. C. Schiller, *Bone*, 2006, **39**, 513-522.
[135] Z. Ivanovic, *Journal of cellular physiology*, 2009, **219**, 271-275.
[136] M. D. Brennan, M. L. Rexius-Hall, L. J. Elgass and D. T. Eddington, *Lab Chip*, 2014, **14**, 4305-4318.
[137] S. Grist, L. Yu, L. Chrostowski and K. C. Cheung.
[138] E. Leclerc, Y. Sakai and T. Fujii, *Biomedical Microdevices*, 2003, **5**, 109-114.

[139] M. Polinkovsky, E. Gutierrez, A. Levchenko and A. Groisman, *Lab Chip*, 2009, **9**, 1073-1084.
[140] S. C. Oppegard, A. J. Blake, J. C. Williams and D. T. Eddington, *Lab on a Chip*, 2010, **10**, 2366-2373.
[141] H. E. Abaci, R. Devendra, R. Soman, G. Drazer and S. Gerecht, *Biotechnol Appl Biochem*, 2012, **59**, 97-105.
[142] K. Funamoto, I. K. Zervantonakis, Y. Liu, C. J. Ochs, C. Kim and R. D. Kamm, *Lab on a chip*, 2012, **12**, 4855-4863.
[143] J. M. Higgins, D. T. Eddington, S. N. Bhatia and L. Mahadevan, *Proc Natl Acad Sci U S A*, 2007, **104**, 20496-20500.
[144] G. Mauleon, J. F. Lo, B. L. Peterson, C. P. Fall and D. T. Eddington, *J Neurosci Methods*, 2013, **216**, 110-117.
[145] M. Adler, M. Erickstad, E. Gutierrez and A. Groisman, *Lab Chip*, 2012, **12**, 4835-4847.
[146] J. F. Lo, E. Sinkala and D. T. Eddington, *Lab Chip*, 2010, **10**, 2394-2401.
[147] E. Sinkala and D. T. Eddington, *Lab Chip*, 2010, **10**, 3291-3295.
[148] J. W. Allen, S. R. Khetani and S. N. Bhatia, *Toxicol Sci*, 2005, **84**, 110-119.
[149] M. Skolimowski, M. W. Nielsen, J. Emneus, S. Molin, R. Taboryski, C. Sternberg, M. Dufva and O. Geschke, *Lab on a Chip*, 2010, **10**, 2162-2169.
[150] Y. A. Chen, A. D. King, H. C. Shih, C. C. Peng, C. Y. Wu, W. H. Liao and Y. C. Tung, *Lab Chip*, 2011, **11**, 3626-3633.
[151] L. Wang, W. Liu, Y. Wang, J. C. Wang, Q. Tu, R. Liu and J. Wang, *Lab Chip*, 2013, **13**, 695-705.
[152] M. Rasponi, T. Ullah, R. J. Gilbert, G. B. Fiore and T. A. Thorsen, *Med Eng Phys*, 2011, **33**, 887-892.
[153] S. F. Lam, V. S. Shirure, Y. E. Chu, A. G. Soetikno and S. C. George, *PLoS One*, 2018, **13**, e0209574.
[154] L. C. Clark Jr, R. Wolf, D. Granger and Z. Taylor, *Journal of applied physiology*, 1953, **6**, 189-193.
[155] P. E. Oomen, M. D. Skolimowski and E. Verpoorte, *Lab Chip*, 2016, **16**, 3394-3414.
[156] G. Mehta, K. Mehta, D. Sud, J. W. Song, T. Bersano-Begey, N. Futai, Y. S. Heo, M. A. Mycek, J. J. Linderman and S. Takayama, *Biomed Microdevices*, 2007, **9**, 123-134.
[157] A. P. Vollmer, R. F. Probstein, R. Gilbert and T. Thorsen, *Lab Chip*, 2005, **5**, 1059-1066.
[158] N. Li, C. Luo, X. Zhu, Y. Chen, Q. Ouyang and L. Zhou, *Microelectronic Engineering*, 2011, **88**, 1698-1701.
[159] K. S. Houston, D. H. Weinkauf and F. F. Stewart, *Journal of Membrane Science*, 2002, **205**, 103-112.
[160] D. A. Markov, E. M. Lillie, S. P. Garbett and L. J. McCawley, *Biomed Microdevices*, 2014, **16**, 91-96.

APPENDIX A: CALCULATION OF HYDROSTATIC PRESSURE BALANCE IN MEDIUM RESERVOIR

We need to set up a mathematic model to determine how long the medium is balanced in the reservoir. The medium flow in the microfluidics channel follows the pressure driven Poiseuille flow in long and straight channel (Figure A1), which is also an analogue to Ohm's law:

$$Q = \frac{\Delta P}{R} \tag{A1}$$

where Q is the volumetric flow rate, ΔP is the pressure drop between the inlet and outlet (P_1-P_2), and R is the hydraulic resistance. The hydrostatic pressure generated by the medium reservoir is P= ρgH, where ρ is the density of water (1000kg/m_3), g is gravitational acceleration (9.8m/s_2), and H_1 and H_2 are the medium heights in the inlet an out reservoir accordingly. If we set the top surface of the outlet reservoir as the reference plane and the initial medium height at inlet reservoir is H_0 (H_0= 10mm) and that at outlet reservoir is 0, the pressure drop between the inlet and outlet reservoir will be

$$\Delta P = \rho g(H_0 - H_2) - \rho g H_2 = \rho g(H_0 - 2H_2) \tag{A2}$$

Our channel is designed in a square shape, thus the resistance in the channel follows:

$$R = 28.4\frac{\eta L}{h^4} \tag{A3}$$

where η is the dynamic viscosity (water is used in the system with η= 8.9×10_{-4}Pa·s), h is the channel height (100μm), and L the microfluidics channel length. If we set the bottom surface area is S (with radius r= 4mm), the volume change in outlet reservoir satisfy the equation:

$$\int_0^t \frac{\Delta P}{R} dt = H_2 S \tag{A4}$$

Combining Equation (A2) and (A4), and organizing, we can get the equation system with the boundary condition:

$$\begin{cases} H_2' + \frac{2\rho g}{SR} H_2 = \frac{\rho g H_0}{SR} \\ H_2(0) = 0 \end{cases} \tag{A5}$$

This is a first order nonhomogeneous linear ordinary differential equation. Solving this equation and plugging in Equation (A3), we can get the expression of the height in outlet reservoir H_2 as a function of time:

$$H_2(t) = \frac{H_0}{2} - \frac{H_0}{2} e^{-\frac{\rho g h^4}{14.2\pi r \eta L} t} \tag{A6}$$

By performing a data sweep with different channel length L and plotting H_2 by MATLAB, we find that H_2 increases with a gradually decreasing acceleration (Figure A1). As the channel L increases, we can see a longer time H_2 needs to approach the steady states ($\frac{H_0}{2} = 5mm$). With this relation, we can find the right length for the microfluidics resistor when we design the chip.

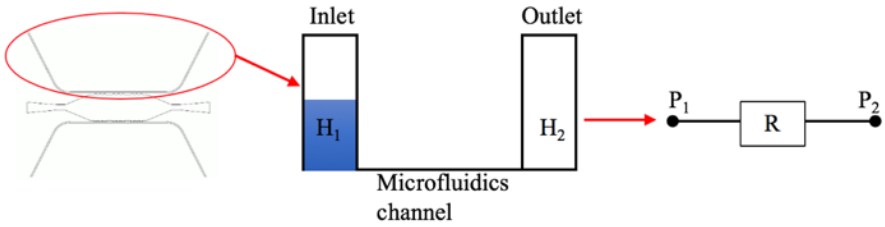

Figure A1 Pressure driven Poiseuille flow in long and straight channel and analogy to electric circuit

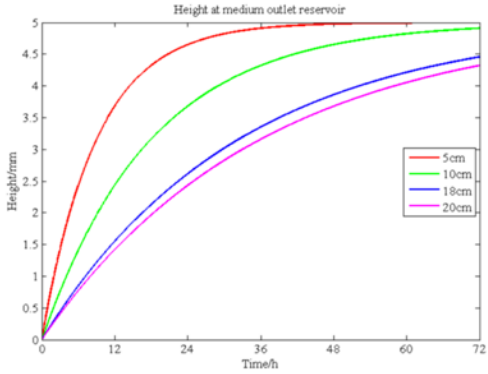

Figure A2 Medium height change over time in the outlet reservoir with different microfluidic channel lengths

APPENDIX B: 3D ALIGNING SYSTEM FOR MULTILAYER PDMS DEVICE ASSEMBLY

As we are meeting the problem that the structure of PDMS microfluidics devices getting increasingly complex especially when multilayer layout exists. Due to the small dimension of microfluidics channels, it's very difficult to look at the detail of channel features and manipulate the chip in small motions. To address this problem, an aligning system (Figure B1 (A)). is built allowing observing the channel feature with magnifying cameras and manipulating the PDMS slabs in 4 degree of freedom (X, Y, Z and σ). The aligning system is made with 2 general parts: cameras and the aligning stage. The cameras are fixed to separated holders that have 3 degree of freedom, so that the cameras can be moved to observe different part of the microfluidics chip for aligning markers (Figure B1 (B)). The aligning stage can be divided into two parts. The ceiling glass is held by three point, and two of which can be adjust with different height to make sure the ceiling glass is level. The bottom stage can control the bottom part of the PDMS slab to move in X, Y, Z and σ (Figure B1 (C)). During the aligning process, the top part PDMS slab is stuck on to the bottom of the ceiling glass and adjusted to right field of view for the cameras. The bottom PDMS slab is stuck on the bottom stage after the Z position is preadjusted to very close to the top PDMS slab. The position where these two parts are is called the pre-aligned position. Then the bottom PDMS slab and the top PDMS slab with ceiling glass are put the plasma cleaner for plasma treatment. Once the treatment is finished, the two PDMS are put back to pre-aligned position. The ceiling glass is quickly check for level. The bottom PDMS slab is quickly adjusted for X, Y and σ position for the best aligning effect. At last, the bottom stage is adjusted to rise the Z position to adhere the bottom PDMS slab to the top PDMS slab. The breadboard and the motion control stages

are purchase from Newport Corporation. The rest of the holder parts are made by 3D printing in our lab.

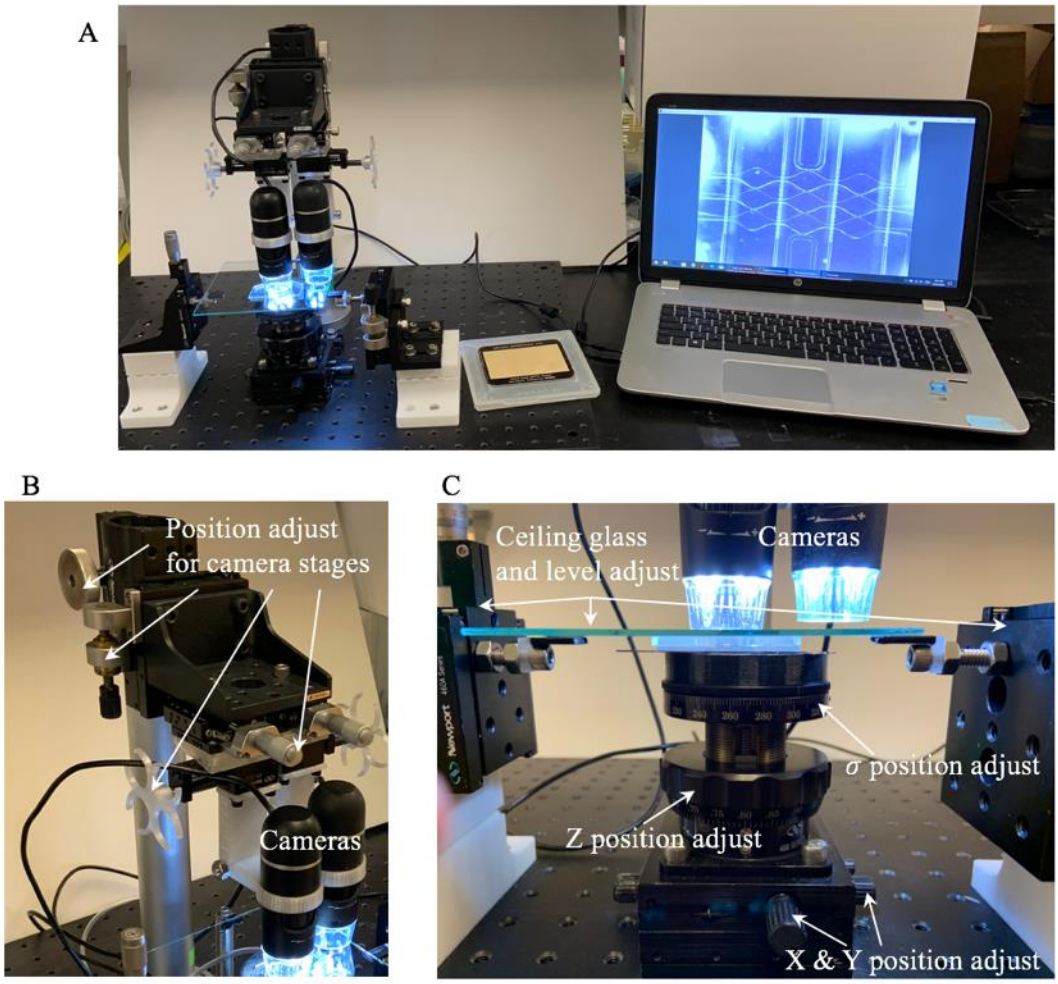

Figure B1 3D aligning system for multilayer PDMS device assembly
(A) The whole system for 3D aligning. A two-layer microfluidics chip described in Chapter 3 is used as a demonstration. (B) The cameras and moving stages. These moving stages allow the cameras to move in X, Y, and Z position, as well as tilt to an angle. (C) Aligning stage. The ceiling glass is held by three points allowing level adjusting. The bottom stage allows the adjusting of X, Y, Z and σ position for the bottom PDMS slab.

APPENDIX C: DETAILED DESCRIPTION OF THE MOVIES

Movie 2.1 Perfusion of whole blood in the HT-MTCS chip

The whole blood is injected by micro pipette from medium inlet M4. Red blood cells deformation and passing through the capillary in single column is observed.

Movie 2.2 Perfusion of FITC-labeled polystyrene beads in the HT-MTCS chip

FITC-labeled polystyrene beads are loaded from medium inlet M4. The diameter of beads is 7.2μm. The beads could be stopped or trapped due to the slow flow rate. The diameter change of the beads is due to the fact that the beads flow in and out of the focal plane.

Movie 2.3 Perfusion of FITC-labeled polystyrene beads in the HT-MTCS chip (2)

FITC-labeled polystyrene beads are loaded from medium inlet M4. The diameter of beads is 7.2μm. The beads can flow from TR to TM, proving fully connected and perfusable vascular network between different tissue culture regions.

Movie 3.1 Liquid loading to the rhombic shape medium channel

Water with red food dye is loaded to the rhombic shape medium channel. The communication pore region is avoided with any air bubble.

Movie 3.2 Confocal image showing the vertical anastomosis between the tissue and medium channel

The ECs grow to the rhombic shape medium channel and form 3D tubular shape to anastomose the vasculature in the tissue chamber and the medium channel.